TESIS DE LA UNIVERSIDAD DE ZARAGOZA

2015

46

Pascual Sevillano Reyes

Study of all-optical network monitoring techniques based on high resolution spectral measurement

Departamento
Física Aplicada

Director/es
Subías Domingo, Jesús Mario
Villafranca Velasco, Asier

ISSN 2254-7606

Prensas de la Universidad
Universidad Zaragoza

ISSN 2254-7606

Universidad Zaragoza
1542

Tesis Doctoral

STUDY OF ALL-OPTICAL NETWORK MONITORING TECHNIQUES BASED ON HIGH RESOLUTION SPECTRAL MEASUREMENT

Autor

Pascual Sevillano Reyes

Director/es

Subías Domingo, Jesús Mario
Villafranca Velasco, Asier

UNIVERSIDAD DE ZARAGOZA

Física Aplicada

2015

Photonics Technologies Group (GTF)
Aragon Institute for Engineering Research (I3A)
Applied Physics Department
University of Zaragoza

PhD Thesis:

Study of all-optical network monitoring techniques based on high resolution spectral measurement

Universidad Zaragoza

Author: Pascual Sevillano Reyes
Advisors: Jesús Subías Domingo
Asier Villafranca Velasco

Thesis presented in fulfillment of the doctorate program of the applied physics department,
University of Zaragoza
March 2015

Instituto Universitario de Investigación de Ingeniería de Aragón Universidad Zaragoza
Facultad de Ciencias Universidad Zaragoza
Departamento de Física Aplicada Universidad Zaragoza

A mi madre, mi padre, mi hermano y a Amaia

AGRADECIMIENTOS

Ha sido duro pero ya hemos llegado. A lo largo de esta tesis se ha procurado usar la primera persona del plural porque, pese a que solo se ha puesto un autor en la portada, han sido muchos los que han colaborado, directa o indirectamente, para que este proyecto haya salido adelante y sería injusto no dedicarles unos merecidos párrafos para que de manera modesta su labor sea agradecida y reconocida. Sé que esta va a ser con diferencia la página más leída así que voy a intentar hacerlo lo mejor posible y espero no dejarme a nadie.

No puedo empezar los agradecimientos sin mencionar a las dos grandes personas que lamentablemente hemos perdido en el grupo a lo largo de este trabajo. Francisco Villuendas era una persona difícil de describir y encajar en los cánones de catedrático de Física Aplicada, creo que por eso me fascinaba tanto aprender de él. Necesitaría muchas hojas para enumerar lo que le debo a Paco y cuando agradecido estoy. Simplemente espero que la gente pueda ver en nosotros, tus becarios, una pequeña parte de la sabiduría que se fue contigo.

Poca gente sabe que fue Zulema de la Rosa quien me presentó a Paco en septiembre de 2008 y que fue por tanto culpable en primera instancia de que yo esté escribiendo estas líneas. A lo largo de la licenciatura y de las etapas que compartí con ella dentro del grupo disfrute de todas y cada una de las charlas-discusiones, donde siempre era capaz de hacerme ver un lado diferente de las cosas. Con ella se fue para mí un referente del altruismo y de la responsabilidad social.

A mi director Jesús Subías le tengo que elogiar por el apoyo que me ha brindado especialmente en los periodos desalentadores que me abordaron en alguna etapa de la tesis. En los momentos de mayor ofuscación siempre fue capaz de mantener la calma y detrás de su pausado silencio siempre me regalaba una reflexión que suponía una bocanada de aire fresco para afrontar la siguiente etapa. A mi director Asier Villafranca no sé cómo agradecerle la paciencia de la que hizo acopio en las últimas etapas. Su capacidad de decisión y resolución aún siguen sorprendiéndome, espero que el futuro nos permita seguir compartiendo cañas en plaza San Francisco. Gracias al tiempo y orientación de ambos esta tesis ha llegado a puerto, más bien al registro central.

A Javier Pelayo que junto con Paco fue quien me ofreció mi primera beca en el grupo para las primeras medidas de fibra óptica. A él le debo mi formación de base en óptica e informática, y aun siendo ya abuelo no conozco mejor asesor tecnológico. No hay fenómeno físico que no se pueda entender después de una de sus explicaciones, todas ellas didácticamente amenizadas con simulaciones en el lenguaje de programación que quieras.

A mis antiguos compañeros de despacho Diego Sancho y después Alejandra Consejo tengo que agradecerles el ánimo incondicional que me dieron desde el principio así como de los buenos momentos que me han hecho pasar cuando levantaba los ojos del teclado. Por muy separados que estemos siempre os llevo conmigo.

A mis compañeras de grupo Cristina Pelayo y Ana Cueva por las lecciones de madurez en los cafés y haberme mostrado cómo se puede compaginar la felicidad dentro y fuera del trabajo. De ellas no me han faltado palabras de apoyo. A mi compañero Enrique Carretero por solucionar más de una duda burocrática. A la gente del CPS, Marta Mainar, Marta Osta, Rafa Gella, Adrian, Iñigo

Salinas, Santiago y Eduardo, que no han dudado en prestarme cualquier pieza/herramienta/equipo cuando lo he necesitado. A Félix Sotelo, Jose Antonio Altabas y en especial a Miguel Cabezón. A ellos debo mucha de mi formación transversal. A Carlos Heras por sus explicaciones sobre efectos no lineales en mis primeros años y en espacial a Rafael Alonso que de manera ciega confió en mantenerme en el grupo el último periodo.

A toda la gente que me he cruzado a lo largo de estos años en mi labor investigadora. A Isabel Roche que compartió conmigo el sufrimiento de las tediosas medidas en WALQA, a Víctor Berdejo cuya asesoría en el uso de equipamiento ha sido fundamental, a su predecesor Jose Antonio que me dio clases magistrales sobre el uso de la fusionadora de fibra.

A Josep M. Fàbrega y Michela Svaluto por habernos dado la oportunidad de poder colaborar en las medidas de OFDM. Por el gran y arduo trabajo que supuso el tratamiento de aquellas medidas; sin su interés y dedicación esas medidas no habrían visto la luz.

A las empresas APL y Fibercom desde las cuales se ha obtenido un valioso feedback para la realización de este trabajo. En especial a Francisco Lopez con quien viene bien charlar de vez en cuando para que te "abofetee" con una buena de dosis de realidad empresarial. Al Ministerio de Ciencia e Innovación por el proyecto concedido y la Universidad de Zaragoza por la beca de doctorado.

Puesto que cada uno es la suma de sus circunstancias tengo que agradecer también a mis amigos del instituto, en especial a Daniel López y Dámaso Sobejano, con quienes las vacaciones de verano eran auténticas aventuras. El buen ánimo con el que empezaba en septiembre se debe en gran parte a ellos. A Fernando Radigales, por sus grandes lecciones sobre baloncesto y sus incitaciones a correr medias maratones. A Tomas Gutiérrez, por su carácter malagueño y esas jornadas de frontón y papas en el J-85.

A la gente del departamento de Física Aplicada, en especial a Sebastián Jarabo quien ha solventado más de una duda de carácter científico, a la gente del taller, Miguel Carretero, Juanjo, César y Carmen, cuya labor de apoyo es a menudo y desgraciadamente infravalorada. A las secretarias Pilar e Inma sin cuyo trabajo estoy seguro de que la labor investigadora y docente del departamento colapsaría en cuestión de días.

En la parte familiar tengo que agradecer a mi Padre, que ha sido siempre para mí el modelo a seguir, a mi Madre, que no se hace idea de cuánto la quiero. He de pedirles también perdón por los cambios de humor que han tenido que sufrir estoicamente muchas veces sin saber por qué. Espero poder recompensároslo. A mi hermano Óscar le agradezco los buenos momentos de desconexión de sofá y basket así como de la confianza que siempre me ha otorgado. A mi abuela Adela y a mi tía Concha por ser la base de mi rica alimentación canaria durante muchos veranos en la Gomera. A mi abuelo Pascual a quien le debo mucho más que mi nombre.

Por último y sin apenas expresiones que lo puedan reflejar, he de reconocer y agradecer el apoyo de Amaia. Aunque hayamos estado separados por muchas horas de bus, coche y trenes, nunca te he sentido lejos, aunque no hayas tocado una sola fibra cada experimento, resultado y carácter de esta tesis tiene un poco tuyo. Me enseñaste a confiar en mí mismo y a valorar más el esfuerzo que el resultado. Pertsona moduan naizenaren onena zor dizut. Merezi duzun bizi-lagunaren altueran egotea espero dut. Maite zaitut.

Contents

Introduction

Optical Communications

The evolution of the humankind has been linked to the improvement of communications between peers. Starting with the early visual communication with signs and gestures, going through the development of long distance communication with beacon or smoke signals all along the Chinese wall, and finally reaching the actual technology sustained by the modulation of electromagnetic waves. No matter the transmission channel employed, the final purpose is the unambiguous meaningful exchange of information.

All the conceptual models define the different levels of disruption in the communication process as noise. The correct interpretation of the message is the basis of the success in the exchange of information. So forth the health and integrity of the message must be assure through the communication channel. As a result, the monitoring of the quality of the signals becomes a key process for the success of the exchange of information in any communication environment.

In 1966 Kao and Hockham demonstrated the potential of silica glass to guide the light [Kao '66]. Six years later Corning developed the first low-loss optical fiber, marking the beginning of the optical communications era. Nowadays, optical networks have been widely spread in different scales, from the robust submarine cables to the flexible fiber in the fiber to the home (FTTH) architecture. However, the principle of disruptions is still present and with these new scenarios, new challenging noises and impairments have arisen.

Legacy fibers and networks have been historically characterized with off-line methods. The first technologies were more simplistic and rigid, therefore the techniques employed back then were based on an end-to-end characterization of the physical media. In that configuration, the system was fed with a pilot signal that traveled through the different nodes and it was analyzed at the termination end. From the analysis of this trained scenario, the degradation in different configurations was estimated [ITU-T '07]. However, the new optical layer functionalities such as dynamic reconfiguration and flexibility disable the use of these techniques for the performance characterization.

The increasing demand of services in the network forces to upgrade the system to more spectrally efficient modulation formats. The boost of the transmission bit rate comes with a growing number of signal impairments that detrimentally manifest themselves as the network rises its complexity level. High-speed optical signals are more vulnerable to impairments and the induced performance degradations are getting more prominent. Even a weak impairment in the link could severely distort some of the optical properties of the signal and compromise the integrity of the communication link.

Not only the modulation formats experience a constant renovation, the network has also developed the capacity of self-reconfiguring, reaching the qualifications of smart and cognitive networks [Tomkos '12]. Provided with the necessary information, the system is able to establish the optimum path for the transmission, to monitor its own performance and when necessary, to re-adapt its own paths. The final goal must always be to maximize the data transmission with a minimal amount of signal distortion.

Performance monitoring traditionally refers to monitoring in the electrical domain at the SONET/SDH layer for bit error rates (BERs) and other quality-of-service (QoS) measurements. However, electrical transponders for high bit rates (40 Gb/s) are expensive, and the number of transponders can be reduced by using all-optical equipment. [Lachs '98]

This new generation networks with fault management capabilities requires the proper assessment of the signal's health. The monitoring of the signal must also be adapted to these heterogeneous networks. This implies that it must be transparent to modulation and data rate as they might change dynamically between measurements [Dahan '11]. During the past years, more advanced techniques have been developed to provide an accurate and dynamic characterization of the signal quality. Optical performance monitoring has been designated as one of the key enablers of the next generation networks [Saleh '06].

The term Optical Performance Monitoring (OPM) has its first appearance in the literature in the early 1990. All the definitions agree to outline OPM as a physical layer monitoring of the health of the signal [Hill '93]. One of the advantages of monitoring directly the physical layer is the ability of rapidly detecting faults in the transmission. Next generation networks tend to all-optical systems, implying that the signals do not need to be down-converted from optical to electrical domain until they reach the end node. There are no intermediate electrical regeneration points and there must be no electrical diagnose of the degradation at intermediate points neither.

Optical Performance Monitoring modules require only a simple tap of the optical signal, becoming then, non-destructive sensing methods that require only a small percentage of the optical signal. This also loosens any restriction of where it needs to be performed. OPM provides a way to monitor the physical state of the network and the quality of the transmitted data at the same time, avoiding then an over design and inefficient use of network resources. However, OPM techniques must deal with some complications.

Sometimes different OPM parameters require different monitors and this implies a costly technology. The OPM is then constrained by the available technology. The development of functional monitoring techniques requires that these techniques could address the simultaneous measurement of several advanced parameters. Following the fashion of the electronic performance monitoring, the OPM techniques must report average values and high and low tides values, providing thus the required information for the management layer.

This thesis focuses in the study of impairment monitoring for the most common parameters based on all-optical techniques. Here, ultimate features of the Stimulated Brillouin Scattering are studied in the analysis of live signal in order to parameterize the distortion present in the signal.

Motivation

The Photonic Technologies Group started with the characterization of the physical properties of the optical fiber. Later on, with the upgrade of the communications systems and the increase of power transmitted over the fiber, the research was focused on non-linear phenomena present in the optical fiber. In 2002, a new method for high resolution optical spectrum analysis based on Stimulated Brillouin Scattering (SBS) was patented [Pelayo '04]. The group presented the first spurious-free high-resolution optical spectrum analyzer, named BOSA, and exhibited the first prototype in ECOC 2004. One year later the measurement principle and the first applications were published [Subías '05].

With this powerful tool developed within the group, the efforts where then put in understanding the information that could be embedded in the optical spectra. Since the early days of the development of the BOSA, the group has always considered that, the optical spectra may hold more information than what has been used so far.

It did not take long to realize the relationship between the temporal domain and the frequency domain. This powerful tool proved itself essential to characterize light emission sources and to evaluate its performance for telecomm applications. The interpretation of these high-resolution spectra was challenging, the understanding of the information depicted in this new spectra came with further research of the nature of the semiconductor emission.

During the first years, the group focused the research on the characterization of the work parameters of semiconductor lasers, proposing novel characterization methods, and on the measurement of the chirp parameter of different kind of lasers and optical modulators [Villafranca '07]. Throughout these years, several doctoral and masters theses gather all the vast knowledge acquired in the emission source characterization. [Villafranca '08]

In 2010, the group presented a project for new optical performance monitoring techniques. The projects was funded with a research grant from the Spanish National Research Program [MICIN '10]. Based on the vast expertise acquired in the analysis of optical spectra for characterizing the performance of emission sources, the project was focused on developing new techniques that could reveal or monitor the performance of the transmission without need to downgrade the signal to the electrical domain.

At the beginning, we centered our efforts in measuring the optical noise present in the signal. As we were developing new techniques to characterize the polarization impairments of the system, we realized that we had developed a new way to measure the state of polarization across the whole spectra. The direct relationship of these measurements with

the polarization mode dispersion and its importance came quickly to our heads as we struggled before with these parameters in the optical cable processing. The patent was presented in 2012 and approved in 2014 [Sevillano '14].

During the next months until present time, the research line has been centered in making the most out of the spectrally resolved polarimeter designed. Together with Aragon Photonics Lab (APL), the system has been fully implemented in their BOSAs and is now available in its catalog.

This thesis summarized all the work done in the past years in the project framework. The results cover the main highlights achieved and the main drawbacks found, which could inspire future dissertations or theses for others, or at least prevent them for the same mistakes.

Thesis Organization

This thesis presents five chapters and is organized as follows. Chapter I is devoted to the description of the main parameters in optical performance monitoring. A full explanation of the physical phenomena related to the parameters is presented. In this chapter we also analyze the Stimulated Brillouin Scattering and its features that later will be employed along the thesis.

Chapter II describes the measurement of one of the monitoring parameters, the optical signal to noise ratio, for different scenarios. This chapter presents the limitations and drawbacks from the current methods and the advantages that the high-resolution spectral analysis can bring. It also shows the potential of the measurement in trendy technologies in which the optical analysis has not been employed yet.

In Chapter III, it is presented the analysis and measurement of polarization impairments in signals. Based on the polarization properties of the SBS the chapter describes all the steps that led to the development of a new technique for spectrally resolved polarimetry. Here, we explained the theoretical fundamentals and the technical details of the patented device. Results in different scenarios test the performance of the device and shows its potential use.

The main goal in Chapter IV is the design of a OSNR measurements technique that could be employed in polarization multiplexing schemes. For that purpose, the spectral coherence of real traffic signal is analyzed. In this chapter, it is also analyzed the statistic of the registered spectral power for narrow spectral regions in traffic carrying signals.

Chapter V closes this thesis with the global conclusions.

I. Optical Signal Quality Measurement and Monitoring

The list of parameters that might be monitored is extensive, going from simple channel presence monitoring to more complex protocol misalignment. It is common to divide this impairment in two categories, component faults and transmission impairment. Among the second category, two of the most common parameters are the Optical Signal to Noise Ratio and the Polarization Mode Dispersion.[Chan '10]

I.1. Noise and Signal discrimination.

The now distant leap toward the third generation window was based on the possibility of longer distance transmission due to optical amplification. The use of optical amplification significantly reduced the cost of regeneration point which, back then, involved detection, equalization and a new source of transmission. Soon the use of the erbium doped fiber as optical amplifier (EDFA) was massively implanted. The basis of these boost stages is that the Eb^{3+}, when pumped at 980nm or 1480nm, exhibits an overpopulation in the levels $^4I_{13/2}$ than can be used to significantly amplify lightwaves which wavelength lays between 1525 and 1610nmm. This inversion of population of the levels $^4I_{13/2}$ and $^4I_{15/2}$ comes also with an inconvenient spontaneous emission of light in the whole region.

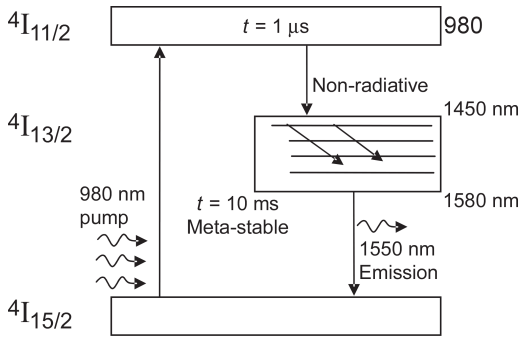

Figure I.1. Simplified energy levels of the Erbium and the transitions involved in the amplification phenomenon.

The spontaneous emission is generated over the whole band. Due to its spontaneous origin, there exists no phase relationship between the generated photons and thus it presents no coherence. This emission is isotropic but part of the radiation does not vanish and is coupled by the fiber and amplified in its path out of the system. The final output of this effect is the generation of incoherent photons that increase the total energy of the output signal but, unlike the stimulated emission, they don't match any of the incoming signal properties. This noise is often referred as amplified spontaneous emission (ASE) and has been a source of study since the implementation of the optical amplification. [Walker '91]

This spontaneous emission has been widely studied and in its most simple version it can be described as:

$$P_{SP} = 2B \cdot n_{sp} \left(G - 1\right) h\upsilon \qquad \text{[I.1]}$$

Where P_{SP} corresponds to the power related with the spontaneous emission, *B* stands for the amplification bandwidth of the Erbium, *G* is the gain at the operation time, h is the Planck constant, ν stands for the optical frequency and n_{sp} is a factor directly related to the population inversion and in most practical cases it is in the region from 2 to 5 [Becker '99]. This model of the emitting noise is widely accepted and it has been used to estimate noise values to design long haul optical networks [Lee '08]. However, it is not suitable in the next generation networks.

When the signal goes through many of these boosting devices, the accumulated noise raises exponentially, increasing then the power density in the fiber and consequently the undesired non-linear effects. Monitoring the amount of noise in the signal gives prior insight of later degradation of the quality of service (QoS) and aids, in the smart reconfiguration process, to avoid further degradation.

The spontaneous nature of the noise makes its spectrum almost flat across the amplification band gap. The stimulated emission on the contrary exhibits a confined spectrum defined by the features of the incoming signal. The Optical Signal to Noise Ratio (OSNR) is one of the most used parameters to measure the accumulated noise in the transmission [Derickson '97]. This parameter has always been easily measured in the optical layer and directly correlated to the bit error rate (BER) [Gumaste '03]. The BER measures the probability of an erroneous bit recovered in a long stream of bits, after it has gone through the physical system. Of course this measurement requires bit time detection and optical to electrical conversion. Although this parameter is the corner stone for QoS analysis, it cannot be monitored continuously as it requires full knowledge of the transmitted channel and therefore it does not stand quick reconfigurations.

OSNR optical monitoring, on the other hand, can be done in parallel to the main link by tapping a small percentage of the transmitted power and requires no more than the optical spectra measurement and its analysis. Although the system is transparent to new modulation schemes and formats, new grid configurations and denser channels multiplexing has proven the present standard insufficient [Kilper '02].

When multiplexed, the channels are coupled in the same fiber going through the different boosting stages and propagating to their final destination. Early standards established the spacing between the optical channels in order to identify them after obtaining the spectrum of the total grid of the WDM. Those spectral gap laying between two adjacent channel exhibit the accumulated noise as there is no original signal placed in these regions. The IEC approved standard for OSNR measurement defines the OSNR as the ratio between the signal present in the channel, and the noise underlying [IEC '92]. This noise value in the channel is interpolated from the value measured out of the channel where it is assumed that there is no signal. The equation includes a bandwidth correction term which purpose is to ensure a standardization of the noise value when measured with different filtering techniques.

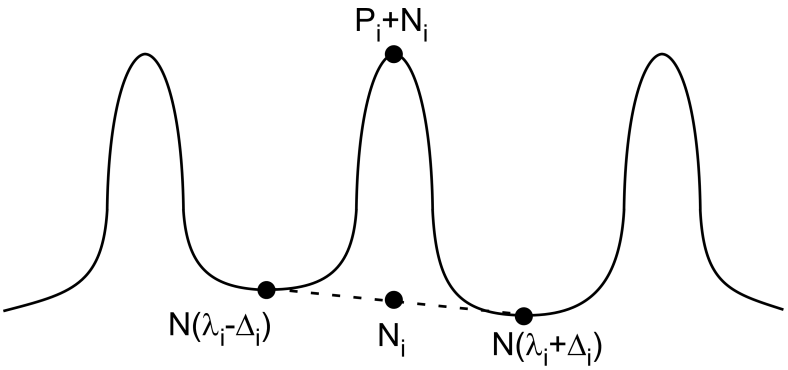

Figure I.2. OSNR measurement based on interpolation

$$OSNR = 10 \cdot \log\left(\frac{P_i}{N_i}\right) + 10 \cdot \log\left(\frac{B_m}{B_r}\right) \quad \text{[I.2]}$$

Where P_i stands for the power of the i-th cannel in linear units, B_m is the measurement bandwidth of the spectra, N_i is the interpolated value of the noise measured with the bandwidth B_m; and B_r is the reference bandwidth which is standardized as 0.1nm or frequency equivalent.

At first sight it can be seen the main drawbacks of this definitions. Not only a flat spectral noise is assumed but also that the spectral regions are reachable. Dense Wavelength Division Multiplexing (DWDM) tests the validity of this statement by allowing a closer position of the channels in the grid.

I.1.1. OSNR in DWDM

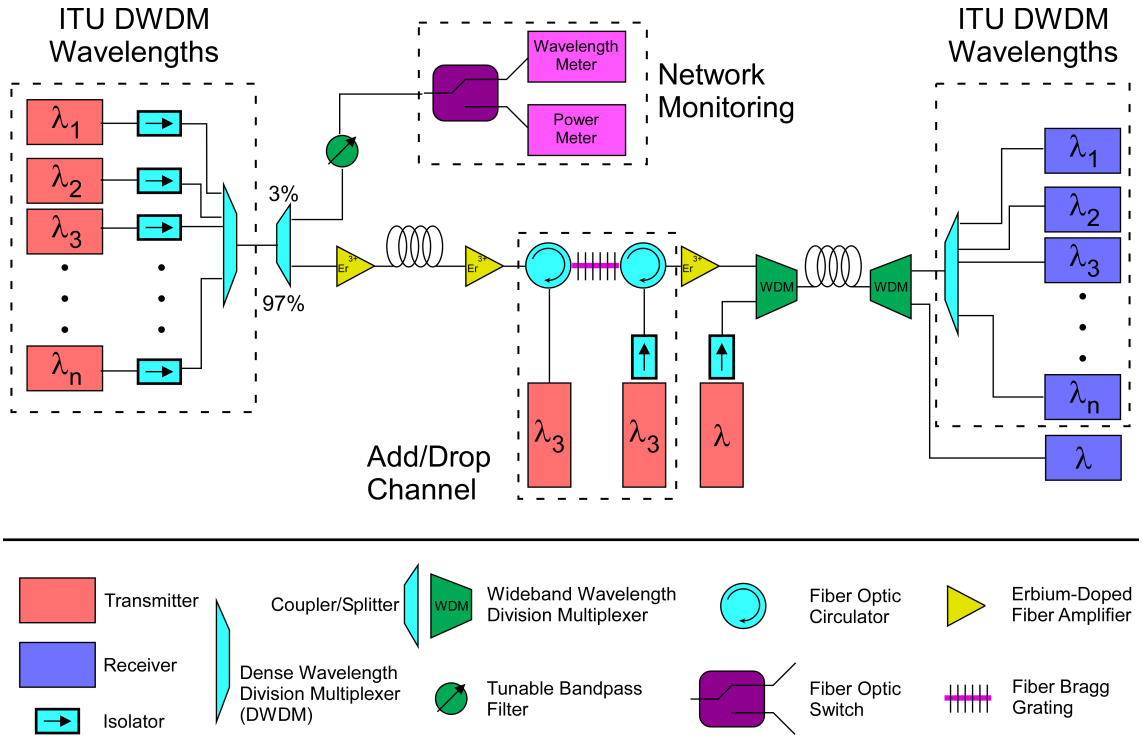

Figure I.3. Schematics of a DWDM architecture with ROADM

The introduction of Dense Wavelength Division Multiplexing increased the number of channel transmitted in the communications bands. This yields also to the reduction of the spectral regions where the noise can be measured. With the advent of new generation networks, the standard OSNR measurement has been proved inefficient. The new schemes present reconfigurable add/drop multiplexers which allow a dynamic reconfiguration of the optical path for any channel in order to achieve the demanded QoS at any time. With this feature, contiguous channels may not share the same path and thus their degradation may not be similar. As it can be seen in fig.I.3 not all the channels go through the same path. This leads to the concept of in-band measurement when referring to new generation networks.

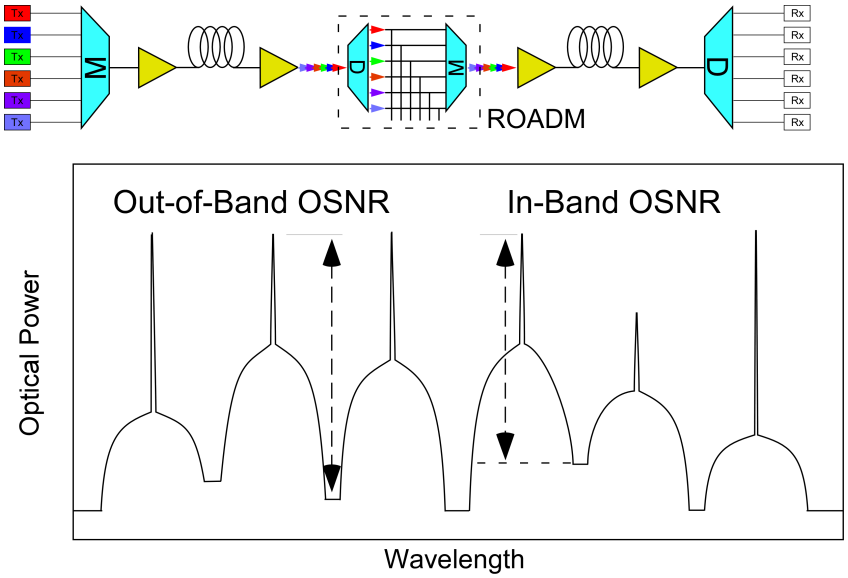

Figure I.4. WDM system with different OSNR values for the different channels showing the differences between Out-of-band OSNR and In-Band OSNR

Now a simple analysis of the optical spectra may not be sufficient to obtain a valid value of the OSNR. Not only has the grid become more packed, but also the noise is filtered and thus it is confined in the spectral region shared with the signal.

The standard assumes, the already obsolete premise, that every channel present in the grid has gone through the same path and thus the same number of boosting points. The implementation of Reconfigurable Optical Add/Drop Multiplexers (ROADM) in the latest years and the dynamic allocation of resources in smart networks have proved this assumption wrong. In the present, each channel can go through different paths and neighbor channels do not need to share the same noise figure as before. This situation is responsible for the coin of the definition of in-band noise measurement.

In fig. I.4, it can be seen an example grid made up by six channels with different OSNR level that requires an individual treatment for a correct monitoring. The in-band measurement implies an identification of the noise level in those spectral gaps where the signal power masks the desired measurement. As this identification must be without access or prior knowledge of the transmitted signal, the measurement principle must be insensitive to configuration parameters and must rely on physical properties that give insight of the noise and signal level.

In order to measure the noise, OSNR techniques must discern the contribution of noise and signal. Besides the traditional interpolation, new techniques have been researched in the recent years, relaying in different principles. Self-Heterodyne Detection has been proposed due to its insensitivity to PMD and other non-linear phenomena [Choi '08] and is based on beat noise analysis estimation between the signal and the noise at the detector. Interferometric techniques exploits the fact that ASE and signal have different coherence and they discriminate the coherent power of the signal from the incoherent power of the noise

[Liu '07]. Methods based on polarization nulling and optical spectrum analysis are well known despite its sensitivity to Polarization Mode Dispersion (PMD) [Lee '01]. The differentiating characteristic there is the polarization. The signal and noise present different origins, the former presents a degree of coherence that can be exploited to its discrimination. This coherence in space and time manifests as a defined polarization, by exploiting this difference, polarization nulling technique can achieve an in-band OSNR measurement. Few years ago our research group presented an alternative implementation of the polarization nulling method, increasing the effective suppression of the polarization nulling, and unaffected by residual PMD.[Jose Martinez '10]

I.1.2. Polarization nulling technique.

Due to its spontaneous origin, the noise accumulated in the network is unpolarized, meaning this that the power is equally distributed in every polarization state. The signal on the contrary has a defined polarization state due to its coherent origin. Polarization nulling methods exploit this difference and, by placing a polarizer previous to the detection stage, the signal component can be nulled by rotating the polarizer until the orthogonal position is reached and thus the signal component suppressed.

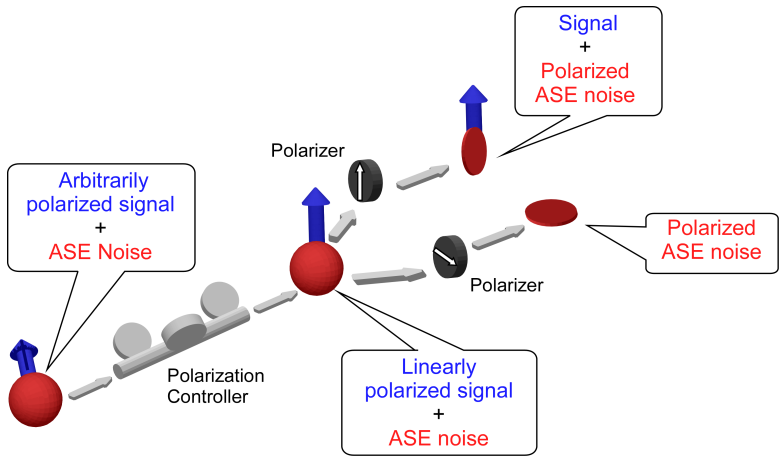

Figure I.5. Schematics of the polarization nulling technique.

Fig. I.5 shows how the extinction of the completely polarized signal can be achieved by performing a rotation of a linear polarizer before the signal is registered by an optical spectrum analyzer. First the signal and the ASE are measured by aligning the polarizer parallel to the signal, and then the polarizer is rotated to its orthogonal state, blocking then the signal completely and enabling the measurement of the underlying noise. In this configuration, some considerations must be taken when measuring the power when the polarizer and the signal are aligned. In that moment, it must be considered that also half of the noise power goes through the polarizer. Also when measuring the situation of signal extinction, the noise measured is half its total power. This is a consequent consideration once a complete depolarization is assumed for the noise.

Based on these principles, this technique requires either a polarization analysis of the signal to know the polarization states in order to align the polarizer perpendicular, or the extinction method must be done by performing a minimum signal search. The former would require filtering and a complete analysis of the signal; the latter would imply a tedious and slow minimum search algorithm.

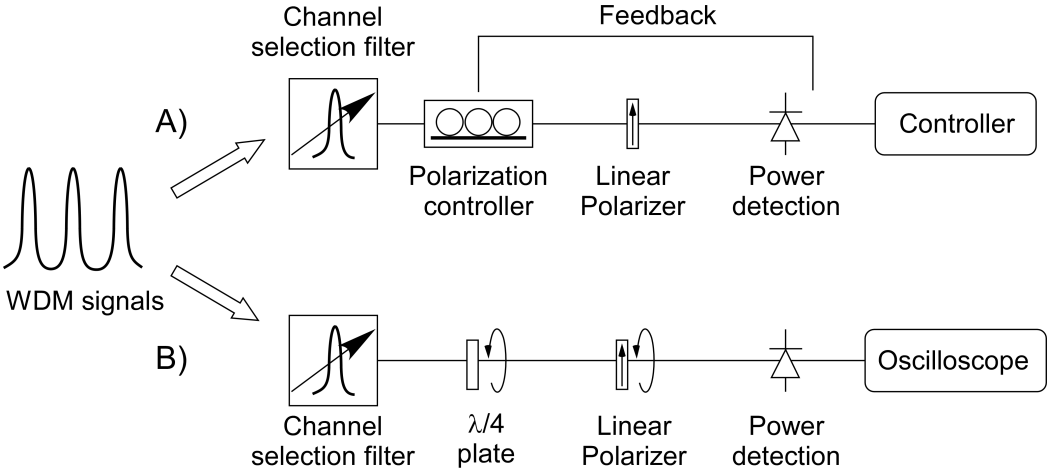

Figure I.6. Polarization nulling based on minimum seek.

This technique is based on a complete depolarization of the noise, which is correct in most of the cases, but also assumes a full polarization of the signal. There are two main scenarios where this condition is not satisfied; the first correspond to signals affected by polarization mode dispersion (PMD). PMD generates a dispersion of the polarization vector of the different spectral components of the signal, which makes it impossible to align the whole signal with a fixed polarizer. Therefore, a full extinction of the signal cannot be achieved.

The second scenario is the polarization multiplexed signal (Pol-Mux). In this case, two signals are multiplexed by modulating two streams of information in two orthogonal states of the same optical carrier. In these cases, even though the laser source is the same, the effect of the modulation, with different bit streams, over the two orthogonal states is the depolarization of the composed signal for times greater than the bit time. This will prevent any kind of controlled suppression of the signal based on its polarization properties.

I.1.3. Pol-Mux

Various methods have been explore to increase the bit/s/Hz ratio in order to increase the final network capacity. Higher modulation rates or increasing the number of channels in the grid yield to a greater complexity and higher non-linear effects in the transmission. Most recently, the new developed modulation schemes implement polarization division multiplexing (Pol-Mux). This has been previously done with the wavelength multiplexing where several channel were transmitted by varying its central wavelength, and thus there would be no cross-talk between them. The pol-mux couples two channels with exactly the

same central wavelength but in an orthogonal polarization so in the reception both channels can be demultiplexed. This modulation format takes advantage of the intrinsic orthogonality of polarized waves such as the wavelength multiplexing did with waves with different central wavelength. [Schonfelder '03]

In these cases polarization nulling cannot recover the noise power because there is always an undetermined projection of the signal in every position of the polarizer. The use of two independent bit streams in two orthogonal polarization states generates a signal which polarization is defined only in the bit-time but depolarized for detection times greater.

Pol-mux proves to be a challenge for optical monitoring, with this modulation schemes the signal loses another distinguishing property such as the polarization, and thus its analysis requires a different approach to reach physical parameters that could be different for signal and noise. The requirement of flexibility for optical monitoring techniques prevents the use of polarization nulling due to the increasing deployment of PolMux.

Without a defined polarization, the signal misses the relationship between the two orthogonal fields and their evolutions. However, each stream of data possess its own coherence. The system still has the ability to interfere with itself. This is due to the coherent nature of the laser and it can be quantified through its autocorrelation function. In chapter 4, a new technique based on this premise is proposed and studied.

In the last years and for the sake of flexibility, new monitoring techniques have focused on the analysis of the sampled amplitude of the signal. Although it was the first parameter used to monitor the degradation, now the efforts are put in loosening the requirement of the synchronous sampling by developing more complex analysis algorithms.

I.1.4. Asynchronous amplitude histograms.

The fundamental monitoring parameter to measure the signal degradation has always been the eye diagram analysis. This representation shows the shape of the transmitted data stream at the receiving point. In the eye diagram, the signal is sampled with an electrical oscilloscope with a lower rate than the signal's rate and then by repeating this sampling the bit shape is reconstructed. In this particular case, the reconstruction of the bit shape requires that the sampling must be synchronized with the signal rate. This implies a clock rate feed for the analysis systems in order to perform this synchronous sampling. [Proakis '01]

Normally, the clock feed is done by recovering it from the main stream with tedious and complex techniques. Based on the eye diagram analysis, a few years ago an asynchronous analysis of the signal was proposed and has attracted significant attention due to its simplicity and remarkable flexibility. [Shake '98]

This asynchronous analysis differs from the common eye analysis in the sampling, as it does not need any clock recovery. This technique potentially reduces the cost of the

sampling analysis as it requires no prior-knowledge of the data rate and thus is flexible for higher rates migration. It is also insensitive to frame format or any other signal structure, requiring only that a continuous bit stream is present for analysis.

Asynchronous histograms are performed at very low data rate and the analysis algorithms are simple enough to be implemented via software. The fig. I.7 displays the difference between the synchronous and asynchronous histograms. In the case, (a) it can be seen that, provided the clock signal, the analysis of the impairments is done by measuring the deformation of the levels of the eye and its transitions.

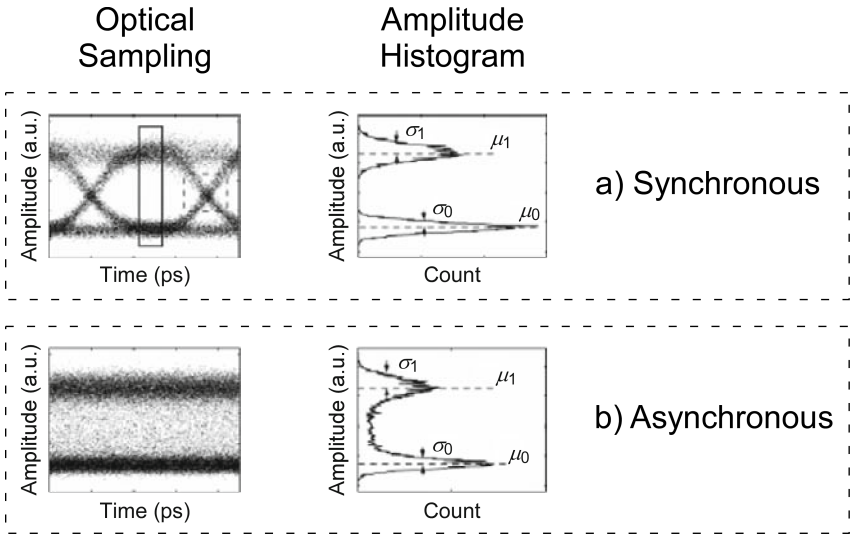

Figure I.7. Synchronous and asynchronous histograms

On the other hand, in fig. I.7(b) we can see a distorted image of the bit shape. In contrast to what happened in the synchronous case, here the separation between the levels of the two states, 1 and 0, cannot be distinguished, as many points were sampled in the transition time between states at different times. Therefore, the transition from the sates cannot be differentiated. However, once the histogram is performed, it can be seen that it presents some features. These features can be related to the distortion present in the signal. Particularly its mean value and variance can be correlated to main distorting parameters.

The analysis of the recovered histograms is usually divided in two methods. In the method A, we start with a reference histogram, which OSNR is sufficiently low and known as it has been previously measured in a calibration stage. Over these histograms, the impact of different levels of OSNR is modelled, these estimated histograms are now compared with the measured histogram. Then, an algorithm is employed so the estimated histogram fits the measured histogram. This algorithm will vary the value of the noise for the reference model until it gets the minimum difference between the estimated histogram and the measured one.

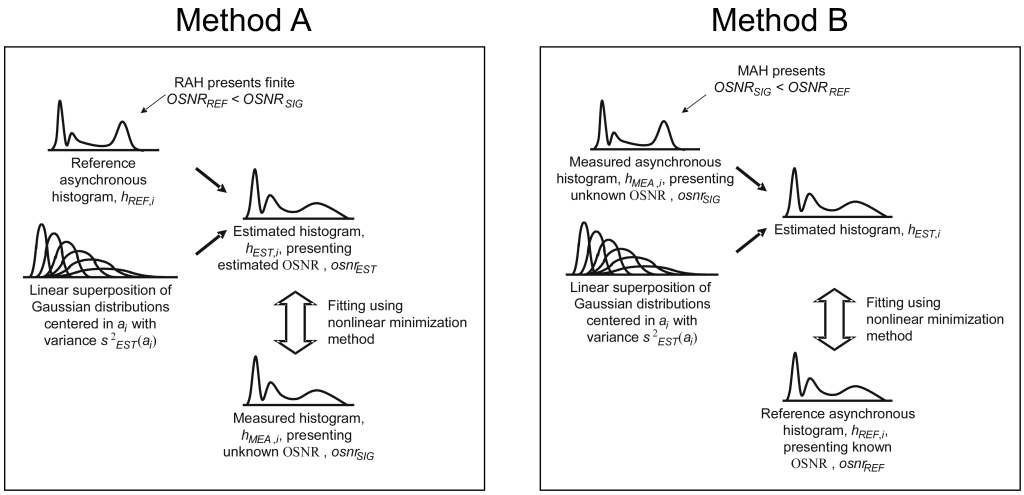

Figure I.8. Different methods for OSNR estimation from asynchronous histograms

In the method B instead of modeling the influence of the noise over a reference histograms, we simulate the effect of different level of Gaussian noise over the measured histogram and compare them with reference histograms with known OSNR that have been previously obtained in calibration stages.

In both methods, the analysis is based on the fitting of a single variable, the value of the OSNR. The first method can be demonstrated to be more efficient for low OSNR while the second one shows better result than the first one for high OSNR values. [Chan '10]

In both ranges this methods presents sensitivity limitations due to the influence of non-signal dependent noise that could be present in the monitoring system, nevertheless it shows a cost-efficient performance [Luis '09]. It is also modulation formant transparent and bit rate independent, and it does not require the costly recovery of the clock signal.

I.2. Polarization Mode Dispersion

I.2.1. Polarization Formalisms

In 1821 Fresnel, enlighten by the experiments of Young, extended the prior work of Huygens in wave theory, explaining the phenomenon of the polarization. He stablished a theory that could explain the prior experiments of Malus and Brewster. He assumed that the electric field has no longitudinal oscillation and only presents transverse components.

$$\vec{E} = E_{0x} e^{i\phi_x} \hat{x} + E_{0y} e^{i\phi_y} \hat{y} \qquad [I.3]$$

There exists multiple ways of representing the electric field [Rogers '08]. The two most common are the Jones space and the Stokes space representation.

In Jones space the electric field is represented as a vector defined in the basis of two orthogonal components perpendicular to the propagation direction. If we assume that the

wave is traveling in the *z* direction, the Jones vector is formed by the complex components, i.e. amplitude (E_0) and phase (φ), of the field in the x and y directions.

$$|E\rangle = \begin{bmatrix} E_x(t) \\ E_y(t) \end{bmatrix} = \begin{bmatrix} E_{0x} e^{i\phi_x} \\ E_{0y} e^{i\phi_y} \end{bmatrix} \quad [I.4]$$

The polarization state in this representation can be extracted from the relationship of the relative phase between the components, $\delta = \phi_x - \phi_y$, and the ratio between their amplitudes. The most common way to depict this representation is the polarization ellipse. Representing the field component in the Cartesian plane, the parameters of the trajectory characterize the polarization state.

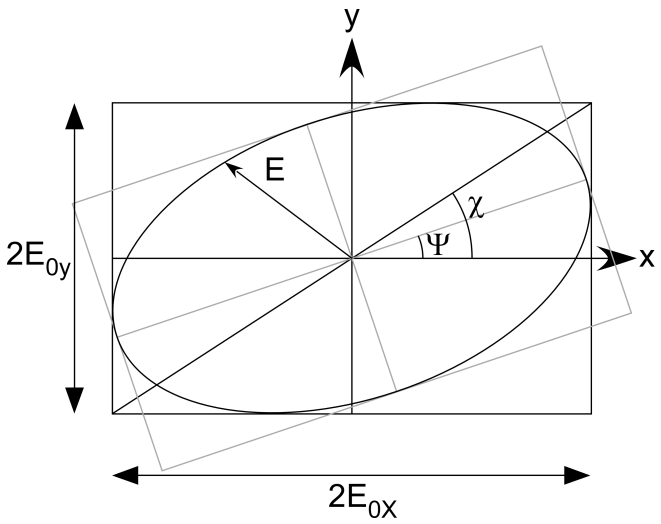

Figure I.9. The Polarization ellipse

In the most general case, i.e. the elliptic polarization state, the angles of the depicted ellipse, χ and Ψ, characterize unambiguously the polarization state of the signal.

$$\tan\alpha = \frac{E_{0y}}{E_{0x}} \quad [I.5]$$

$$\tan 2\psi = \tan 2\alpha \cdot \cos\delta \quad [I.6]$$

$$\sin 2\chi = \sin 2\alpha \cdot \sin\delta \quad [I.7]$$

In the same way that the polarization properties of a propagating wave can be described by its Jones vector, the optical devices can be characterized by its Jones Matrix. This matrix describes how the optical device modifies the polarization properties of the incoming wave. By applying this operator to the jones vector of the incoming wave, the polarization properties of the output wave can be calculated.

$$J = \begin{bmatrix} \rho_{xx} e^{i\phi_{xx}} & \rho_{xy} e^{i\phi_{xy}} \\ \rho_{yx} e^{i\phi_{yx}} & \rho_{yy} e^{i\phi_{yy}} \end{bmatrix} \quad [I.8]$$

$$|E_{out}\rangle = J|E_{in}\rangle \quad [I.9]$$

Although this representation has been proved very intuitional, it assumes a fully defined polarization and lacks explanation for the depolarization phenomena. The concept of depolarization appears when considering non perfectly monochromatic waves or time integration in the detection. Stokes presented in 1852 a more general description based on the intensity that could cover the non-polarized or partially polarized cases.

The Stokes space is a four-dimension scalar space which parameters are based on intensity instead of the complex electric field. In this case the first of the Stokes parameters, S_0, accounts for the total intensity while the others account for the proportion of signal in a three basis axis; (S_1,S_2,S_3). The first component of the basis, S_1, accounts for the difference between vertical and horizontal component, the second component, S_2, for the difference between signal at 45deg and 135deg, and the last one, S_3, accounts for the difference between right hand circular and left hand circular component.

$$\begin{aligned} S_0 &= I_0 + I_{90} = I_{45} + I_{135} = I_{RHC} + I_{LHC} \\ S_1 &= I_0 - I_{90} \\ S_2 &= I_{45} - I_{135} \\ S_3 &= I_{RHC} - I_{LHC} \end{aligned} \quad [I.10]$$

Their relation with the electrical field can be expressed as [Collett '05]:

$$S = \begin{pmatrix} S_0 \\ S_1 \\ S_2 \\ S_3 \end{pmatrix} = \begin{pmatrix} E_{0x}^2 + E_{0y}^2 \\ E_{0x}^2 - E_{0y}^2 \\ 2E_{0x}E_{0y}\cos\delta \\ 2E_{0x}E_{0y}\sin\delta \end{pmatrix} \quad [I.11]$$

As the first component , S_0, represents the total light, it can be measured in any orthogonal pair of axis and thus its value will always be grater or equal than the norm of the vector made up by the components in the three axis. The depolarization will be then this difference.

$$S_0^2 \geq S_1^2 + S_2^2 + S_3^2 \quad [I.12]$$

Normally, the parameters (S_1,S_2,S_3) are normalized with respect to S_0, and thus in the case of fully polarized light their value ranges from 0 to 1.The Stokes parameters often come with a representation of the polarization in the Poincare sphere. In this 3D depiction, the poles of the sphere represent circular polarization states while linear polarization states

lay in the equatorial plane. The length of the vector is related to the inequation [I.12], as it would go from 0, in totally depolarized, to 1 in fully polarized signal, reaching the surface of the sphere.

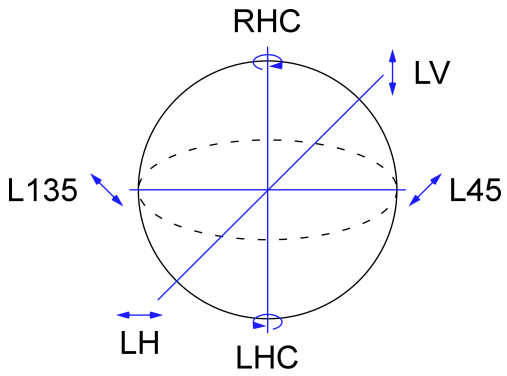

Figure I.10. Poincare sphere

The angles formed by any vector in the Poincare sphere are directly related to the angles that defined the ellipse in the Jones space and thus they can be used to unambiguously describe any polarization state.

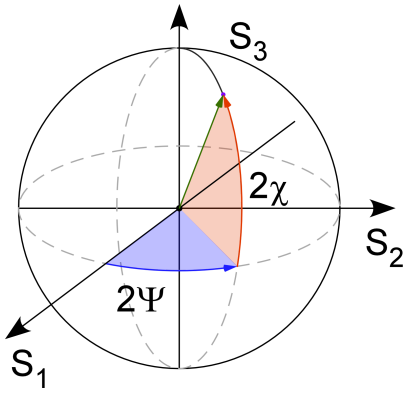

Figure I.11. Ellipse's angles in the Stokes space

$$\left.\begin{aligned} S_1 &= S_0\cos(2\chi)\cos(2\psi) \\ S_2 &= S_0\cos(2\chi)\sin(2\psi) \\ S_3 &= S_0\sin(2\chi) \end{aligned}\right\} \quad \begin{aligned} \psi &= \frac{1}{2}\tan^{-1}\left(\frac{S_1}{S_2}\right) \\ \chi &= \frac{1}{2}\sin^{-1}\left(\frac{S_3}{S_0}\right) \end{aligned} \qquad [I.13]$$

The relationship stated above proves that the polarization state of the signal can be completely determined through the Stokes parameters. These parameters can be obtained by performing the measurement of the intensity of the signal in the mentioned six states. This implies that a scalar measurement of the intensity in six different states can fully describe the polarization of the signal.

Polarimetry often employs Stokes space representation for two reasons. First, it is an intensity-based representation and most of the detector are intensity photodetector, hence

there is no need for complex operation to obtain the Stokes parameters. The second reason is that it is connected with the Mueller calculus, which affords a superb mathematical framework for calculating the response of optical devices and their effect on fully or partially polarized light. This is especially significant when describing the behavior of optical devices such as optical phase retarder.

I.2.2. Polarization evolution in fibers

The exact solution of the wave equation in the optical fiber with different refractive index for the core and the cladding, n_{co} and n_{cl}, is made up by six field components, i.e. E and H in the x,y,z directions. These propagation modes are discrete and hybrid because each one consists of all six field components and possess no circular symmetry. Normally the system can be greatly simplified by assuming the so-called "weakly guiding approximation", n_{co}-n_{cl}<1, and thus the longitudinal field components are neglected. This assumption leads to the approximate mode solutions defined as linearly polarized LP modes. In isotropic media, the fundamental mode LP_{01} is degenerated and two modes LP_{01}^{x} and LP_{01}^{y} can be guided with the same propagation constant [Keiser '10].

In case of single-mode fibers, the indexes, n_{co} and n_{cl}, are set to guide only the fundamental and lowest order modes. In the case of circular cores with perfect angular symmetry, the fundamental HE_{11} in the general case is the same solution as the LP_{01} in the weakly guided case and thus it supports two degenerated modes. The solution exhibits an amplitude with a revolutionary symmetry that can be polarized in X or Y axes with the same propagation constant β. This statement implies that for this fundamental mode the fiber guides any polarized state unaffected through all its length, reaching the furthest point in the same original mode and thus with the original polarization state. However, the fiber present asymmetries in the circular core and cladding which leads to a differential propagation of the different modes and thus a differential evolution of the polarization states across the fiber.

The most common and simple way to describe the evolution of the polarization in the fiber is to consider the whole fiber as a concatenation of infinitesimal trunks of fiber. In each of the trunks, the differential evolution of the field is given by the wave equation:

$$\frac{d^2\boldsymbol{E}}{dz^2} + \varepsilon k_0^2 \boldsymbol{E} = 0 \qquad \text{[I.14]}$$

Where k_0 is the propagation constant and can be expanded:

$$\varepsilon k_0^2 = \beta_0^2 I + \beta_0 \vec{\beta}\cdot\vec{\sigma} = \beta_0^2 I + \beta_0 \begin{pmatrix} \beta_1 & \beta_2 - j\beta_3 \\ \beta_2 + j\beta_3 & -\beta_1 \end{pmatrix} \qquad \text{[I.15]}$$

The $\vec{\beta}$ vector accounts for the birefringence of the fiber in the three basis of the Stokes space. β_o stands for the ordinary propagation constant and $\vec{\sigma}$ is the pauli matrix tensor for projections between Jones and Stokes spaces.

Now decoupling the temporal evolution of the electric field, the solution for the eq [I.14] can be represented as:

$$\boldsymbol{E} = E_0 e^{-i\beta_0 z} \left| s \right\rangle \qquad [I.16]$$

Where the vector $\left| s \right\rangle$ represents the SOP vector in the Jones space. Replacing this solution, the evolution of the orientation of the electric field can be describes as:

$$\frac{d\left| s \right\rangle}{dz} = -\frac{1}{2} i \left(\vec{\beta} \cdot \vec{\sigma} \right) \left| s \right\rangle \qquad [I.17]$$

Thus, the evolution of the vector for an infinitesimal length can be approximated as:

$$\left| s\left(z_0 + \Delta z \right) \right\rangle = \left| s\left(z_0 \right) \right\rangle \cdot \exp\left(-\frac{1}{2} i \left(\vec{\beta} \cdot \vec{\sigma} \right) \Delta z \right) \qquad [I.18]$$

Expanding the value of the exponential, the equation [I.18] can be rewritten as:

$$\exp\left(-\frac{1}{2} i \left(\vec{\beta} \cdot \vec{\sigma} \right) \Delta z \right) = \cos\left(\boldsymbol{\beta} \cdot \Delta z \right) I + i \frac{\sin\left(\boldsymbol{\beta} \cdot \Delta z \right)}{\boldsymbol{\beta}} \left(\vec{\beta} \cdot \vec{\sigma} \right) \qquad [I.19]$$

Where **β** accounts for the modulus of the birefringence. This equation represents the unitary matrix that determines the evolution of the polarization for an infinitesimal portion of fiber, T(Δz) defined as the unitary transmission matrix in Jones space. This approximation is valid only in those regimens in which the birefringence can be considered constant .

$$\left| s\left(z_0 + \Delta z \right) \right\rangle = T\left(\Delta z \right) \left| s\left(z_0 \right) \right\rangle \qquad [I.20]$$

Due to its unitary properties, the final matrix will be a concatenation of independent matrixes describing the evolution in the different trunks.

This evolution described above is more explicit when expanded in the Stokes space. The Stokes representation of Jones space vector can be performed by using the Pauli matrixes and its identities [Gordon '00].

$$\hat{s} = \left\langle s \left| \vec{\sigma} \right| s \right\rangle \qquad [I.21]$$

The evolution of the polarization expressed in the Stokes domain can be then written as:

$$\frac{d\hat{s}}{dz} = \frac{d\langle s|}{dz}\vec{\sigma}|s\rangle + \langle s|\cdot\vec{\sigma}\frac{d|s\rangle}{dz} \quad [I.22]$$

Now substituting the evolution of the jones vector and using the identities, it can be obtained that the spatial evolution of the stokes vector across the length of the fiber follows:

$$\frac{d\hat{s}}{dz} = \vec{\beta}\times\hat{s} \quad [I.23]$$

This equation relates the evolution of the polarization vector across the fiber to the birefringence of the fiber.

If we go back now to the equation [I.20], the propagation matrix can be written as:

$$T = e^{-i\phi_0}U \quad [I.24]$$

Being ϕ_0 the common phase due to propagation. Now if we differentiate with respect to the frequency having in account the expression:

$$\frac{d|s(z)\rangle}{d\omega} = e^{-i\phi_0}\left[-i\frac{d\phi_0}{d\omega}U + \frac{dU}{d\omega}\right]|s(0)\rangle \quad [I.25]$$

This evolution can be rewritten as:

$$\frac{d|s(z)\rangle}{d\omega} = \left[-i\tau_0 + \frac{dU}{d\omega}U^*\right]|s(z)\rangle \quad [I.26]$$

Where τ_0 is known as the mean group delay and it is defined as the frequency derivative of the common phase ϕ_0 .Finally if we apply the same differentiating rule that was used above:

$$\frac{d\hat{s}}{dz} = \frac{d\langle s|}{d\omega}\vec{\sigma}|s\rangle + \langle s|\cdot\vec{\sigma}\frac{d|s\rangle}{d\omega} \quad [I.27]$$

Neglecting the dependence of the refractive index with the frequency. The evolution of the polarization in the Stokes space can be simply expressed as.

$$\frac{d\hat{s}}{d\omega} = \vec{\Omega}\times\hat{s} \quad [I.28]$$

According to the expression [I.28], any birefringence in the fiber would induce a different evolution of the polarization state for the different spectral components. There exist special orthogonal pairs of polarization at the input and the output of the fiber called the principle states of polarization (PSP). These PSPs have group delays, τ, which are the maximum and minimum mean time delays in the time domain view. The difference between

these two delays is called the differential group delay (DGD). When light is lunched into the fiber with a SOP matching one of the PSP, its polarization remains constant across the fiber and exits with its same SOP. The Ω vector describes both the PSPs and the DGD in the fiber. It is a Stokes vector pointing in the direction of the slow PSP with a length equal to the DGD induced by the birefringence. The evolution described in [I.28] can be easily identified as a rotation of the polarization stokes vector $\hat{s}$ around the Ω vector defined by the differential group delay established by the birefringence.

The equations [I.23] and [I.28] state the analogy between the polarization evolution across the space and its dependence with the frequency. Obviating a common factor and assuming that the birefringence can be considered independent with respect to the wavelength, both equations show a similar behavior.

Equation [I.28] can be tested by coupling into a single mode fiber, two narrow emission sources with similar polarization states and different emission wavelength. After a sufficient long path, the relative orientation of their polarization states changes, and thus interference phenomena in which polarization is involved can be neglected.

I.2.3. Polarization mode dispersion

In terrestrial optical transmission, this problem becomes relevant when the emission source is pulsed for codification and thus the spectra broadened. In the temporal domain, the effect of the birefringence can be easily depicted expressing the signal in the basis defined by the principal states of polarization. The evolution of the component of each axis is ruled by its propagation constant. This yields then to a delay between the projections of the pulse in each axis. The final effect of this differential evolution is the temporal broadening of each pulse.

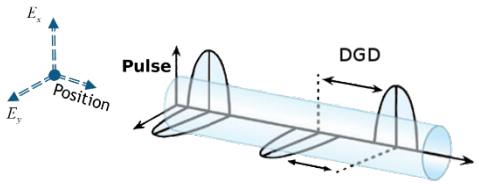

Figure I.12. Differential Group Delay in the time domain

In the frequency domain, the width of the signal spectra is inversely proportional to the duration of the pulse. When guiding a polarized pulsed signal through fiber with non-zero birefringence, after a sufficient distance, the polarization states for the different spectral components of the pulse will have different relative polarizations.

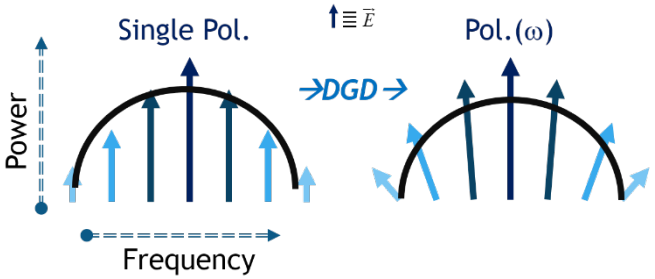

Figure I.13. Differential group delay effect in the frequency domain.

In the case of the pulsed transmission, the shorter the pulse the wider the spectra and thus the more affected it becomes. The dispersion of the polarization vector that can be seen on the spectral domain reflects the distortion level of the signal.

Due to its inherent nature, the DGD is not a static value, slight fluctuation in the transmission conditions can change the relative orientation between the birefringence axis and the signal. Occasional stresses in the fiber can induce a temporary change of the magnitude and orientation of the birefringence over a certain length of the fiber. It can be demonstrated that, at the end, the expected value of this delay, when generated after travelling through a sufficient length of fiber, follows a Maxwellian distribution over a mean value, and escalates with the increase of the length as a random-walk process. This statistical value is known as the polarization mode dispersion (PMD) value of the transmission. Usually the most expected value of the Maxwellian distribution is used as the final parameter [FERREIRA '05]. This value does not represent the actual degradation of the signal rather than the mean degradation expected due to fluctuations.

The DGD is then the fundamental measurement to assess the polarization impairments present in the signal due to the propagation in the fiber. As we have seen in the fig. I.13 this is represented as a walk-off of the polarization vector across the spectra of the signal. This leads to think that in the opposite way, the analysis of the polarization state of the spectral component of the signal gives information about its differential group delay. By performing a polarimetry in the spectral domain, we could characterize the instantaneous DGD present in the signal.[Nezam '04] .

Historically, the PMD has only been a matter of concern in the cabling process of the fiber because it was the only stage in which high-PMD values could be induced to affect 10G or lower. Nowadays, it is gaining attention as the data rate grows. With the upgrading to 40G and 100G, the tolerance decrease by a factor 4 and 10, respectively. The PMD must be now monitored in live signals and its compensation is a matter for multiples studies. In table 1 are represented the PMD values tolerated for different modulation formats at different rates.

Data Rate	Modulation Format	PMD Tolerance (ps)
10	NRZ-OOK	32
	RZ-OOK	40
	CSRZ-OOK	44
	DB	24
40	NRZ-OOK	8
	RZ-OOK	10
	CSRZ-OOK	11
	DB	6
	NRZ-DPSK	10
	RZ-DPSK	10
	NRZ-DQPSK	20
	RZ-DQPSK	21

Table 1 PMD tolerance limit for direct detection systems.

I.2.4. PMD Monitoring.

State-of-the-art monitoring techniques for PMD in non-coherent conventional modulation schemes can be divided in three main categories according to the operating principle.

Post-filtering RF analysis are based on the measurement of the efficiency of the beat between different components of the spectra [Luo '05]. Due to the different speed for the two PSP in the fiber, a dephase between these two states appears. The value of the detected power of the beating is then related to this dephase produced by the birefringence of the fiber. The main disadvantage of the technique based in this principle is that several other dispersive impairments distort the beating efficiency and thus create an ambiguity. Chromatic dispersion also induces a dephase between two separates RF components due to the different refractive index for different wavelength, and it affects the value of the final power detected. Although these technique seems to be useless for modulation schemes that do not present clock tones, such as NRZ, several alternatives that overcome this limitation have been proposed. Furthermore, there have been published different set-ups than claim to separate PMD and CD contributions, however they can only be applied for specific modulation formats and limited global impairments requiring high-speed devices. [Yang '07]

Electrical signal analysis techniques are based on the analysis of the signal quality after the optical to electrical conversion in the receiving end. The most employed techniques are based on the eye pattern analysis [Buchali '02]. The eye pattern depicts a synchronous sampling of the amplitude distribution after receiving multiple bits. In this depiction, the shape of the received bits and its transition from “0” to “1”, and vice versa can be analyzed. Based on the distortion present in this eye, the dispersive impairments can be monitored. As the RF tone analysis, it is hard to isolate the contributions of each one of the possible distortion. The limitations of these techniques are the clock recovery and the fast and

expensive electronics that it requires. However, there has been growing interest in novel techniques that do not require the clock signal fed to the analysis system. As for the OSNR, the distortion due to the PMD can be evaluate from the asynchronous amplitude histograms, but in this case, the optical waveform is sampled in pairs separated by a known physical delay which is not related to the rate. This plot is called phase portrait and although it is as complicated to understands as the eye diagram, it contains the same information without the need for clock recovery. Unfortunately, it also presents the same inconvenient lack of ability to isolate the source of distortion.[Chan '10]

The last worth mentioning technology is based on the measurement of the degree of polarization. These techniques evaluate the depolarization suffered by the signal after travelling through the birefringent media. As it can bee seen in fig. I.13, the final effect of the different refractive index for the different PSP is a differential evolution of the SOP across the signal bandwidth. When the signal present no PMD distortion, it can be considered fully polarized and the degree of polarization (DOP) equal to one. The decrease of the DOP of the signal corresponds to the distortion caused by PMD. The simplicity of the system makes it a good candidate for PMD monitoring and it also does not require high-speed devices or prior information of the modulation schemes and it is not affected by other dispersive impairments such as PMD. Among these three technologies, this is the only one that can be performed in the optical domain without the need for demodulation.

However, this kind of analysis is limited by its sensitivity, which depends on the modulation format. It also have a limited measurement range, which depends on the rate, and finally its performance can be severely affected by high-order PMD. In order to overcome these drawbacks, an enhanced modification can be employed. This technique is the State of Polarization (SOP) evolution monitoring [Xia '12], and it is based on the identification of the polarization plane with the highest delay between orthogonal polarizations for a given signal under test (SUT). However, all published methods based on resolved polarization analysis of the signal spectrum require either previous alignment of the system, or manipulation of the signal SOP [Roudas '04][Moller '01], thus limiting the measurement to individual channels.

In chapter 3, we present an alternative technique, based on the SOP evolution analysis but with a higher resolution aided by the SBS, that presents all its mentioned improvements and overcomes the need for alignment or polarization controlling over the signal.

I.3. Stimulated Brillouin Scattering

Optical spectrum analysis can be performed with a wide range of filtering techniques [Campos '04] [Vandeventer '91] [Baney '02]. However, the aimed performance narrows the number of candidates. Based also on the acquired experience with non-linear effect, the

stimulated Brillouin scattering has been employed to carry out most of the work done in this thesis.

I.3.1. Scalar theory

The Brillouin scattering takes place when an optical wave travelling through an optical fiber reaches certain threshold power determined by the nonlinear properties of the fiber. This high intensity wave, aided by electrostrictive forces varying in time, generates a pressure wave that travels along the fiber. The propagation of this pressure wave generates a periodic and travelling variation of the refractive index across the fiber. This modulation of the refractive index can be seen as a travelling Bragg grating at the speed of this acoustic wave. The phenomenon exhibits a Stokes backward propagation wave which frequency is downshifted in relation to the frequency of the travelling acoustic wave in the media. This frequency shift is known as the Brillouin frequency and described as:

$$\upsilon_B = 2n_p\upsilon_A/\lambda_p \qquad \text{[I.29]}$$

Where n_p in the refractive index of the fiber at the frequency of operation, v_A is the velocity of the acoustic wave in the fiber, and λ_p is the wavelength of the signal.

When a second optical wave is present, the phenomenon is said to be in the stimulated mode. This case presents maximum efficiency when both signals are counterpropagating. In this mode, the second optical signal is known as probe, and the high intensity signal as pump. When the difference between their central frequency matches the Brillouin shift, the coupling between them and the acoustic wave is maximum. Resulting then in an increase of the probe energy at that frequency, proportional to its original density of power and other factors depending on the fiber. This effect can be easily described as the resonance in which a photon from the pump is transformed into and acoustic phonon and a photon of the Stokes wave at the probe frequency.

$$\omega_P = \omega_S + \omega_A \qquad \text{[I.30]}$$

In the stimulated case, the evolution of the pump and probe is coupled, as explained above. The most common description of the spatial evolution of these waves is presented as:

$$\begin{aligned}\frac{\partial P_P}{\partial z} &= -\alpha P_P - g_B P_S P_P \\ \frac{\partial P_S}{\partial z} &= \alpha P_S - g_B P_S P_P\end{aligned} \qquad \text{[I.31]}$$

Where P_p stands for the pump power, P_s is the probe wave, α is the attenuation coefficient and g_B is the Brillouin gain. Here it can be seen that the gain is exponential. This gain coefficient can be described in terms of the physical parameters of the fibers:

$$g_b = \frac{8\pi^2 \gamma_e^2}{n_p \lambda_p^2 \rho_0 c \cdot \upsilon_A \Gamma_B} \quad [I.32]$$

Where γ_e stands for the electrostrictive constant of the silica, n_p stands for the refractive index at the pump frequency, λ_p corresponds to the pump wavelength, ρ_0 is the density of the silica, Γ_B is the inverse of the lifetime of the phonon and ν_A is the frequency of the acoustic wave.

This interaction between the pump and the probe takes place only when their frequencies satisfy the matching condition aforementioned. This limitation generates an efficiency profile of the Brillouin amplification depending of the frequency of the probe describes as:

$$g_B(\omega) = \frac{g_b (\Gamma_B/2)^2}{(\omega - \omega_B)^2 + (\Gamma_B/2)^2} \quad [I.33]$$

Where ω_B Stokes frequency. This equation indicates that the Brillouin profile presents a Lorentzian profile which full width at half maximum (FWHM) corresponds to Γ_B. In standard single mode fiber this values is widely accepted as 10Mhz. The equation [I.33] determines the dependence of the gain with respect to the physical parameters. Due to its interferometric origin, the interaction between these two waves depends on their relative polarization.

I.3.2. Vector Brillouin Properties

As any other interference phenomenon, the final efficiency depends on the relative polarization between the coupling waves. When the probe and pump match the conditions for the Stimulated mode, the final gain of the former will depend on their relative polarization states along the fiber.

This polarization dependence of the Brillouin gain arises from the absence of the phenomenon when the pump and signal under test (SUT) fields are orthogonal. When this phenomenon takes place along a guide where they both are confined, such an optical fiber; the different polarization states of both, signal and pump, evolve, and thus, their relative orientation in every moment must be considered for the evaluation of the final gain and the final polarization state of the amplified probe signal.

The propagation of the signal across the fiber can be describes as:

$$\vec{E}_{sig}(z) = \mathbf{T}(z)\vec{E}_{sig}(0) \quad [I.34]$$

Where the $\mathbf{T}$ matrix describes the whole evolution in the fiber for a length z. The propagation of the pump in the opposite way, and obviating wavelength dependences, is then described as:

$$\begin{aligned}\vec{E}_{sig}(0) &= \mathbf{T}^{T}(z)\vec{E}_{sig}(z)\\ \vec{E}_{pump}(z) &= \mathbf{T}^{*}(z)\vec{E}_{pump}(0)\end{aligned} \qquad [I.35]$$

Introducing this spatial evolution of both fields, the formal approximation, described in prior section in a scalar way, can be now rewritten in vector terms as:

$$\begin{aligned}\frac{d\vec{E}_{sig}(z)}{dz} &= \left[\frac{d\mathbf{T}(z)}{dz}\mathbf{T}^{\dagger}(z)+\frac{\gamma_0}{2}\left[\vec{E}_{pump}(0)\vec{E}^{\dagger}_{pump}(0)\right]\right]\vec{E}_{sig}(z)\\ \frac{d\vec{E}_{pump}(z)}{dz} &= \left[\frac{d\mathbf{T}^{*}(z)}{dz}\mathbf{T}^{T}(z)+\frac{\gamma_0}{2}\left[\vec{E}_{sig}(0)\vec{E}^{\dagger}_{sig}(0)\right]\right]\vec{E}_{pump}(z)\end{aligned} \qquad [I.36]$$

Reformulating the equations in this form, it can be clearly seen how the ultimate gain factor would depend on the relative polarization between the pump and the signal at every time. However, when the scattering takes place in a spool of fiber, both fields experience the same evolution of their SOP along the fiber with respect to their original states. A straight thought would lead to a misconception if one thinks that then the relative orientation would be always the same. As they propagate in opposite direction, their evolution will not be the same. In linearly polarized states they keep their relative polarization state, and thus if they are parallel in one position they remain parallel in the next place where their state of polarization is linear. Nevertheless, as they propagate in opposite directions when they reach the circular states they both will evolve to the orthogonal circular states, i.e. dextrorotary and levorotary, from the same previous linear state. The opposite behavior takes place when both states are orthogonal in linear states, which corresponds to absence of phenomenon, but when they reach the circular polarization state, they arrive at the same orientation, dextro or levo, and thus become parallel.

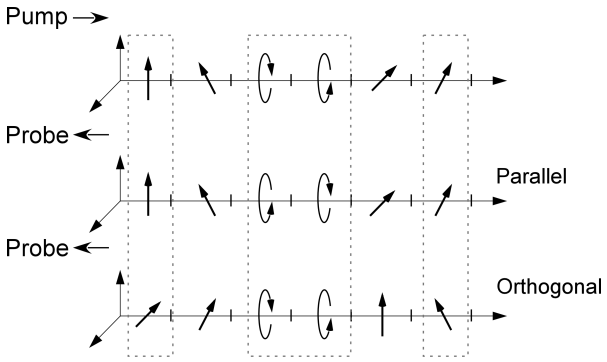

Figure I.14. Representation of the evolution of the SOP for pump and signal across the fiber. The probe evolution is plotted from the orthogonal and parallel states relative to the pump at the injection point.

In long enough length of fiber, both will experience the same amount on time in all possible states and thus it can be defined an effective gain [Zadok '08]:

$$\gamma_b = \frac{\gamma_0}{2}\left(1+\left\langle \hat{s}_p \cdot \hat{s}_{SUT} \right\rangle_L\right) \qquad [I.37]$$

The two vectors stand for the Stokes space representation of the SOP for the pump and the SUT. The function γ_0 stands for the well-known Lorentzian shape dependence of the gain with the frequency, and depends on the pump laser power lever and physical factors of the fiber, such as the electrostrictive constant of the fiber or its density [Govind P. '06a]. The length-averaged dot product of both vectors along the fiber has been proved to vary from minus one third, when they are orthogonal in one end, to one third, when they are parallel [van Deventer '94]. The equation for γ_b describes the gain function dependence on the polarization state of the pump in the Stokes space.

So the SBS can be treated as a polarization selective element that presents two different gains for the states parallel and perpendicular to the pump when it is injected in the spool of fiber. Besides this dependence, the filter presents the aforementioned wavelength selectivity. Therefore, the gain function of the filter when used to scan the spectra can be written as:

$$G(\omega) \propto \exp\left[\hat{s}_{SUT}(\omega, z=\mathrm{L}) \cdot \vec{g}(\omega, z=L)\right]^{1/2} \qquad [I.38]$$

This different value of the gain for two orthogonal polarization states respect to the pump yields to a different final output value of the amplified spectral component when it exits the fiber depending on its income polarization. For high enough power of the pump this gain difference can be considered as an effective rejection ratio between these orthogonal states that depends on the range of powers [Wise '11]. To verify the suitability of the effect as a polarization discriminator the different gain for perpendicular states was measured. To do so, one monochromatic signal is measured after it is amplified with a static polarization pump.

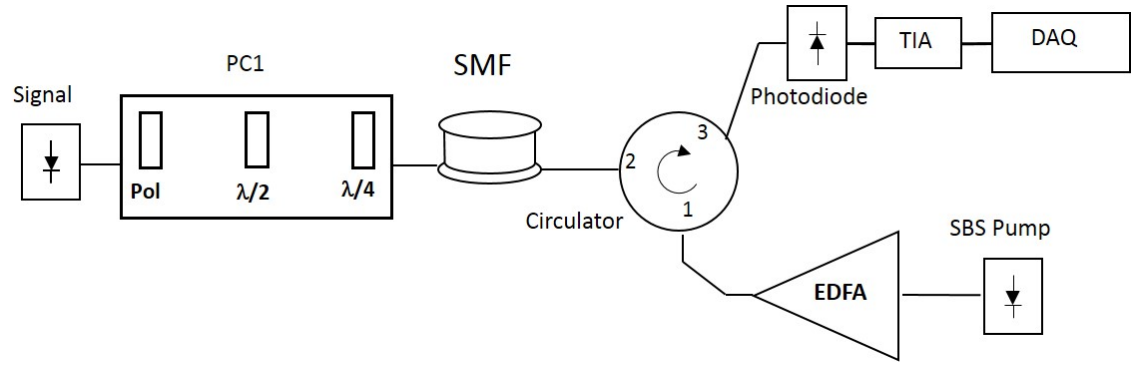

Figure I.15. Schematics for the polarization extinction ratio of the SBS filter.

This amplification is optimized when the signal frequency matches the emission frequency of the pump minus the Brillouin shift frequency. The amplified power value is recorded for different signal power values, and for two polarization states; one where the signal and the pump are orthogonal, and thus the registered value is minimum, and the other power is registered when the signal is rotated to its perpendicular state. An automatic polarization controller was employed to search for the polarization state in which the signal has its minimum amplification.

Once the conditions were optimal to reach the minimum amplification, the needed values to rotate to the orthogonal position of the signal were calculated and set with the same polarization controller. In fig. I.16, it is depicted the different gain for the polarization states parallel and perpendicular to the pump for an static polarization pump which output power was amplified by an EDFA and set according to the length of the spool of fiber. It can be seen that in the range from -50dBm to 0dBm the system performs a greater than 20dB discrimination. This performance has been already used to design enhanced optical filtering [Wise '11].

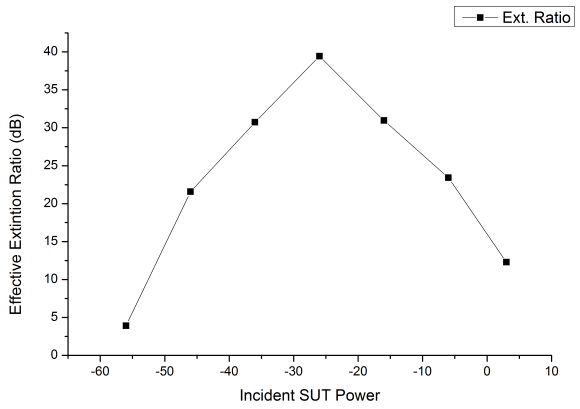

Figure I.16. Extinction ratio between incident signals parallel and perpendicular to the pump for several signal income power.

I.3.3. Brillouin Optical Spectrum Analyzer. BOSA

As it has been said, it is not strange to find in the literature the description of the SBS as a travelling Bragg grating within the fiber. However, unlike these passive gratings which block the power out of the filter's bandpass region, here the SBS highly amplifies the power within the bandpass region. Normally, in filtering techniques there is a trade-off between the width of the filter and the measurable optical power, i.e. the spectral resolution and the sensitivity. When the filter's width is very narrow, low levels of power reach the detector after the filter, and thus, it is harder to measure their value. Due to its active gain, the SBS amplifies the filtered component making it easier to measure low power values.

The full description of the SBS as an optical active filter for high-resolution optical spectrum analysis was patented [Pelayo '04] and its technical description presented [Subías '05] by some of the members of the GTF. The fundamental set-up is made up by a Tunable

Laser Source (TLS) amplified by an erbium-doped fiber amplifier (EDFA) to generate the SBS interaction in a reel of single mode fiber (SMF).

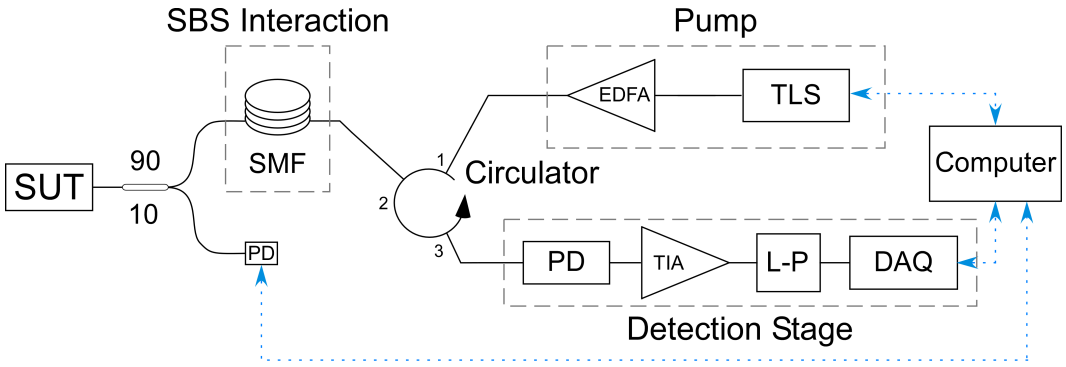

Figure I.17. Basic set-up of the for the optical spectrum analysis based on SBS.

The high power pump signal generates a Brillouin backward Stokes wave downshifted ≈11GHz, with respect to the pump central emission. An optical circulator allows optimum coupling between the signal under test (SUT), the pump and the detector in the setup. When the pump wave and the counter-propagating SUT are separated by the Doppler frequency shift, the SBS amplifies the SUT in a very narrow range, given by the Brillouin bandwidth for that pump power.

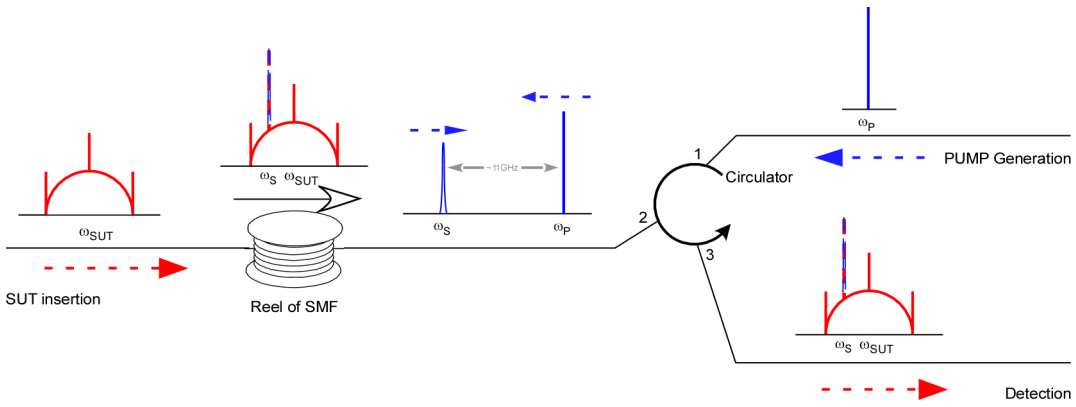

Figure I.18. Schematics of the SBS phenomena and its amplification.

The circulator also prevents the SUT source from being damaged by the pump wave. The amplified SUT is detected with a photodetector and, after transimpedance amplification and low-pass filtering to avoid contributions from heterodyning, it is sampled with a digital data acquisition card (DAQ).

At any time in which the pump wavelength is ω_P, the registered electric signal in the detector can be simplified as:

$$P_{DET} = \int P(\omega)\,d\omega \approx P_{SUT}(\omega_S)\,G_B + \int_{\Delta B} P_{SUT}(\omega)\,d\omega + P_{SP} \qquad [I.39]$$

where ω_S is the Stokes frequency for the ω_P, the integral of the SUT power correspond to the total signal power passing unamplified through the circulator, and P_{sp} is a constant term produced by spontaneous Brillouin scattering. To simplify, we have considered the interaction bandwidth of SBS infinitely narrow and other effects such as the SBS loss or fiber losses have not been taken into consideration.

The greatest contribution to the registered power at the detector is given by the product of the Brillouin gain, and the power of the signal at the Doppler-shifted pump frequency. Provided the SUT and pump power remain constant over time, we can subtract them from the detected signal to obtain a magnitude that will be proportional to the optical power of the SUT at the frequency given by the TLS wavelength and the Doppler frequency shift. By controlling the central wavelength emission of the pump and sweeping it over the SUT bandwidth, the system can recover the optical spectrum of the incoming signal. With the proper synchronism between the pump TLS and the DAQ, the system can reference the wavelength and, with a prior calibration of the gain for a constant power of the pump, the absolute optical power can be calculated.

Among other technical requirements, the system demands a high emission stability and homogenous sweep laser. Its high-nonlinearity is based on the exponential dependence of the gain, which yields to a high sensibility and enables an 80dB spurious free dynamic gain. The spectral resolution is achieved thanks to the spectral profile of the Brillouin gain, going up to 0.08pm at 1550nm. This technique presents one of the narrowest resolution compared with other techniques present in commercial devices.

In 2003, the company Aragon Photonics Labs (APL), collaborating with the GTF, presented the first BOSA prototype. Since then, the constant relationship between APL and GTF has resulted in several upgrades and enhanced performance since that first model, some of them enclosed in this thesis.

Figure I.19. Models BOSA200 and BOSA Lite

II. Direct Spectrum Analysis using Brillouin spectroscopy

The noise generated in the amplifying stages of the transmission is widely accepted as the main limiting cause for system performance [Walker '91]. The OSNR has been employed as the main monitoring parameter due to its direct relationship to the BER in the electrical domain but also because, so far, it can be obtained with a direct optical spectrum analysis. However, the deployment of advanced features in the new networks requires thorough analysis and an enhanced system for the correct OSNR measurement. High-resolution optical spectrum analysis based on SBS enables a high-detail spectrum that can reveal information that, normally, can not be resolved by other techniques. Here we revise its use in different scenarios depending on the required performance, also we present its suitability for the characterization of advanced modulation formats.

II.1. Introduction to OSNR

The most conventional OSNR measurement techniques are based on analyzing the optical spectrum of the incoming signal [Hill '93]. Relying on this principle, the optical power spectral density (PSD) is recovered at an intermediate point with a conventional Optical Spectrum Analyzer (OSA), normally based in passive filtering techniques such as gratings. The total ratio between signal and noise is calculated by measuring the noise in the spectral region between channels, and interpolating its value for the channel spectral region [ITU-T '04]. These techniques rely on the availability of spectral regions where the noise can be unambiguously detected. Nevertheless, measuring noise in tight spaced DWDM channels becomes complicated and these methods can lead to a miscalculation of the noise.

In next generation networks, add/drop, dynamic routing and grooming functionalities are consolidated. These new features present challenging scenarios for new OSNR measurement techniques. Legacy regulations and actual definitions of the monitoring parameters cannot be implemented in future networks. Interpolating the noise in the signal region might not be suitable in many scenarios and the same can be applied to those schemes where different channels present different figures of noise. Throughout this chapter, we revise the OSNR standard and its measurement with direct optical spectrum analysis. Finally, we present the advantages that high resolution optical spectrum analysis can bring to some of the drawbacks present in conventional filtering techniques and explore new set-ups for improved polarization nulling.

II.2. OSNR measurement with BOSA

Traditionally, OSNR has been measured by interpolating the Amplified Spontaneous Emission (ASE) that appears outside the channel bandwidth . This out-of-band technique assumes a flat spectrum for the noise present in the channel, and wider bandwidth for the noise than for the signal. This second assumption also implies that there exists accessible spectral regions where the noise can be measured. The most common implementation for the OSNR measurement presents a wavelength tunable filter and a detector. However, the technical requirements of these devices will be imposed by the requested performance.

In the simplest scenario, the signal passes through the tunable filter and the detector measures the power of the filtered component. The filter, by tuning its central wavelength, selects the spectral region that will be measured. The most spread devices for this purpose are the optical spectrum analyzers (OSA). These devices synchronize the tuning and the registering stage and display the recovered spectrum along the selected wavelength span.

After the spectrum is recovered, the analysis of its features provides the OSNR value based on the defined standards. According to regulation [ITU-T '04], the ASE must be measured in the center of the spectral region between the signal channels, and then interpolated. Following the regulation, the total value of the noise is defined as the optical

power density of the noise integrated over a 0.1nm bandwidth. Here, it is assumed that the noise has a constant density over the spectral region. Then, the bandwidth correction term is added in the equation [I.2] to ensure that, the measured power of the noise is independent of the filtering technique employed to recover the optical power spectral density values. On the other hand, the power of the signal is obtained by measuring the whole power of the channel and subtracting the value of the estimated noise in the same region where the channel has been measured. With these two values, the OSNR can be calculated as shown in eq. [I.2].

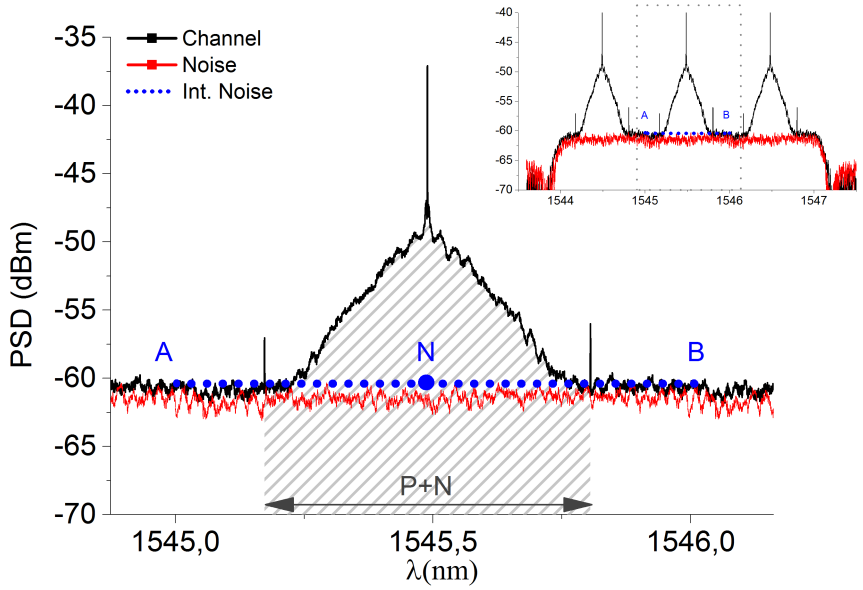

Figure II.1. OSNR measurement according to ITU-T G.694.1

The fig. II.1 corresponds to the recorded spectra for three signals with additive noise. The signals here are generated by the same 40 GHz pseudorandom bit generator (PRBS) and fed into the same Mach-Zhender modulator. By changing the bias voltage, the modulation format was set to NRZ-OOK. The noise, depicted here as the red line, was generated with a regular EDFA with no input signal, and its output was coupled with the signal. Both were filter with an optical band-pass filter and finally analyzed with the BOSA set to 10 MHz resolution. The spacing between signals, black line, is 50GHz approx. and the whole bandwidth of the noise is approximately 3nm.

Following the regulations, the points A and B are selected to measure the noise, as they are in the spectral region between channels. In both points, the optical power spectral density is measured and it is assumed that there is no contribution of the signal. With these values, the noise present in the center signal region is interpolated and integrated over the 0.1nm bandwidth that the standard states.

In the case depicted in fig. II.1, the measured value in A is -60.08dBm and in B is -59.88dBm. This gives and interpolation of N=-59.98dBm for the estimated value in N. To obtain the value of the noise in a 0.1nm bandwidth the value is assumed constant. With the 10MHz resolution, the final value of the noise is -29.01dBm.

In the next step, the power of the whole channel, shaded with gray stripe pattern, has been obtained by integrating the optical power over the whole signal bandwidth, which in this case is 80GHz as it is a NRZ modulation, giving a value of -15.01dBm. Finally, the power of the signal can be calculated by subtracting the already measured noise, interpolated in the 80GHz bandwidth of the signal, and the OSNR is determined by their quotient. For this case, the final OSNR values is 14.01dB. Here, the technical requirements demanded are low and it can be performed with standard equipment and procedure.

Nevertheless, the role of the spectral resolution has been undermined. Although the term present in the equation [I.2] removes any dependence with the spectral resolution of the filter, the system may output invalid results when the spacing between the channels is reduced. This problem arises frequently in schemes such as DWDM.

II.3. OSNR in DWDM

Typical WDM systems in the earlier 2000 were made up by 40 channels at 100GHz, the following implantation of interleavers made it possible to host 80 channels with 50GHz spacing [ITU-T '12]. Nowadays, the spacing can be stablished below the 10GHz, and it can be dynamically readapted.

In these scenarios of Dense and Ultra-Dense Wavelength Division Multiplexing (U-DWDM), the spectral resolution plays an important role. The analysis must consider the limitations imposed from the lack of resolution and the close position of the channel.

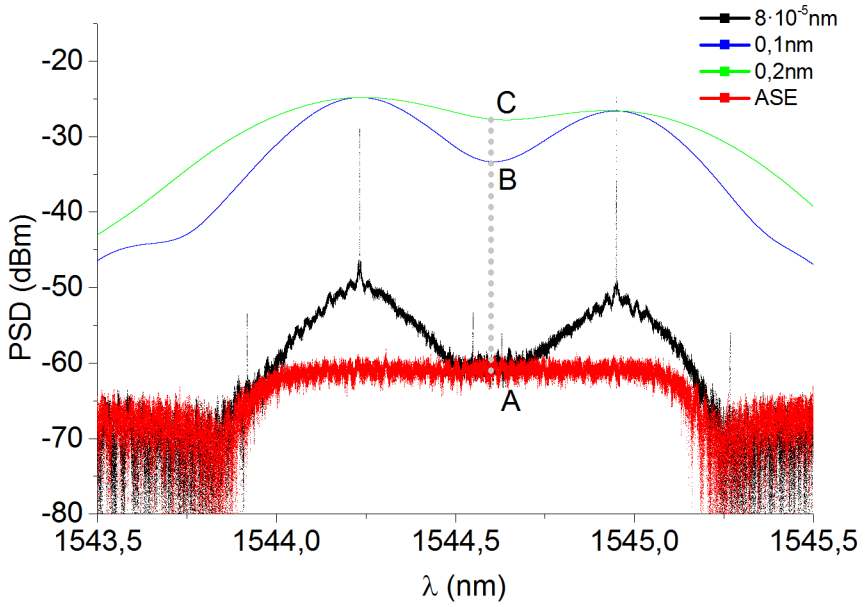

Figure II.2. OSNR measurement for DWDM

Fig. II.2 presents in black line the spectrum recorded, with a 10MHz resolution, for a system made up by two 40GHz NRZ-OOK signals and an additive noise. In this case, the space between the signals is 10GHz. The red line corresponds to the registered noise

component when the signals are not coupled. The different colored lines show the effect of reducing the resolution, the blue line and the green line present the recorded spectra for 0.1nm and 0.2nm resolution respectively.

Applying the equation [I.2] for B will provide the same result as A, due to the bandwidth correction term. The correction term of a measurement registered at 10MHz (0.08pm) and scaled to 0.1nm is -30.97dB. Which correspond to the difference between the registered point in B and C. On the other hand, the value measured on C presents contributions of the close channels and thus, it is overestimated. In this case, the difference should correspond to the readjustment between bandwidths; however, there is a difference greater than 6dB between the cases in blue and green lines, which does not correspond to the expected 3dB difference when doubling the bandwidth. This is caused by the non-negligible contribution of the spectral points corresponding to the signal that yields to an overestimation of the noise in this point.

This impairment imposes an upper limit for the resolution employed for the filtering that depends on the spacing and the rate of the involved channels. The consequence of reducing the space between channels is similar. It also ends in an overestimation when the resolution exceeds the channel spacing. In these cases, the resolution obtained by the SBS filter enables the measurement in DWDM and U-DWDM scenarios. It provides the required resolution that ensures the resolution of those spectral points were the optical power spectral density corresponds only to noise contribution.

The use of Pol-nulling techniques in DWDM may enable the use of standard optical spectral analysis techniques, as the channels may be suppressed individual, but for that they must be isolated first and its polarization analyzed. Few years ago the group presented a novel technique for the OSNR in-band measurement taking advantage of the resolution achieved by the BOSA and also the polarization drift phenomenon originated in signals affected with high-DGD [Jose Martinez '10]. In the next section we present an upgrade of the system that based on the polarization properties of the SBS eases the set-up and present new features.

II.4. Induced DGD on OSNR analysis.

Polarization nulling techniques are based on the suppression of the signal component and the measurement of the remaining optical power, either by a regular photodiode or an optical spectrum analyzer. They rely on the polarization properties of the signal and the depolarized nature of the noise. The suppression of the signal component in a channel is achieved by coupling the channel in a polarizer which orientation has been set orthogonal to the SOP of the signal. The noise, on the other hand, presents no dependence with the orientation of the polarizer and the registered component will always be half of its total power.

These techniques instead of assuming a defined shape of the noise spectra, they reach the noise level by nulling the signal component. However, when PMD is present, the system cannot recover the noise level properly, preventing a reliable measurement. Nevertheless, this impairment can help to reach an in-band measurement of the noise when high resolution is employed.

In the first chapter section I.2, it has been showed that the origin of the PMD can be described as a random DGD along the fiber. In pulsed signals, the effect of the DGD was depicted in fig.I.13 as the walk-off of the polarization vector for the different spectral components of the signal. In the proposed scenario for the OSNR measurement, the system induces a DGD over the signal affected by the noise, before coupling it into the polarizer. This yields to a controlled dispersion of the polarization vector of the spectral components of the signal.

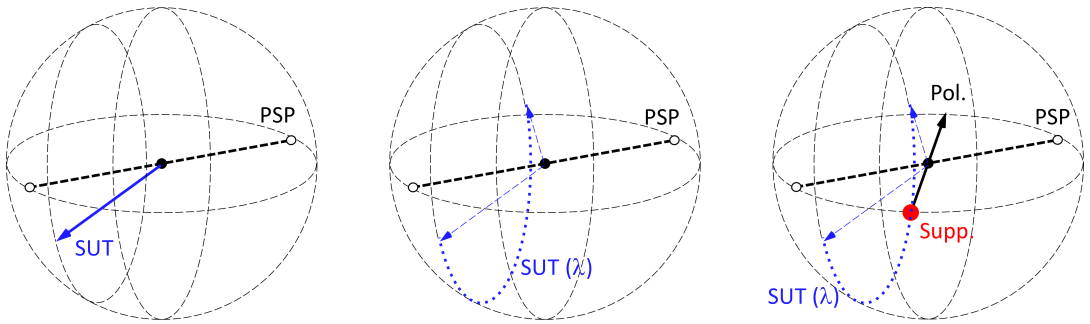

Figure II.3. Depicton of the Wavelength-dependent rotation of the polarization vector caused by the induction of a DGD on a broadband signal in the Poincare sphere.

In the fig. II.3 we can see the effect of the DGD over a wide a spectrum signal depicted over the Poincare sphere. There, we can see the rotation of the SOP of the SUT around the axis defined by the PSP, the angle will be determined by the value of the birefringence between these PSP. As the signal is not monochromatic and it presents multiple spectral components, the evolution of them will be differential, and thus the final SOP of the total signal will depend on the frequency, depicting all of them an arc as it can be seen in the central sphere in fig. II.3. By placing a polarizer, depicted as the black vector. We can suppress the particular component which SOP is orthogonal to the polarizer, here depicted as the red dot.

Due to its lack of coherence, the noise is not affected by the delay induced in the DGD system and remains depolarized. Right after the polarizer, the recovered spectrum exhibits different power levels for the different spectral components of the signal, beyond the sinc-shaped envelope characteristic of binary modulations. These recovered values depend on the projection of their SOP onto the polarization state of the polarizer. Those spectral components which polarization is orthogonal to the polarizer, are suppressed and thus, after the polarizer, the remaining detected power corresponds only to half of the underlying noise that passes through the polarizer at any orientation. If the spectral resolution is low, the filter will smooth this dependence, as it will integrate the projected value for contiguous spectral

components. This detrimental effect due to the lack of resolution is analogue to the case we have shown in fig. II.2.

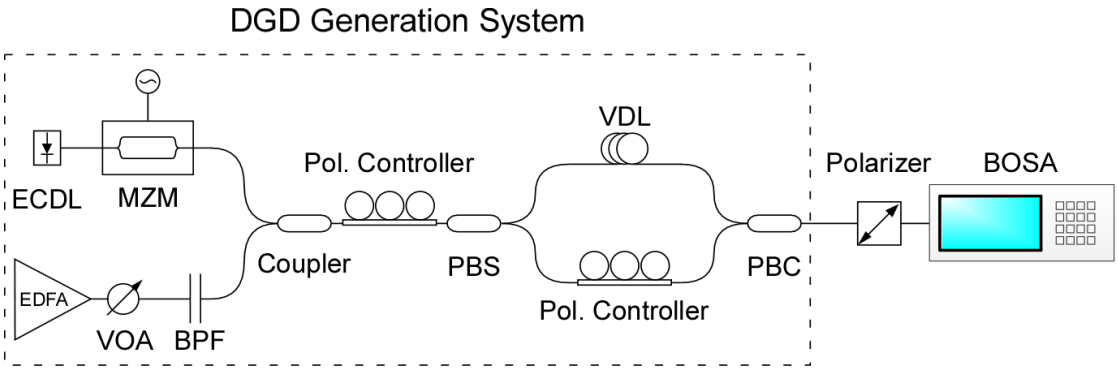

Figure II.4. Schematics for the selective in-band OSNR measurement

This impairment when resolved with a high resolution spectrum analysis allows a full characterization of in-band polarization nulled components. If the DGD set is high enough, depending on the signal bandwidth, it can be assured that there would be a complete deviance of the SOP of the spectral components of the signal. This yields to the fact that there would be components with polarization going from parallel to perpendicular prior to the polarizer. By controlling the relative orientation of the axis in which the DGD is generated and the axis of the polarizer, it can be assure that there would be spectral points which signal component will be fully suppressed and the underlying noise revealed.

The basic schematics of the induced DGD system is depicted in fig. II.4. The signal is split with a polarization beam splitter (PBS), and then one of the branches goes through an optical variable delay line (VDL). The polarization controller (PC) prior to the PBS ensures that the SUT does not match the PSP of the system at its input, which corresponds to avoid the coincidence of the blue vector and the PSP axis depicted in the fig. II.3. By placing a polarization controller in one of the branches, we can control the coupling between the two orthogonal states due to changes in the SOP of the signal in the delay lines. After that, both branches are coupled with a polarization beam combiner (PBC).

The delay line forces a different time of flight for the two brunches, which is equivalent to a controlled birefringence between the PBS and the PBC. The time of flight range of values, greater than bit-time, generates a dispersion that is enough, in 10GHz or 40GHz modulation rates, to rotate the polarization vector from parallel to orthogonal in multiples points. This rotation for angles greater than π in the Poincare sphere ensures that there are spectral components which SOP lays in the equatorial plane, in the Poincare sphere, and can be suppressed by the linear polarizer. Finally, the output of the PBC is introduced in the polarizer and the outcome spectra analyzed with the BOSA

The system requires the induction of a high DGD value, a polarization controller prior to the DGD generation system, and the implementation of a minimum search algorithm for the rotation of the polarizer prior to the analysis to search for the suppression

of the SOP of the signal. Otherwise, the system cannot guarantee the total suppression of the signal.

In the set-up depicted in fig. II.4, the polarizer acts as the polarization selective element. Its main purpose is to discriminate according to the relative angle between the SOP of the incoming signal and the polarizer. Here we propose the use of the SBS itself as the polarization selective element, keeping also its wavelength tunable selectivity. The spectral analysis is then polarization selective and there is no need for a linear polarizer. The proposed modification is depicted in fig. II.5.

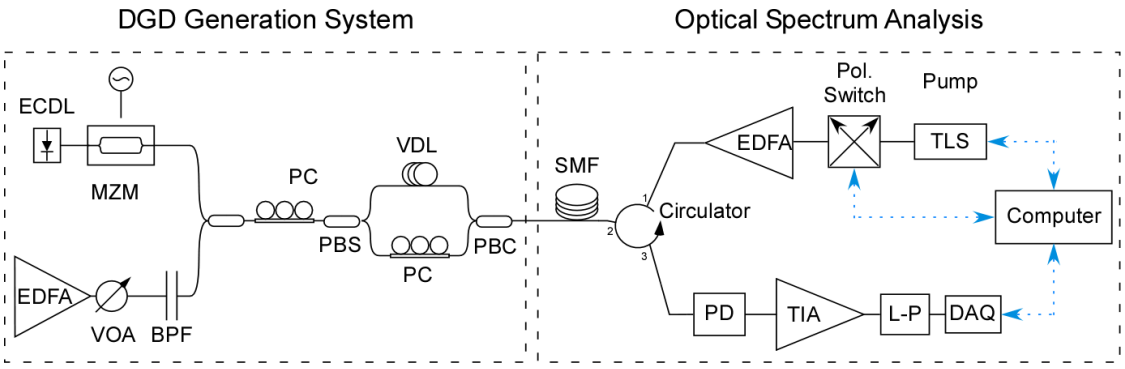

Figure II.5. Schematics for the selective in-band OSNR measurement based on SBS

In order to take advantage of the polarization properties of the SBS, here we implement a polarization switch at the output of the TLS employed as the pump. With this controller, we rotate the polarization of the pump from one state to the orthogonal. By performing a sweep in two orthogonal SOP of the pump, we can also obtain the polarization independent spectra of the incoming signal.

Fig. II.6 shows the recorded spectra for a given SOP of the pump in the black trace, and the noise measured when the signal is not coupled in the red trace. We can see that, those spectral points where the polarization is perpendicular to the pump present a minimum value that matches accurately the noise floor. The number of minimum point where the noise is revealed is directly related with the value of the DGD induced, while the amplitude would depend on the relative orientation between the PSP, in which the DGD was induced, and the SOP of the pump for the analysis. Notice that, as the suppression points do not have a wide bandwidth, it is necessary to resolve the spectra with a high-resolution technique to avoid the aforementioned effects of low resolution showed in fig. II.2 at the begging of this chapter.

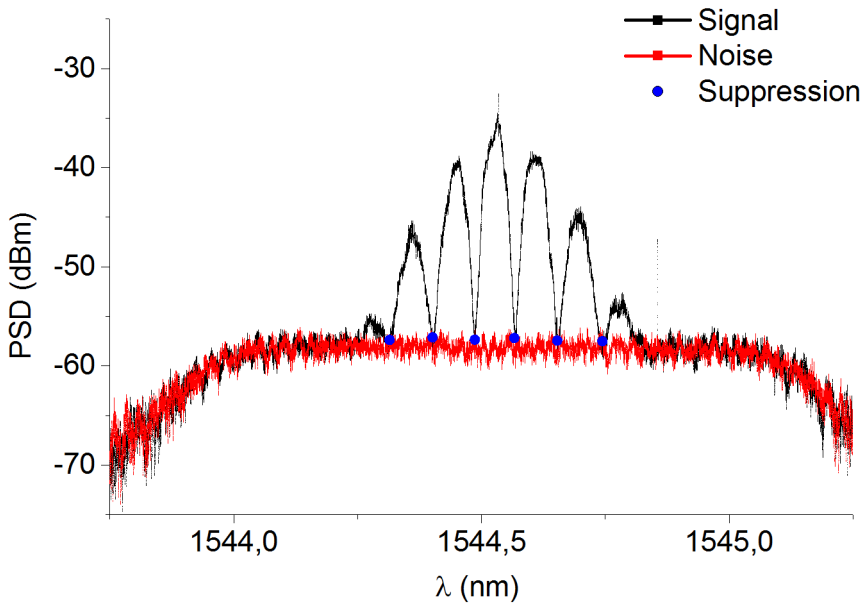

Figure II.6. OSNR In-band measurement by suppressing multiple spectral points aided by the DGD-Induced system and the SBS polarization sensitivity.

This method can reveal the in-band value of the noise, but also it can perform it continuously for the whole spectral span as the polarization sensitivity and filtering element are the same. By removing the linear polarizer, the number of passive elements and insertion losses is reduced which improves the dynamic range.

II.4.1. Limitations and potential problems

The technique presented in the previous section is based on the projection of the polarization components on the plane defined by the polarization states of the pump. As a result, there could be multiple SOP that would present the same projection over a plane, precisely any rotation over the axis perpendicular to the SOP of the pump, or the polarization sensitivity element, would be unnoticed for the system.

The most simple example is the rotation of the polarization vector from linear 45deg to linear 135deg going through the Dextrorotation or Levorotation pole of the Poincare sphere. This example can be easily set by introducing a delay between the states Horizontal and Vertical, in that case the walk-off would be maximal passing through the poles of the Poincare sphere. If this linear states match those used by the pump, the projection for all of them would be same, which produces and incorrect measurement of the impairments. (Fig. II.7.b).

This drawback can be circumvented by simply rotating the pump and performing the same measurement in any two different orthogonal states. This way, any rotation could be measured and a full measurement of the DGD achieved. In the next chapter, considering this possible upgrade, the system was modified so a full description of the polarization

properties of the signal could be performed and parameterized in the Stokes space without ambiguity.

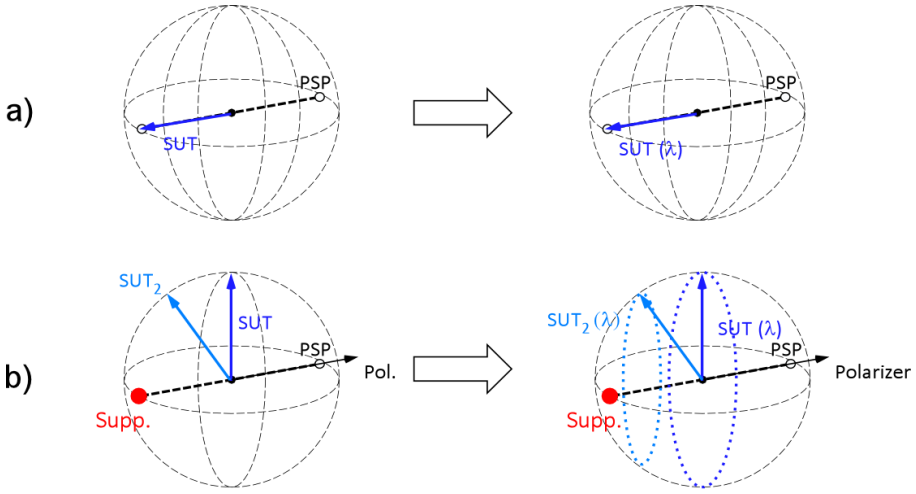

Figure II.7. Depiction of the scenarios where the induced-DGD cannot be applied. a) SOP of SUT matches the PSP defined axis; b) The polarization sensitivity element matches the axis the PSP and the projection of the SOP(λ) is constant.

The other limiting scenario has risen up recently. The new developed modulation scheme based on Pol-Mux cannot be monitored neither with the standard polarization nulling techniques nor with the DGD induced polarization nulling presented above. The use of two random and independent bit streams to modulate the same emission source in two orthogonal polarizations generates a complete randomization of the SOP of the signal. In these cases, the SOP of the signal changes at the same rate as the two streams in the two orthogonal states change. Therefore, the signal present an apparent depolarization for times greater than the bit time. As a result, polarization analysis is unfeasible, as it would require a polarizer and analysis with response times greater than the bit time, which would present no advantage in the optical domain.

II.5. OSNR in OFDM

In the new generation networks, there exists a wide range of new multicarrier modulation formats that cannot be assessed by the current standard. The regulations were designed for single carrier evaluation and, in multicarrier scenarios, either they cannot be applied or do not evaluate them correctly. Although these systems are rising in importance, there are no reference methods that could monitor the signal's health in the optical layer, to the best of our knowledge. Based on the high resolution of the Brillouin filter and modulation properties we developed a technique to measure the OSNR present in these signals in the optical layer.

II.5.1. Introduction to OFDM

The orthogonal frequency division multiplexing (OFDM) is a special case of multi carrier modulation where a single data stream is transmitted over a number of lower-rate

subcarriers (SC). Which means that, instead of having a single stream of bits modulated at a high data rate, the information is divided and transmitted in multiple lower frequency SCs in parallel, which leads to a longer bit period. In a classical parallel-data system, the total signal frequency band is divided into multiple frequency subchannels that were conveniently spaced so they would not overlap and thus avoiding interchannel interference. However, this leads to inefficient use of the available spectrum. The particularity of OFDM lies in the use of the orthogonality between the individual subcarriers. This orthogonality originates from the correlation between any two adjacent subcarriers if their frequencies are spaced by an integer multiple of the inverse of the bit time. It can be mathematically demonstrated that, when the orthogonality condition is satisfied and with the appropriate filtering, each channel can be recovered without intercarrier interference (ICI), despite a strong signal spectral overlapping

The fundamental principle of OFDM was proposed by Chang as a way to overlap multiple channel spectra within limited bandwidth without interference, taking consideration of the effects of both filter and channel characteristic [Chang '66].

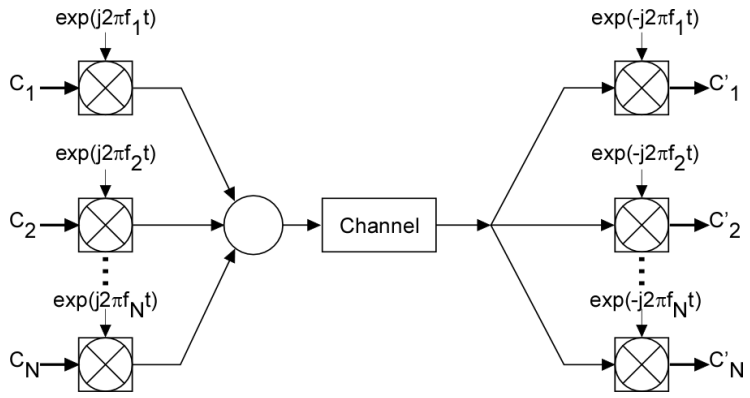

Figure II.8. Depiction of the multicarrier modulation.

The flexibility of the OFDM lays on its ability to increase the number of subcarriers and/or choose appropriate rate and format in these subcarriers. These features also ease the upgrade to higher rates and allow a spectral furnishing of the final transmission. The constant reallocation of resources proves essential for the OFDM to become a solid candidate for next generation transmission schemes. OFDM offers good spectral efficiency and efficient elimination of subchannel and symbol interference using the fast Fourier transform (FFT) for modulation and demodulation, which does not require any equalization.

In OFDM systems a signal s(t) can be represented as:

$$s(t)=\sum_{i=-\infty}^{+\infty}\sum_{k=1}^{Nsc}c_{ki}s_k\left(t-iT_s\right)$$
$$s_k\left(t\right)=\Pi\left(t\right)e^{j2\pi f_k t} \qquad \text{[II.1]}$$
$$\Pi\left(t\right)=\begin{cases}1, & \left(0<t\le T_S\right)\\ 0, & \left(t\le 0, t>T_S\right)\end{cases},$$

Where c_{ki} is the *ith* information symbol at the *kth* subcarrier, s_k is the waveform for the *kth* subcarrier, N_{sc} is the number of subcarriers, f_k is the frequency of the subcarrier, and T_s is the symbol period, Π is the pulse shaping function.

The mathematic orthogonality is achieved when the correlation between adjacent subcarriers is zero:

$$\delta_{kl}=\frac{1}{T_S}\int_0^{T_S}s_k s_l^* dt=\frac{1}{T_S}\int_0^{T_S}\exp\left(j2\pi\left(f_k-f_l\right)t\right)dt=\exp\left(j\pi\left(f_k-f_l\right)T_S\right)\frac{\sin\left(\pi\left(f_k-f_l\right)T_S\right)}{\pi\left(f_k-f_l\right)T_S} \qquad \text{[II.2]}$$

It that case the frequencies of two subcarriers must satisfy:

$$f_k-f_l=m\frac{1}{T_s} \qquad \text{[II.3]}$$

According to the definition we have described, the implementation of this modulation implies the deployment of great number of subcarriers with severe restrictions on their central frequency oscillation. However, in 1971 Weinsten and Ebert first revealed that OFDM can be implemented by using inverse discrete Fourier transform for its generation and the direct discrete Fourier transformation for its demodulation [Weinstein '71]. Based on this and with the actual FFT algorithms, the required orthogonal signals can be digitally generated precisely and in a very computationally efficient way.

Figure II.9 shows the concept of orthogonal multiplexing, where we can a see a modulation band at base frequency composed by N sub-carriers. In fig II.9(b) the system is up-converted to an intermediate frequency f_c by beating it with a radio frequency signal centered at this frequency. In fig II.9(c) the system depicts the spectra once the system is modulated in an optical carrier at optical frequency f_o.

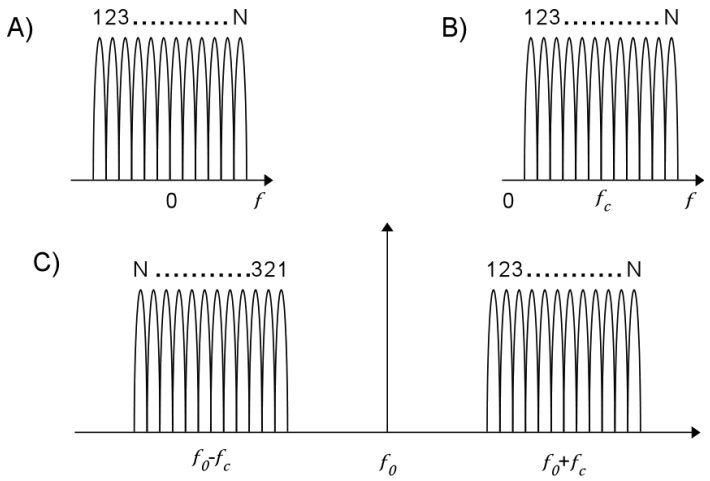

Figure II.9. Diagram of the OFDM construction.

Due to its growing popularity and deployment, the monitoring of OFDM in the optical domain has become a recent challenge. Optical spectrum analysis can be useful not only to measure the basic monitoring parameters such as OSNR, but also to characterize the modulation ultimate performance.

II.5.2. In-Band OSNR in OFDM

In the next experiment, the measurement of a single OFDM channel is addressed based on the concepts of in-band measurements. Its ability to modify its spectral shape proves useful to arrange spectral zones where the noise present in the band could be recovered.

The experimental set-up is depicted in fig. II.10.The signal is synthetized off-line aided by a DSP and Matlab software. A stream of 2^{15} bits running at 2.5 Gb/s is mapped into 4-QAM symbols and modulated using an N-points inverse fast Fourier transform (IFFT).

In order to ensure a correct data demodulation after photo-detection, a guard interval with the same bandwidth of 2.5 GHz as the electrical OFDM signal is generated. By doing so, at the receiver the mixing products between the signal and the optical carrier can be filtered out. The digital OFDM signal is then loaded onto an arbitrary waveform generator (AWG), operating at 12 GSa/s. The signal at the output of the AWG then drives a Mach-Zehnder modulator (MZM) biased at the quadrature point ($0.5V_{\pi}$), which modulates a sampled grating distributed Bragg reflector (SG-DBR) tunable laser source (TLS) running at λ_0=1550.92 nm with measured linewidth of 48 MHz.

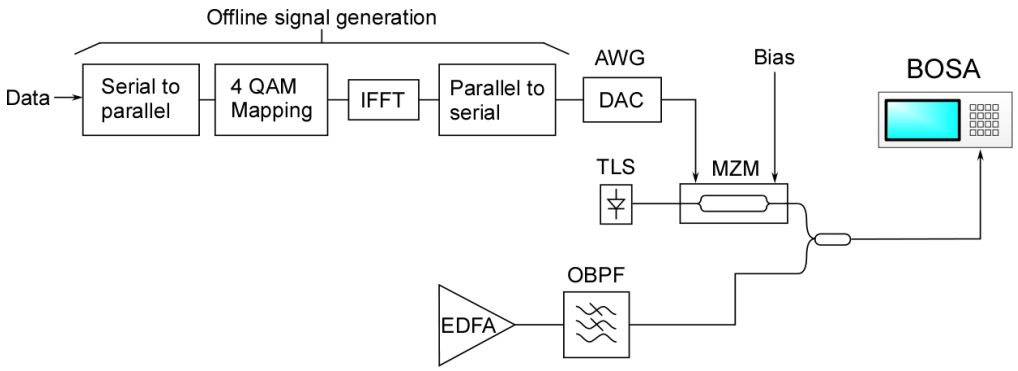

Figure II.10. Experimental set-up for monitoring OFDM

The optical spectrum analysis is performed with a standard BOSA. In order to test the set-up, the spectra of the optical OFDM (O-OFDM)signal are registered for different number of subcarriers (N).

Fig. II.11 shows the obtained optical spectrum for N=8, averaged over 54 measurements. Clearly, one can see the characteristic spectral shape of a double side band optical OFDM signal that has been seen previously in the electrical domain since its application in radio. The optically intensity modulated OFDM (IM O-OFDM) signal is symmetric with respect to the optical carrier and presents a constant flat power spectral density over the 2.5 GHz OFDM signal band and a guard interval with the same bandwidth. The OFDM signal exhibits a small distortion corresponding to the subcarrier ($\lambda_0 \pm 3.75$ GHz). It arises from the implementation of the hermitian symmetry for which the zero and Nyquist frequencies have been set to zero.

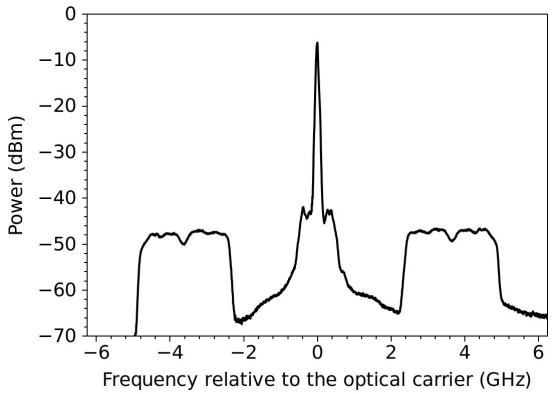

Figure II.11. Recovered optical spectra for and OFDM with N=8 averaged over 54 measurements

In the next scenario, the number of subcarriers was increased to N=16 and all the mapped symbols of the input sequence were set to 1, in order to analyze the spectral shape of the subcarriers. As it happens in single carrier modulations, in this static situations the effective linewidth of the carriers is depicted in the spectra. Fig II.12 shows the recorded spectrum for just one sweep across the modulation. Here, we can see that the spectral shape of the 16 subcarriers is revealed when no signal is introduced in them. As we can identify the subcarriers, we could also be able to observe and quantify impairments or its absence by

analyzing the spectral shape of the modulation in the same way it is performed for single carrier modulations.

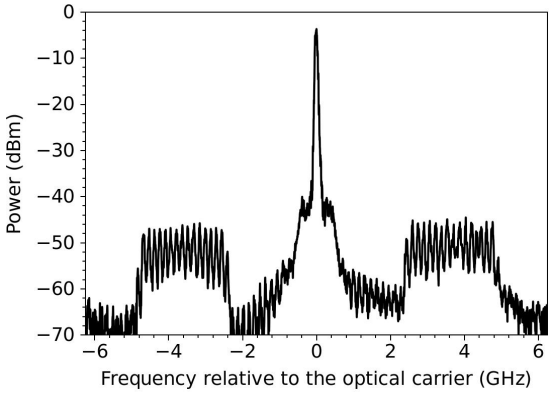

Figure II.12. Recovered optical spectra for and OFDM with N=16 in a single sweep

Now we couple the exit of an Erbium Doped Fiber Amplifier (EDFA) with a 2x1 coupler as seen in fig. II.10. This EDFA without input signal simulates the cases of an additive white noise in the C-band region. The noise generated by the EDFA was previously filtered with a 100 GHz wide optical band-pass filter (OBPF) in order to ensure working in an optimal power range for measurement, i.e. no saturation in the detectors.

The first approach for measuring the OSNR in these cases is based on prior definition of the OSNR in single carrier modulation and stated in the regulations [ITU-T '04]. Instead of measuring in the gaps between channels and extrapolate, here we search for different regions where the noise can be isolated.

The total power, P_T, of any region with signal power P_S and with an integrated ASE noise power P_N can be written as $P_T=P_S+P_N$. The ASE level measurement can be performed at selected frequency ranges, either within the guard interval (λ_0±2.5 GHz) or in those corresponding to OFDM subcarriers selectively suppressed.

The power measured in those regions is extrapolated to the whole band assuming a flat noise spectrum. The total noise power (P_N) inside the bandwidth used for evaluating the OSNR can be directly measured integrating the power in the selected region. After that, the original signal level (P_S) is found by subtracting the estimated noise power from the measured signal power over the same bandwidth (P_T), and the OSNR=P_S/P_N can be calculated.

In the first case, we focus on the proposed O-OFDM signal with N=64. In fig. II.13(a), it can be observed that the received optical power within the guard band corresponds only to noise. However, when approaching to the optical carrier, the spectral characteristics of the laser limit the band within the noise measurement should take place, leading to erroneous measurements. This compels the measuring points to be within the ranges λ_0±1 GHz and λ_0±2 GHz. Which, as we have seen in the previous section, sets a higher technical requirement for the measurement.

The power of the noise (P_N) is estimated to be -30.72 dBm for a 12.5 GHz (0.1 nm) reference bandwidth. This value is only 0.49 dB away from the -31.21 dBm obtained when measuring the noise without the O-OFDM signal, shown in red line in fig. II.13(a). As the total power (P_T) was -7.20 dBm in the mentioned bandwidth, the signal power (P_S) is estimated to be -7.22 dBm, resulting in an OSNR (P_S/P_N) of 23.50 dB. The noise power here has been measured in the guard band. Although this band could be considered part of the modulation, as it has been deliberately set in the transmission end for the sake of demodulation, it would be more desirable to be able to reach the underlying noise power inside the modulation; so it could be considered an in-band measurement.

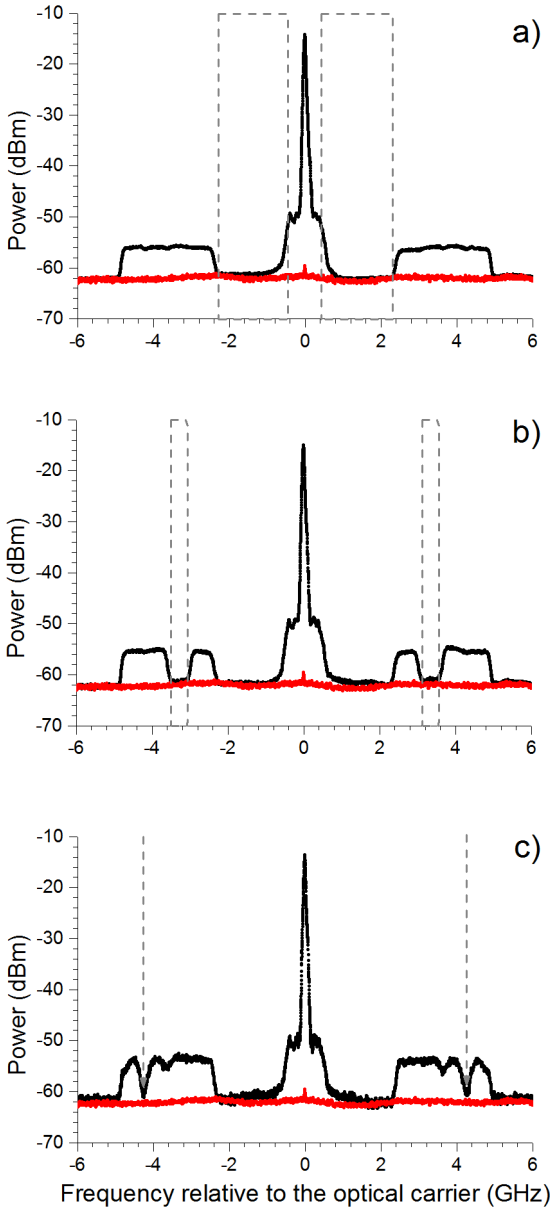

Figure II.13. Measured spectra for OSNR calculus.

Next, in order to demonstrate a noise measurement inside the OFDM band, an OFDM signal was generated with N=64 carriers, occupying the same bandwidth as the

previous transmitted signals. In this case, we suppressed 16 consecutive subcarriers in order to generate a spectral region with no signal power on it. This is shown in fig. II.13(b). Following the steps described above, but now taking into account only the bands between λ_0±3.05 GHz and λ_0±3.45 GHz for measurements, the noise could be estimated to be -30.18 dBm, 0.04 dB away from the reference noise power. Total measured power was -7.96 dBm in the whole 12.5 GHz signal bandwidth and the signal power was estimated to be -7.98 dBm, meaning that the estimated OSNR is 22.20 dB.

Finally, we analyzed the case of ASE estimation when suppressing a single OFDM subcarrier. Theoretical limit based on the SBS gives 40 dB extinction for 60 MHz spacing, however several other factors, such as laser phase noise, jitter, etc.., reduce the sensitivity. In the setup of fig. II.10 the limiting factor was the wide linewidth of the SG-DBR tunable laser. So, for ensuring the ASE detection, this time an O-OFDM with N=8 subcarriers was considered, and one of the subcarriers was suppressed. The resulting spectrum is shown in fig. II.13(c). The power density corresponding to the suppressed subcarrier (λ_0±4.25 GHz) revealed -29.36 dBm of ASE when measured in 0.1 nm bandwidth, 1.85 dB away from the previously measured noise power. The whole signal power was found to be -7.23 dBm inside the same bandwidth, giving an estimation of the signal power of -7.26 dBm. Thus, the OSNR is estimated to be 22.09 dB.

Therefore, in case of O-OFDM-based bandwidth variable transponders, in which carriers can be adaptively suppressed, the frequency range without signal can be used for noise measurements. When the O-OFDM transponders are based on intensity-modulation direct-detection (IM/DD), the guard interval, required for correct signal recovery at the receiver, furnishes a spectrum region in which in-band ASE noise measurements can be performed, leading then to a proper in-band measurement in the desired regions. By selectively performing this operation, the measurement could be synchronized and the whole noise floor mapped. These measurements are similar to the IEC recommendation for measuring OSNR in DWDM with single carrier modulations, and thus require caution when analyzed.

The results prove that in the optical spectra we can sense some basic impairments such as the lack of subcarriers, also identify its position in the band and measure their power levels. Bearing in mind these results, it may be possible to go further and perform a full characterization of each individual carrier separately from the whole band. In this way, this identification may result in a re-definition of monitoring parameters in the subcarrier domain. An individual parameterization of each sub-carrier could be useful to identify the most robust subcarriers. Due to the high flexibility of this modulation, these parameters could be employed to allocate resources by sorting the subcarriers according to their robustness and performance.

II.5.3. SC-OSNR in OFDM

In this section, the main goal is to obtain an OSNR measurement at the subcarrier level and correlate it with reference parameters in the electrical domain. Thus, the impact of the optical noise on each O-OFDM subcarrier could be assessed by a simple optical spectrum analysis. However, some processing of the acquired optical spectrum samples must be performed in order to relate these measurements with the signals recovered at the receiver.

The concept underlying the OSNR measurement is the parameterization of the distortion present in the signal due to noise by analyzing its optical spectra. In the prior cases or in the single carrier modulation, the concept is easily carried out by considering the whole spectra of the signal lies in the region close to the optical carrier, occupying the region delimited by the transmission rate. When migrating this concept to sub-carrier in OFDM, the same criteria cannot be applied, because due to construction and symmetry, the information extracted in one sub-carrier does not lay in one single spectral region. As a result of the multiple symmetries present, the information transmitted in one subcarrier is reflected in the optical spectra in different regions. And this implies also that the impairment present in all of these multiple spectral regions affect the recovered information.

For the case of real-valued fast Fourier transform (FFT), the symmetry is forced at the DSP of the transmitter. There, only half of the subcarriers support data, the other half carry the complex-conjugate of this data. When the fast Hartley transform (FHT) is used for OFDM modulation, the spectral symmetry is obtained with no additional processing. [Shieh '06]

According to the principle of the OSNR definition for single carrier modulations, here we define the sub-carrier OSNR as the ratio between the signal optical power spectral density (OPSD) and the noise spectral density (NSD) in the spectral regions of the sub-carrier:

$$OSNR_{SC} = \int_{f_{sc}-BW}^{f_{sc}+BW} \frac{OPSD}{NSD} df \qquad [II.4]$$

Where the optical power spectral density for the signal and the noise takes into account the symmetries imposed by the modulation in the DSP and in the modulation in the optical domain.

In order to correlate this defined value, some assumptions about the noise should be considered. When the signal E(t) is degraded by some optical noise (e.g. due to optical amplification), this is translated to a certain SNR degradation after photodetection. According to the noise beating theory [Agrawal '12] , the beating between signal and noise can be considered dominant for high OSNR, which can be approximated as Gaussian noise. Thus, the power spectrum of N(t) is approximately flat and with density:

$$G_N(f) = \frac{2R^2 P_s^2}{OSNR \cdot B_O} \quad \text{[II.5]}$$

Where B_O is the optical reference bandwidth for measuring the OSNR, OSNR=Ps/N_O is the global optical OSNR, and N_O the power of optical noise within B_O.

For the case of the subcarriers, one can describe the power of each subcarrier having in account the signal is generated with the Mach-Zhender modulator and the optical power at its output can be described as:

$$P_{SC} = \frac{1}{2}\frac{\pi V_{DAC}}{V_\pi \sqrt{N_C}} P_S \quad \text{[II.6]}$$

Thus, the OSNR per sub carrier can be described as:

$$OSNR_{SC} = \frac{P_{SC}}{N_O} = \frac{\pi V_{DAC}}{V_\pi \sqrt{N_c}} OSNR \quad \text{[II.7]}$$

According to [Fabrega '13] the electrical SNR on the other hand can be described as:

$$SNR_E = \frac{P_X}{\sigma_N^2} = \frac{\pi^2 V_{DAC}^2 B_O}{V_\pi^2 N_C B_e} SNR_O \quad \text{[II.8]}$$

Having in account [II.7] and [II.8] the electrical signal to noise ratio and the optical signal to noise ratio can be related as:

$$\frac{OSNR_{SC}}{SNR_e} = \frac{1}{2}\frac{V_\pi \sqrt{N_C}}{\pi V_{DAC}}\frac{B_e}{B_O} \quad \text{[II.9]}$$

In other words, as SNR_e is proportional to the $OSNR_{SC}$, one can estimate the performance of the OFDM modulation by a simple inspection of $OSNR_{SC}$, and even extrapolate a limit for the probability of error of the symbols. Please, note that this model may be limited to work under some assumptions, e.g. the Gaussian distribution of the electrical noise and the high OSNR condition.

In order to perform a first test of the OSNR monitoring at subcarrier level, the experimental set-up described in fig. II.14 is used for a back-to-back configuration. It is conceived to characterize the correlation between the different levels of OSNR in the optical domain, and the performance analysis parameters in the electrical domain. The DSP and electrical up/down-conversion at the transmitter/receiver are performed off-line, following the steps detailed in fig. II.14 .At the transmitter, random generated data are mapped into the corresponding constellation (BPSK) and modulated by an FHT, with 64 subcarriers. The system is intended for occupying a 12.5GHz channel and, consequently, the total bandwidth of the generated optical spectrum is set to 11GHz. A small guard band of 500MHz around

the optical carrier f_o=193.865THz (1550.92nm) is set for avoiding undesired effects from the laser emission profile.

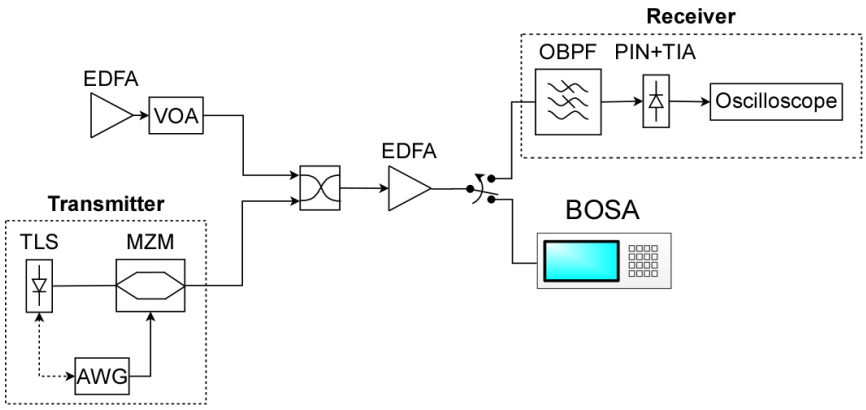

Figure II.14. Schematics of the Optical Spectra measurement and the electronic demodulation

The considered electrical bandwidth occupancy for the useful OFDM signal (51 subcarriers) is 5GHz. The bit rate is 5Gb/s, as a BPSK modulation format is used. The obtained real-valued OFDM symbols are then serialized. The digital OFDM signal is clipped and upconverted to an intermediate frequency (f_c=3GHz) by mixing with a digital oscillator. The resulting signal is converted to the analog domain by the AWG. This analog signal is injected into the MZM biased at the quadrature point and excited by a tunable laser source (TLS). As done in the prior section cases, an additive white noise generated by an Erbium Doped Fiber Amplifier (EDFA), followed by a variable optical attenuator (VOA), is introduced in the system by means of a coupler. The VOA enables the noise level control of the ASE that is coupled into the system.

At the receiver, the incoming signal passes through an optical bandpass filter (OBPF) of 0.1nm, for filtering out the optical noise. Next, the optical signal is detected by a module composed by a PIN diode and a transimpedance amplifier (PIN+TIA). The detected current is digitized by a real-time oscilloscope (OSC) running at 50GSa/s. The OFDM baseband signal is then recovered after downconverting and low pass filtering in the digital domain. The recovered signal is off-line demodulated, equalized and demapped. Every 2048 OFDM frames, 8 training symbols are inserted for synchronization and equalization.

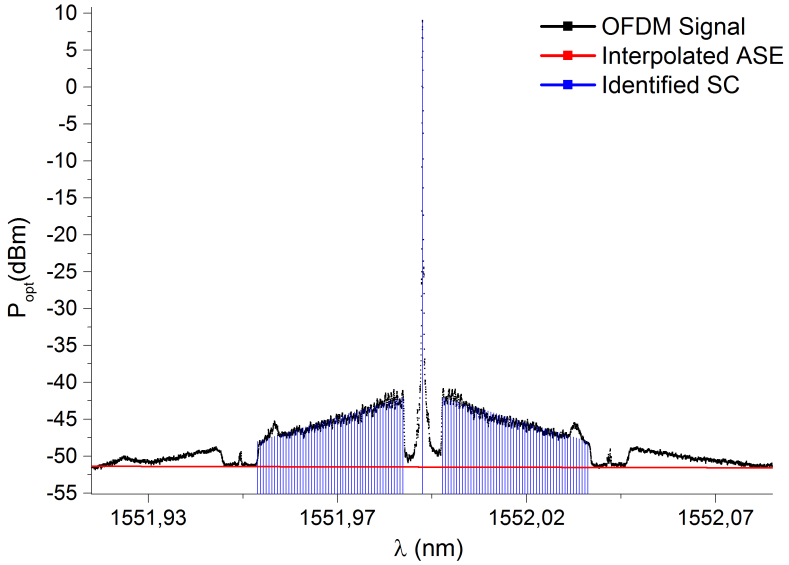

Figure II.15. Detailed optical spectra of an OFDM signal identifying the subcarriers..

In fig. II.15 we can see the recorded spectrum of the OFDM. There, we can see an individual identification of the sub-carriers. This identification here was performed with prior knowledge of the number of carriers; however this information was not necessary, as by its shape it can be calculated. In order to track slight and sudden frequency drifts of the system, a convolution of the measured spectra with prior and posterior measurements is performed continuously to avoid undesired misalignments. This technique ensures proper alignment for averaging successive measurements. In figure II.16 we can see a detailed zoom of one of the sidebands of the OFDM signal.

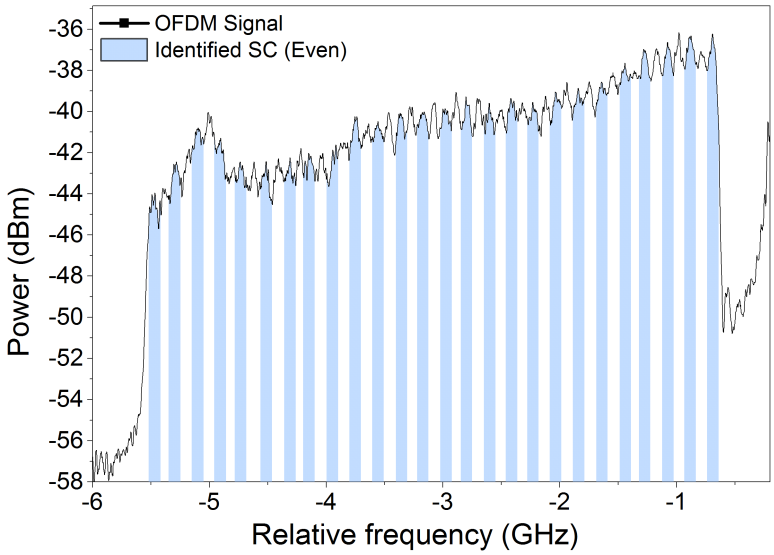

Figure II.16. Subcarrier identification.

In order to assess the impact of the optical signal degradation at a subcarrier level, the optical spectrum of fig II.16 has to be mapped with the corresponding digital subcarriers. The procedure to apply is the following

1. An optical signal to noise ratio per subcarrier (SC-OSNR) is defined in the spectral interval occupied by each subcarrier. In contrast with the total OSNR defined for 0.1nm and accounting for an average performance of the whole system, this value allows specific characterization and performance degradation monitoring for each subcarrier.
2. The SC-OSNR contributions at the two sides of the optical carrier are averaged between them in order to take into account the symmetry due to the optical modulation. At this point, we obtain an SC-OSNR spectral distribution like fig. II.1.
3. In order to take into account the inherent Hermitian symmetry of the FHT, a further average of the SC-OSNR is performed between both sides of each OFDM band.

Once the figure of merit is defined, we test its usefulness for different scenarios. First, we set the system with different values of the global OSNR, defined for an ASE measured within a bandwidth of 0.1nm, ranging from 18dB up to 32dB. These values are further referred to as total OSNR, in order to distinguish them from SC-OSNR. The fig II.17 shows the different SC-OSNR measured for each SC individually for different values of the total OSNR.

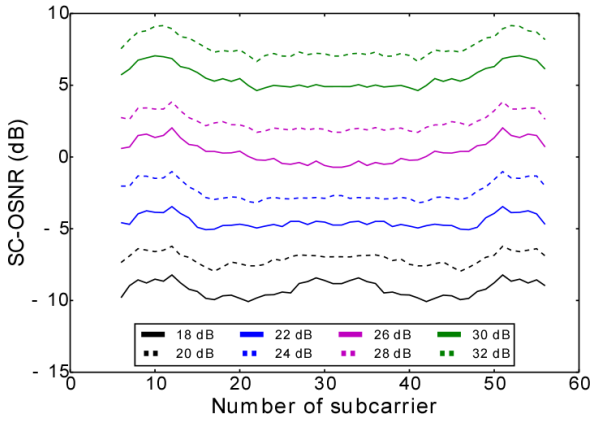

Figure II.17. Different SC-OSNR level for the different subcarriers at different global OSNR values.

In order to validate this measurement we need to correlate the measured SC-OSNR with the distortion values in the detection end. To do so, the reference measurement we employ are based on electrical performance after the demodulation of the signal. As these are the fundamental measurements for the signal's health, all the correlations are done using them as the reference value.

Employing the SC-OSNR calculated from the high-resolution OSA spectrum and the electrical SNR calculated at the receiver, a direct relationship is found between them. This is shown in fig. II.18 where the SC-OSNR is plotted as a function of the electrical SNR before equalization (a) and after equalization (b). As expected, the electrical SNR before equalization is highly correlated with the SC-OSNR. In fact, their dependency is almost linear in dB, meaning that increasing one dB of electrical SNR is directly translated to a 1dB

increase of SC-OSNR. In addition, for high values of OSNR, the theoretical model based on eq. [II.9] acts as a lower limit, following the tendency.

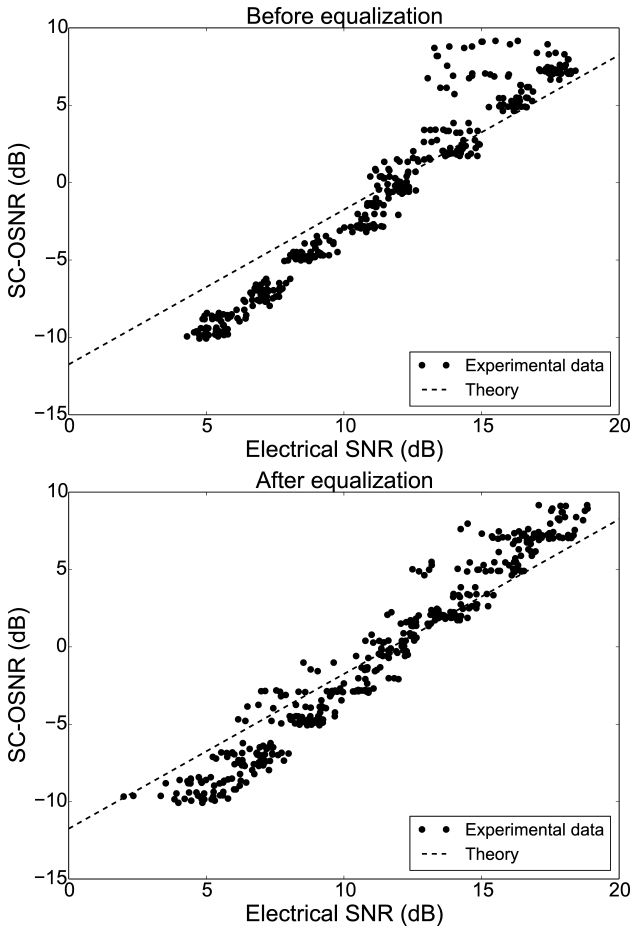

Figure II.18. SC-OSNR and Eelectrical SNR correlation

Nevertheless, for high values of electrical SNR, there is a high dispersion of points. For high total OSNR values, the electrical SNR of the subcarriers at the edges is limited to 13dB. In order to overcome this effect, the electrical SNR is calculated after equalization, as shown in fig. II.18 (b). For this case, the points corresponding to higher electrical SNR have lower dispersion.

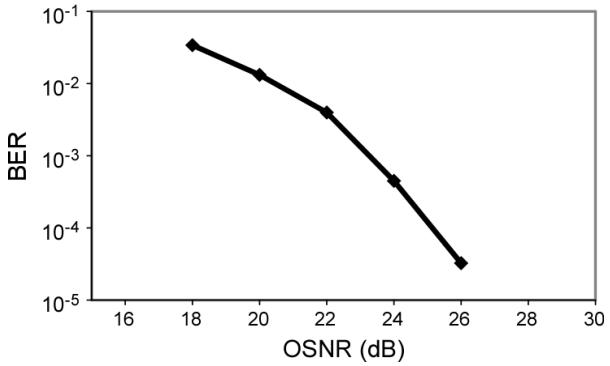

Figure II.19. Total BER as function of the total OSNR.

Finally, BER measurements are obtained by statistical bit error counting to obtain up to 10^3 errors. Fig. II.19 shows the total BER as function of the total OSNR. There, it can be observed that 10^{-3} BER is attained at 23.7 dB of OSNR. Fig. II.20 shows the BER distribution over the OFDM active subcarriers at different values of the total OSNR, for a single acquisition of 2^{15} bits. It can be seen a clear correlation between fig. II.20 and fig. II.17, showing the same trend for the SC-OSNR and the BER in the detection. In addition, a direct relationship is found between SC-OSNR measured with BOSA and BER for this acquisition. As expected, the BER is correlated with the SC-OSNR, in a similar way as the total OSNR, see fig II.19 and fig. II.21 , decreasing one order of magnitude per 5dB increase of SC-OSNR. Also, the BER calculated from eq. [II.9], dashed line, acts as an upper limit, as it is the limit performance when OSNR is high enough.

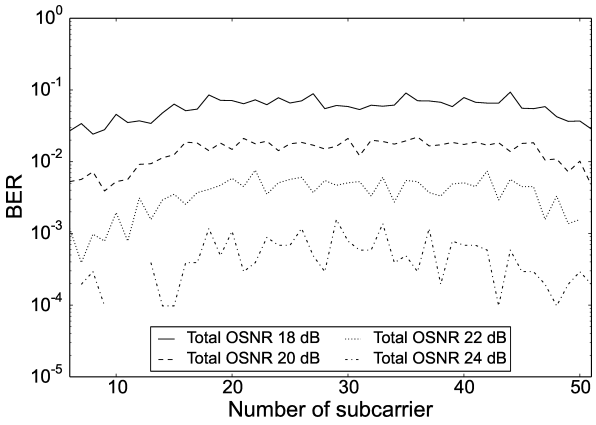

Figure II.20. BER measurement for each OFDM subcarrier.

The resulting averaged SC-OSNR is a figure of merit, which takes into account all the symmetries of the double sideband IM/DD spectra and thus, it can be directly related to the figures obtained in the digital domain, after OFDM demodulation. Additionally, this methodology can be easily adapted to other OFDM techniques. For example, when data is mapped to a complex-valued FFT combined with I/Q modulation and coherent detection, a more straightforward mapping between optical spectral components and data symbols is present.

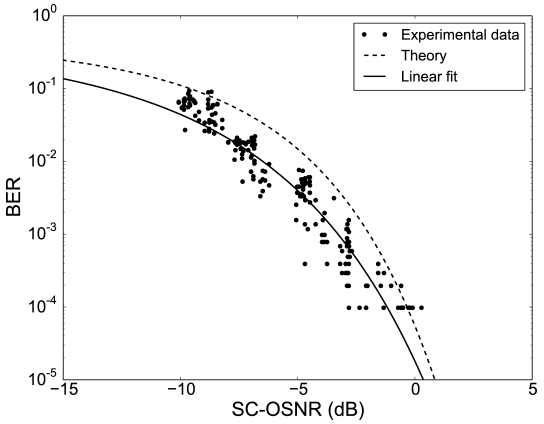

Figure II.21. BER and SC-OSNR correlation.

This individual characterization of the noise present in the different subcarriers could be useful to a sensible design of the OFDM transmission scheme. Depending on the SC-OSNR of each subcarrier, the system could adapt the modulation scheme for those subcarrier that have been more affected by the noise. The final goal is to select their modulation format according to its robustness to the noise.

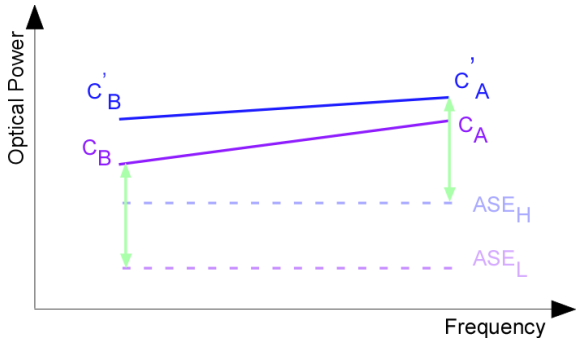

Figure II.22. Schematics for the different Sub carrier performance at different global OSNR values.

For different noise levels, the different subcarriers can be affected in different ways. As the OFDM allows a high flexibility, sub-carrier characterization could also widen the window of operability when needed.

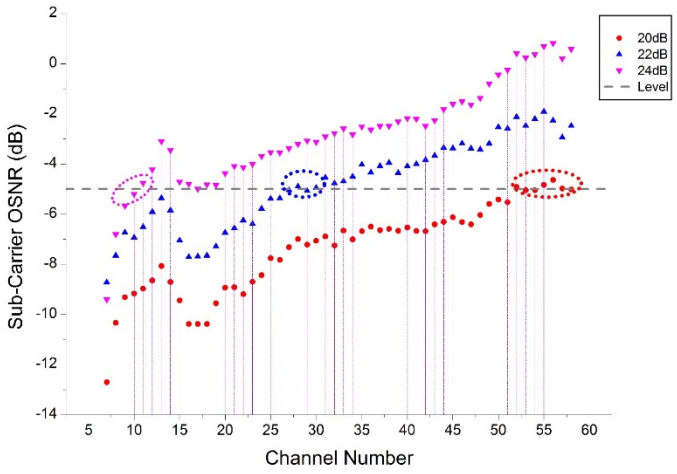

Figure II.23. Measurement of the different SC-OSNR at different global OSNR that allows and individual performance assessment.

In fig. II.22 it can be clearly seen the same performance for different sub-carriers in different global OSNR levels. The purpose of this section is to consider the sub-carrier optical monitoring as a method for reaching up to higher levels of quality and thus exploit the optical domain for in-band measurements.

II.6. Conclusions

In this chapter, we have recalled the drawbacks present in the OSNR optical for different scenarios. It has been also shown the potential of high-resolution to overcome some

of these limitations. DWDM scenarios have been faced and we have shown the limitations imposed to the resolution by the desired performance.

We have demonstrated the potential that high-resolution spectral analysis can bring to multicarrier modulation formats in order to monitor optical performance parameters such as OSNR. In this framework we have proposed a methodology to estimate sub-carrier OSNR and we have validated the direct correlation between BER performance of individual sub-carriers and measured sub-carrier OSNR.

Live monitoring of these quality parameters can be performed in the nodes of the optical networks with no need for demodulating data. Thus, it becomes a key point towards better management of OFDM-based systems in future flexible and elastic optical networks. Additionally, the methodology developed can be easily adapted to be used when employing other OFDM techniques, such as coherent optical OFDM.

We have also proposed a novel scheme to enhance polarization nulling techniques. Based on the phenomena produced in a signal due to DGD, we can induce a selective suppression of the signal component and thus reveal in-band values of the underlying noise. To that end, we take advantage of the vector properties of the Brillouin filter. Using its polarization sensitivity, we substitute the polarizer present in these nulling techniques for the polarization dependence of the Brillouin gain. The system achieves a complete characterization of the noise for the whole C+L band without needing prior filtering of the channels or and without losing in-sight resolution .

III. Brillouin Spectrally-Resolved Polarimetry

In this chapter, the polarization sensitivity of the SBS is presented as the core of a spectrally resolved polarimeter. This feature, exploited as a polarization discrimination element, together with its intrinsic gain profile, is studied in this chapter. Starting from the conceptual diagram of the design for a spectrally-resolved polarimeter, here it is summarized the main steps going from the set-up schematics to the software interface development.

III.1. System Design

The full recovery of the polarization information of the signal requires a complete characterization of the SOP across its bandwidth. The fundamental core of the measurement must contain a polarization sensitive element and another sub-system that discriminates according to the wavelength. The principle of measurement can be simplified as depicted in figure III.1.

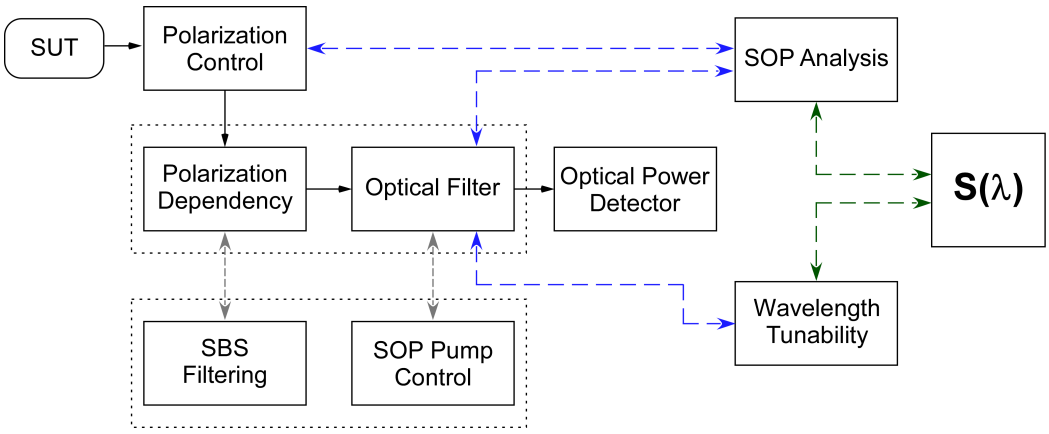

Figure III.1. Conceptual diagram for the polarimeter design

As we have shown in previous chapters, the SBS polarization dependence can be used to recover polarization deviation over the projection of the SUT SOP and the pump SOP. In those cases, the system was limited to measure misalignment with the SOP with no further characterization of the polarization properties of the signal. In order to obtain a full recovery of the Stokes parameter, additional steps are required. At this point two options were faced, either performing three controlled rotations of the signal, with their respective projection over one fixed stated of the pump; or performing three rotations of the pump SOP and a projection of the income signal over the pump states.

The first option implies a manipulation and, in most of the cases, a prior knowledge of the SOP of the incoming signal. The main goal is the design of an operative monitoring method for polarization impairments; hence, the rotation of the signal was discarded. The second option requires only a controlled rotation of the pump. There exists several commercial options to achieve a defined rotation of an incoming SOP with great performance.

In the proposed design, the system rotates the SOP of the pump and registers the six projected spectra. These data are used to calculate the three stokes parameters. Specifically, as stated in the chapter 1, all the polarization states of the pump must be orthogonal in the Stokes space.

Attending to the conceptual schematic depicted in figure III.1, the set-up was designed as it can be seen in figure III.2.

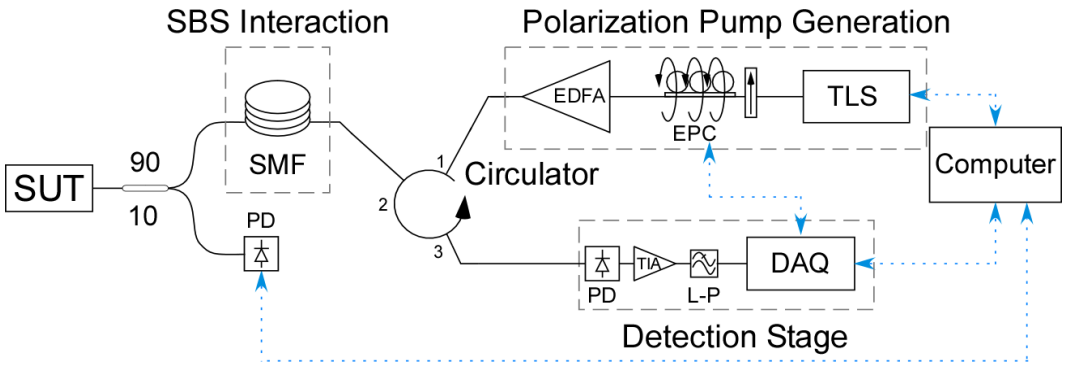

Figure III.2. Set-up for the spectrally resolved polarimeter based on polarization dependence of the SBS

The use of six different polarization states for the pump requires the characterization of polarization dependent losses (PDL) for the different elements, which imposes a technical requirement for all the involved elements. Any PDL or polarization dependent gain (PDG) that would induce a differential weight in the sweeps, would also induce an overestimation of any of the Stokes parameters. This would lead to an erroneous final measurement of the polarization properties.

The electronic polarization controller (EPC) ensures the generation of the six principal polarization states. However, the pump goes through several optical elements before reaching the spool of fiber where the non-linear process takes place. The evolution of the polarization across this path is unstable and thus, its final state cannot be predicted. The randomness of this mentioned evolution matrix for the polarization, makes the effort of its characterization futile. However, its evolution can be approximated to polarization state independent, and thus the relative orientation between states, orthogonal in Stokes space, can be considered constant. This assertion is true for the set-up presented above, i.e. if we consider single mode fiber elements and no polarization maintaining elements.

This final statement leads to the conclusion that, all the measurements can be considered rotated over an absolute principal axis. Henceforth, the relative position and angles are constant while the absolute position is not. Regarding all the formula deduced in the theory, all the mentioned parameters employed in the characterization, only depend on the relative orientation between the polarization states of the different spectral component, not in their absolute value.

III.1.1. Measurement method

The recovery of the SOP of the signal requires the measurement of six spectra for six different SOP of the pump. The non-ideality of the devices present in the filtering block leads to an intrinsic polarization dependence while acquiring the spectra. The most sensitive element is the EDFA for the pump. The PDG of the system must be compensated in order to achieve the required performance.

In order to isolate the effect of the PDG, the spontaneous emission of the Brillouin scattering is measured for all the states of the pump. For this purpose, an optical switch is placed right before the signal, at the input of the device, to block the incoming signal and thus, recording the solely spontaneous emission of the Brillouin Scattering, rather than the stimulated scattering when the signal is present.

The whole synchronization of the system is controlled by a motherboard performing the next steps:

- Establish one of the SOP for the pump by controlling the EPC.
- Activate the pump laser emission that is directly amplified by the EDFA. The high intensity wave is coupled in the spool of fiber.
- Block the signal under test and register the spontaneous Brillouin emission for the polarization by performing a wavelength sweep with no stimulus present.
- Measure the incoming signal level by deactivate the pump laser emission, unblock the signal and register just its power level. (as seen in fig. I.17).
- Activate the pump, allow the SBS amplification, perform the wavelength sweep of the pump and simultaneously sample the electronic signal of the photodetector.
- Subtract the contribution of the incoming signal and the spontaneous emission for the whole wavelength range.
- Perform the above steps for the orthogonal polarization and, by its subtraction resolve one of the Stokes parameters across the swept wavelengths.
- Iterate the process twice for the next two pairs of orthogonal states.
- Finally, represent the spectrally resolved state of polarization.

The parameters are calculated synchronously with ad-hoc algorithm implemented in the motherboard that controls all the involved devices. Once the calculations are performed, the processed data can be analyzed and interpreted.

The next step for checking the validity of the method was to perform a calibration. For this purpose, several calibration experiments were designed to evaluate its technical performance and its weaknesses

III.1.2. Calibration routines

In the first scenario, a linearly polarized ECDL was coupled into the system after it went through a high birefringence fiber. The recovered stokes parameter for 20 consecutive measurements is depicted in figure III.3. The SOP was registered for the wavelength of the maximum emission power.

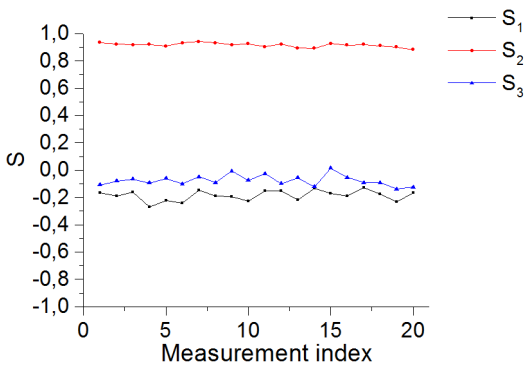

Figure III.3. Stokes parameters for a static monochromatic signal linearly polarized after 20 consecutive measurements.

The stability of the laser emission and the original SOP is guaranteed in the range of the times of the measurements. To that end, it has been measured by registering separately its emission power stability with an optical power meter (OPM) and its SOP stability by placing a polarizer before the OPM. The instability of the central emission wavelength of the ECDL, i.e. the jitter, is compensated by performing a convolution between the registered spectra for the six SOP of the pump.

The representation in Stokes space of the single polarization vector for the recovered points is depicted in figure III.4.

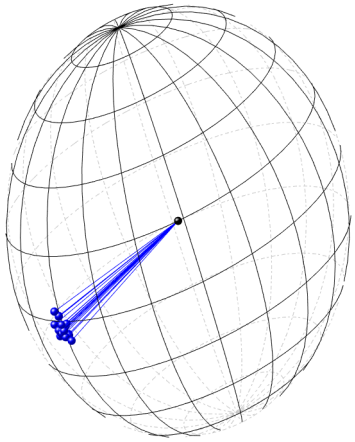

Figure III.4. Poincare representation of the SOP of polarized monochromatic signal after 20 consecutive measurements

There, it can be seen that the dispersion of the vector from the mean is below the 3deg in the Stokes sphere. When represented in the Jones space this means a deviation in the angle defined by the semi axis lower than 1.5deg.

In the next scenario, the linearity of the system was tested. As it has been aforementioned, the system does not measure absolute polarization states rather than relative, so in order to measure its precision, a single ECDL with an electronic polarization controller was employed. The laser was measured in six orthogonal states, precisely the basis of the Stokes space right after the PC. In order to ensure the orthogonality of the six states, the

pigtail that connected the output of the PC to the input of the equipment can be considered free of PDL, and thus the recovered vectors remain orthogonal.

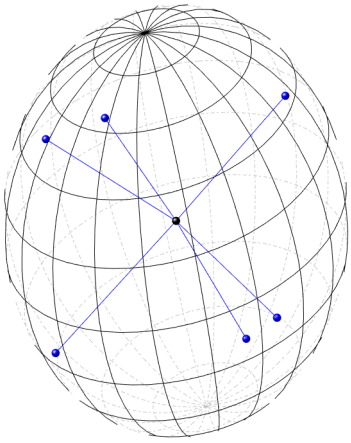

Figure III.5. Poincare representation of the SOP measurement of six orthogonally generated states at the input of the system.

In the fig. III.5 the six measurements are represented. There it can be seen how the system conserves the angular relation between the different SOP measured.

The last scenario of the calibration was set to test the wavelength selectivity of the system. To that end, the output of an external cavity laser was divided with a splitter, one of the branches was connected to a Mach-Zhender modulator. The modulator was fed with a single tone generated by a network analyzer which frequency can be selected in ranges below GHz. The output of the Mach-Zhender and the other branch of the splitter are now combined with a polarization beam combiner and then coupled into the system.

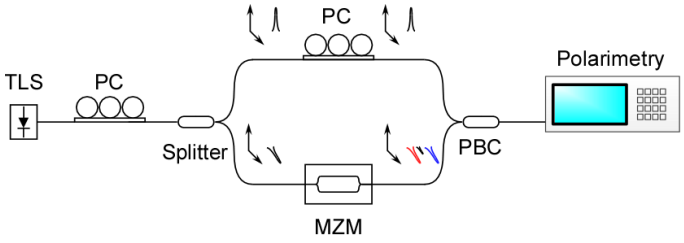

Figure III.6. Schematics for the wavelength calibration set-up

By varying the bias voltage of the Mach-Zhender, the central peak of the modulated signal can be significantly suppressed compared to the modulated tones. Due to the nature of the PBC, the signals introduced in the two branches will output the combiner in orthogonal states, giving as a result then that the tones generated in the Mach Zhender will have both an orthogonal polarization with respect to the signal in the other branch. This signal, that propagates through the other branch without MZM, corresponds to the solely emission of the laser, which at the same time corresponds to the suppressed central of emission of the modulated tone. The final output is made up by the two spectral components of the modulation with a defined polarization, and the central emission coming unaltered in one of the branches with the orthogonal polarization.

Now reducing the modulation frequency in the network analyzer, it can be tested how close the technique can separate the polarization states.

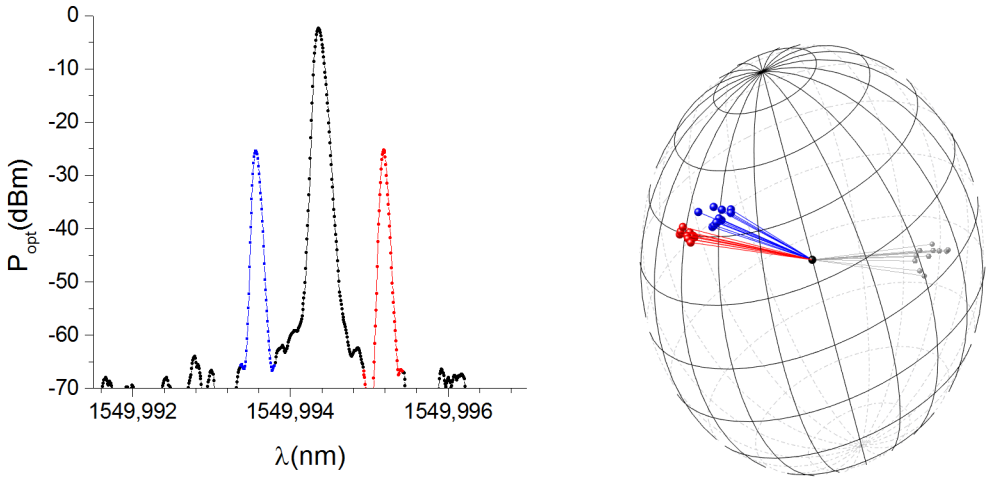

Figure III.7. (Left) High-resolution spectrum of the output signal showing the modulation bands and the center emission wavelength of the laser. (Right) Poincare representation of the SOP of the peaks resolved in the spectra showing the generated orthogonality.

In figure III.7, it can be seen the spectra of the modulated signal for a 100MHz tone and the recovered SOP. It can be clearly seen that the system is not neither affected by close wavelength components nor their relative state of polarization, keeping then the optical rejection ratio of the Brillouin profile employed as gain plus the polarization sensitivity.

With this set-up, we check how spectrally close the system can resolve two orthogonal states. Most of the commercial devices are based on filtering and detection with wider filters which yields to a loss of spectral resolution [Xu '09] [Moller '01]. To the best of our knowledge, the system proposed achieve the highest spectral resolution in a commercial device.

Once the calibration test were satisfactory the method was employed in some frameworks where a spectrally-resolved polarimetry proves to be useful.

III.2. Measurements

III.2.1. Modulated signals

So far, all the signals under test were periodic and their spectra present only discrete tones. On the other hand, signals modulated with random bit sequences present continuous spectra over wide spectral regions. In these cases, as there are no clearly defined components, the recorded spectra are treated averaging over close points. Averaging points would reduce ultimate resolution, but taking in account that spacing can go as close as 10MHz the loss of resolution can be acceptable depending on the nature of the polarization impairment that is to be measured.

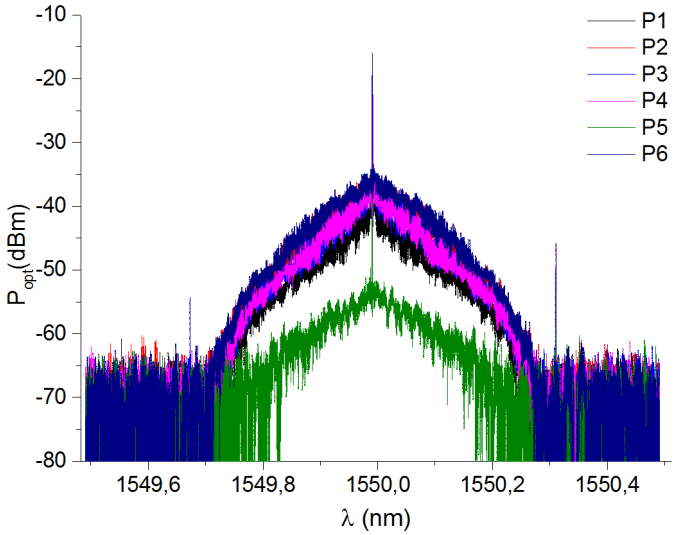

Figure III.8. Spectra of a 40G OOK-NRZ modulated signal projected over six orthogonal SOP of the pump.

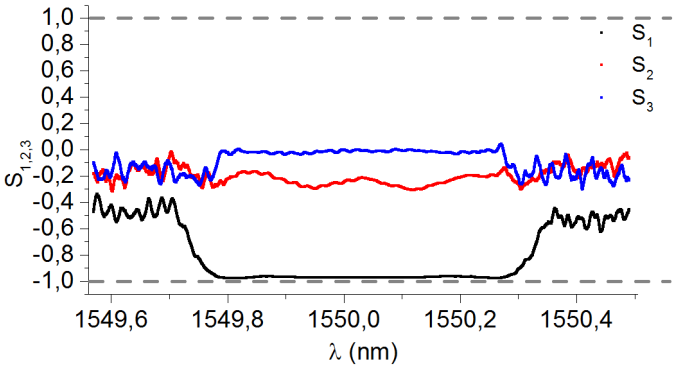

Figure III.9. Stokes parameter for a polarized 40G modulated signal.

In figure III.8, the spectra measured in a 40G OOK-NRZ signal, modulated with a 2^{31}-1 PRBS, for the six different state of the pump are represented. As can be seen, the width of the modulation spectra corresponds to the modulation rate. The different power levels of the registered signal are due to the different gain of the SBS amplification for the different relative polarization states. As here the signal presents one single polarization for the whole spectra, the different spectra look like differing, more or less, in a vertical offset. Notice that the power scale is logarithmic and thus some precaution must be taken when comparing absolute power level. Figure III.9, shows the calculated Stokes parameters corresponding to the spectra measured for the signal presented in figure III.8.

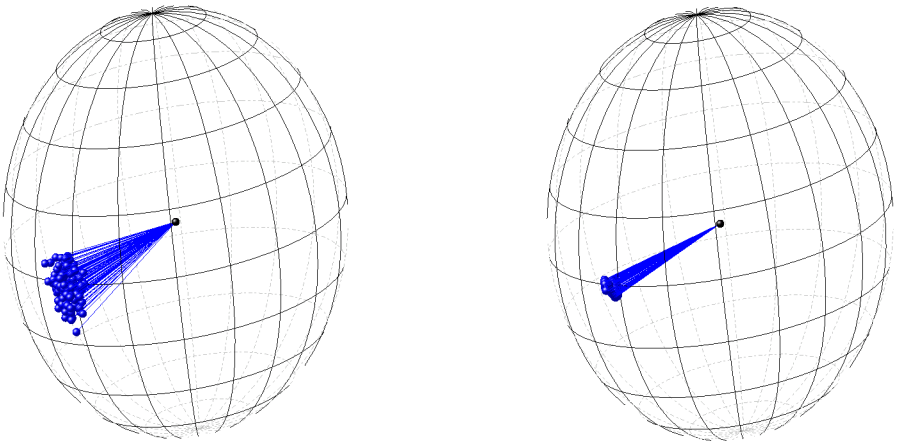

Figure III.10. Reduced dispersion by averaging the recover SOP measurements

Due to the statistic origin of the carrying traffic, the shape of the spectra is not perfectly stable and, in figure III.10 (left), that phenomenon can be seen as a bigger spot for the SOP. The instability is caused by the non-periodic nature of the bit sequence, and its slight variation when performing the consecutive sweeps, for the different SOPs of the pump. This effect can be reduced by performing a moving average, which is equivalent to filter those variations with frequency higher than a certainly value. It is unlike to measure polarization states that from a certain wavelength change their state significantly to the closer one. By applying this average, the system loses resolution but provides more treatable results.

III.2.2. DGD Analysis

As it was showed in previous chapters, the effect of the DGD over the SOP in the Stokes space can be summarized in the formula:

$$\frac{d\vec{S}}{d\omega} = \vec{\Omega} \times \vec{S} \qquad \text{[III.1]}$$

For the most simple case possible built with a single delay introduced just in one axis, the delay can be calculated through the angles subtended for two SOP for two different wavelength. In the general case, the SOP is not aligned in the same plane and thus the angles must be calculated through their projection into a plane defined by Ω .

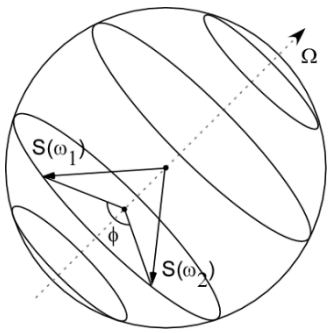

Figure III.11. DGD depicted in the Poincare sphere when generated over one single birefringent axis (Ω)

$$DGD = \frac{\Phi}{\Delta\omega} \qquad \text{[III.2]}$$

For the simplest case, the angle of rotation can be directly calculated from two different SOP and the axis of the birefringence, Ω.

$$\Phi = \sin^{-1}\left\{\frac{\left(\vec{S}(\omega_1)\times\vec{\Omega}\right)\times\left(\vec{S}(\omega_2)\times\vec{\Omega}\right)}{\left|\left(\vec{S}(\omega_1)\times\vec{\Omega}\right)\right|\left|\left(\vec{S}(\omega_2)\times\vec{\Omega}\right)\right|}\right\} \qquad \text{[III.3]}$$

As we have shown in the section 2.4, DGD can be generated by splitting the signal in two orthogonal polarizations and forcing a time delay in one of them, right before they are coupled back again. In this set-up, the delay controls the induced DGD, normally in this disposition the delay times used are greater than the bit time. For this range of values, the depicted rotation in the sphere is greater than one revolution. In these cases, the analysis can be limited to a single axis projection of the spectra and a later analysis.

In the analysis set-up, the option presented here was to perform two sweeps for two orthogonal SOP of the pump. Both spectra are recorded and the data processed. In this disposition, the signal is not manipulated and the deviation of the polarization can be easily extracted from the differential ratio of both measurements. To that end, a polarization switch was placed right after the pump laser and thus the orthogonality between the two states is ensured. The system is similar to that employed for the DGD induced in the polarization suppression technique. In this case, we do not control the polarization at the input of the DGD system and so far we center our analysis in comparing the difference of the two spectra rather than the absolute value of both, as it was done in section 2.4.

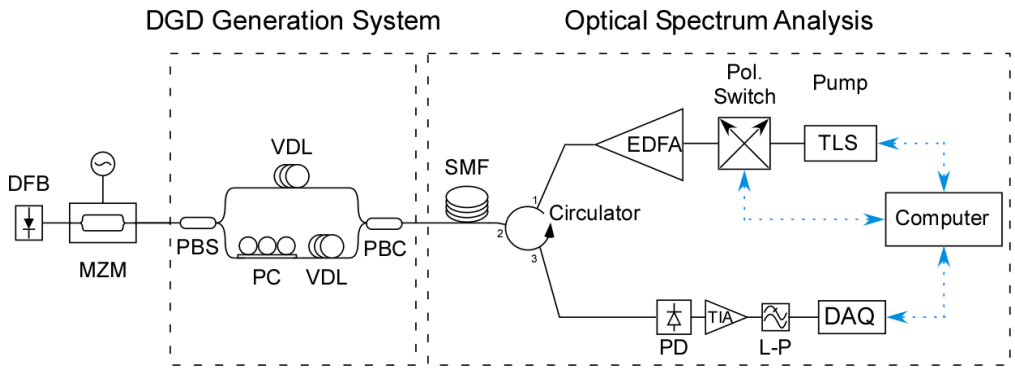

Figure III.12. Schematic for the DGD generation and the polarization analysis.

The set-up is depicted in figure III.12. The polarization switch was arranged right before the amplifying EDFA. Aided by this device, the polarization state of the pump was switched between two orthogonal states. This orthogonality is assumed constant along the fiber. Sweeping now the central emission wavelength and controlling the switch, the spectra of two orthogonal states can be recovered.

Here, the two optical variable delay lines (VDL) controlled the delay between two orthogonal polarization states. The PBS and the PBC define the PSP of the system and the output of the latter couples the signal in the spool of fiber where the SBS filtering takes place. The pump sweep, the polarization switch and the DAQ acquisition rate are all conveniently synchronized to get real time measurements.

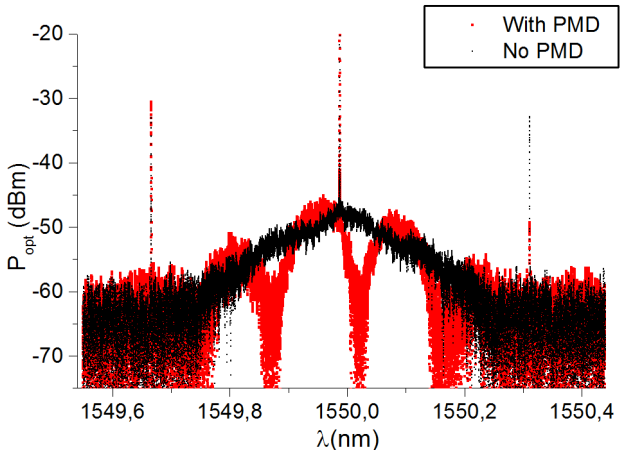

Figure III.13. Spectra of a signal recovered with the set-up whit PMD, red line, and without PMD, black line.

The black line shown in figure III.13 corresponds to the signal with no DGD present. The *sinc* shape of the modulation is depicted with no relevant distortion. In the red line, a DGD of 57.3ps was induced by the delay lines. The visual inspection of the recovered spectra gives an insight of the phenomena and corroborates the expected dependence. What we can see is the convolution of the polarization dispersion spectra and the shape of the modulated spectra. The polarization information is visible now in the spectra but, without a prior assumption of the original signal's shape, it cannot be revealed. By obtaining the differential ratio of the spectra for the two orthogonal polarizations, the polarization walk-off across the signal bandwidth is revealed.

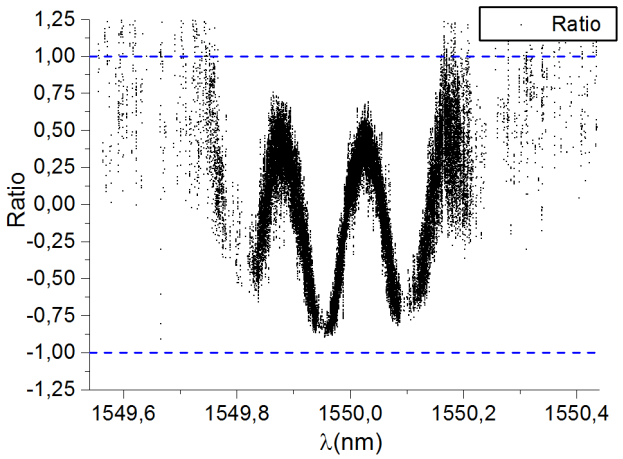

Figure III.14. Ratio of power between two perpendicular polarizations.

The periodicity of the signal in figure III.14 can be clearly recognized. This dependence can be identified as the projection of a circular trajectory onto one axis. In the

case of the figure III.13 and figure III.14 the induced DGD is well above the bit-time and thus the walk off describes multiple revolutions for the whole bandwidth. With this value the spectrum presents multiple maxima and minima. The value of the delay introduced between the branches of the PBS can be calculated by a Fourier analysis of differential ratio of the spectra for the two orthogonal polarizations. The analysis extracts the frequency of variation, which is related to the induced differential group delay as stated in [III.2] The value estimated in the measurement is 55.2ps, which is in great accordance with the 57.3ps established with the delay lines.

With this data analysis, the upper limit for the measurement is limited by the spectral resolution, which is set in 0.08pm. The high resolution in this case allows a characterization of high values, which cannot be acquired with other techniques. Although it could be thought that it is unnecessary to be able to identify such high values, it becomes increasingly important when using PMD compensator. Electronic domain techniques, for instance, fail to measure delay times over the bit time. In those cases the severe distortion of the eye diagram makes its characterization impossible.

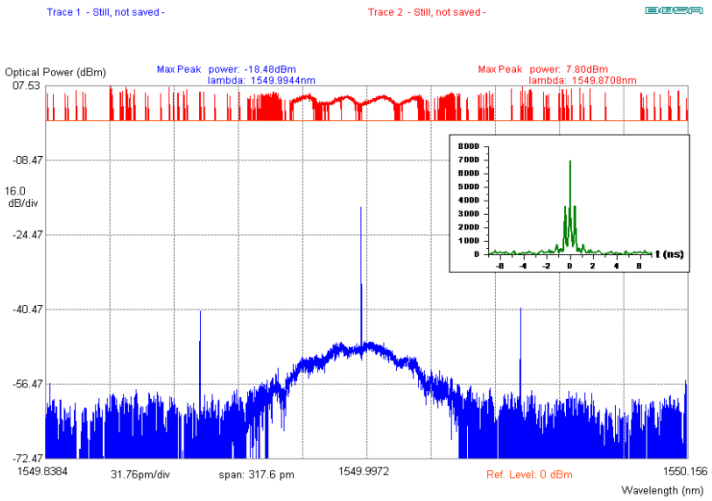

Figure III.15. Interface for the DGD analysis module for a set value of 330ps.

In the figure III.15 and figure III.16, it can be seen the multiple spectra registered, the ratio obtained (red line) and the Fourier analysis performed (green line). The upper graph plotted in the right corner corresponds to the Fourier analysis of the differential ratio. In the green line one predominant frequency can be noticed, the value for the estimated DGD is obtained by analyzing the value of the depicted peaks. The value for the delay in this case is set around 330ps for the figure III.15 and 6.1ns in the figure III.16.

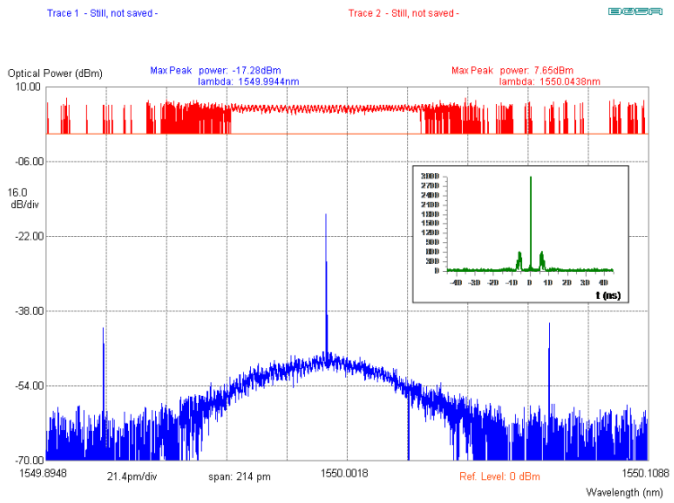

Figure III.16. Interface for the DGD analysis module for a set value of6.1ns.

Figure III.15 and III.16, correspond to screenshots of a preliminary software developed in the early stages of the spectrally resolved polarimeter. Takin advantage of the User Interface, the aim was to develop a monitor of the polarization drifts over the signal bandwidth prior to the full polarization measurement

The analysis presented in these cases is straightforward, as the introduced DGD is constant and set only for two orthogonal polarization states. Higher order DGD could be introduced by performing the same procedure for different delay values between the orthogonal states and/or over different polarization states. Despite this possible arrangement and combinations, the analysis of the ratio will give an effective measurement of the degradation present in the signal due to this polarization impairment. The characterization would relay then in how to weight the measurement values to obtain an effective value for the accumulated DGD.

In the range of DGD values below the bit time, the system does not achieve the same performance. For those values, the depicted arc of the SOP across the signal bandwidth does not complete a rotation, and thus the results from the analysis present high uncertainty. In the range of low DGD a full spectral-polarimetry must be performed.

Low DGD values can be easily generated with polarization maintaining fiber, also referred as High Birefringence (Hi-Bi). This fiber keeps the output polarization state of the signal relatively stable against external factors. This is achieved by forcing a great birefringence between two SOPs by inducing a stress along a defined axis. If the orientation of the input signal is controlled, a DGD proportional to the length of the fiber and the birefringence can be induced in the input signal along the principal states of the fiber.

The set-up is similar to the one presented in figure III.2 where the EPC is used to select the output SOP of the pump. Once the analysis system is set, the input signal was coupled after it went through a defined length of high-birefringent fiber. In the first scenario, the DGD was measured with a reference method and the value obtained was 8.55ps.

Figure III.17 shows the recorded spectra for the system with two orthogonal pumps. The black line corresponds to the undistorted spectrum of the signal while the red one corresponds to the projection once the DGD is induced in the signal.

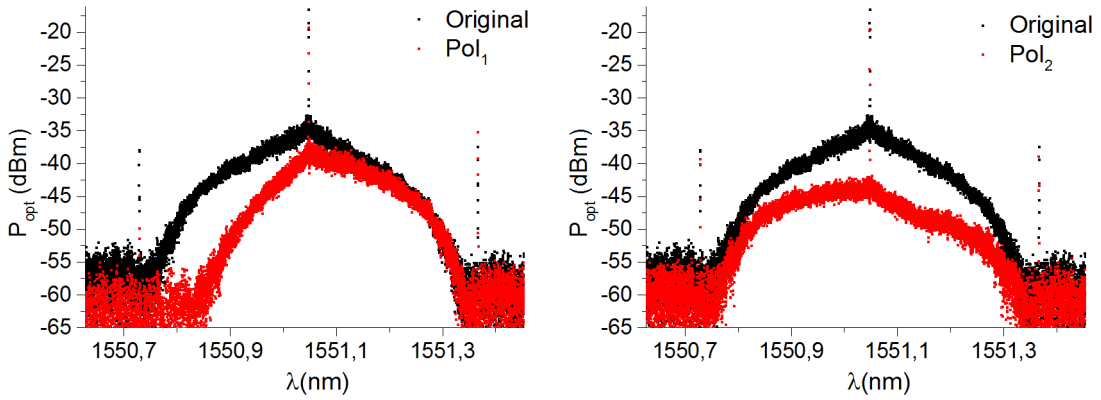

Figure III.17. Spectra registered for two orthogonal SOP of the pump and their original signal where no DGD was induced in them.

Following the methodology explained earlier in this section, the six spectra of the signal were obtain for six SOP of the pump. With these values, the Stokes parameters were calculated. In figure III.18, it can be seen the dependence of these three parameters with respect to the wavelength.

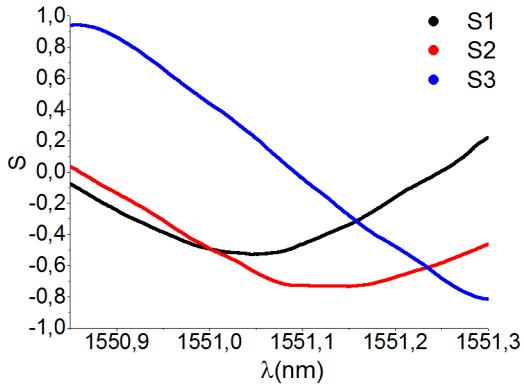

Figure III.18. Stokes parameters and spectrally resolved SOP for a modulated signal with DGD

There we can see a smooth evolution of the three parameters across the bandwidth of the signal. Comparing with the high DGD values, it can be deduced that this would correspond to a small interval of a periodic evolution.

Plotting these three values on the Poincare sphere, we can get a visualization of the evolution of the SOP of the signal. In figure III.19, it can be seen the depicted arc across the signal bandwidth. In this case, the measured DGD through the depicted arc, according to [III.2] and [III.3], gives a result of 8.9ps.

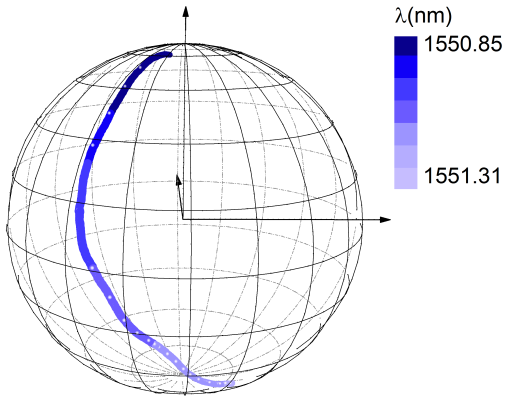

Figure III.19. Poincare sphere and the representation of the Stokes parameters.

This visualization of the trajectory depicted serves also to calculate the axis of rotation. This rotation axis determines the principal states of the system that originates this DGD. If the system had induced the DGD between the linear vertical and horizontal SOP, the rotation axis would have been the axis in the equatorial plane with coordinates [1,0,0].

With the aim of calculating the axis, the algorithm employed is the same that is used to determine the norm of the plane with three points. Measuring three point of the depicted arc, the axis of rotation can be calculated. Assuming the three points, $\vec{S}_1, \vec{S}_2, \vec{S}_3$, are measured, the axis of rotation $\vec{\Omega}$ can be obtained as:

$$\vec{\Omega} = \left[\Omega_1, \Omega_2, \Omega_3\right] \qquad \text{[III.4]}$$

$$\Omega_1 = \begin{vmatrix} 1 & S_{12} & S_{13} \\ 1 & S_{22} & S_{23} \\ 1 & S_{32} & S_{33} \end{vmatrix} \Omega_2 = \begin{vmatrix} S_{11} & 1 & S_{13} \\ S_{21} & 1 & S_{23} \\ S_{31} & 1 & S_{33} \end{vmatrix} \Omega_3 = \begin{vmatrix} S_{11} & S_{12} & 1 \\ S_{21} & S_{22} & 1 \\ S_{31} & S_{32} & 1 \end{vmatrix} \qquad \text{[III.5]}$$

Due to the mentioned instability of the spectra for specific cases, the axis calculations normally is done by averaging the norm vector over different points of the depicted arc, verifying also that the dispersion of the vector do not exceed the reference value for the precision calculated in the calibration scenarios.

In the next scenario, with the appropriate length of the fiber, a DGD of 8.9ps was induced in the system. In figure III.20, it is represented the spectrally resolved stokes parameters and the registered spectra for one single SOP of the pump.

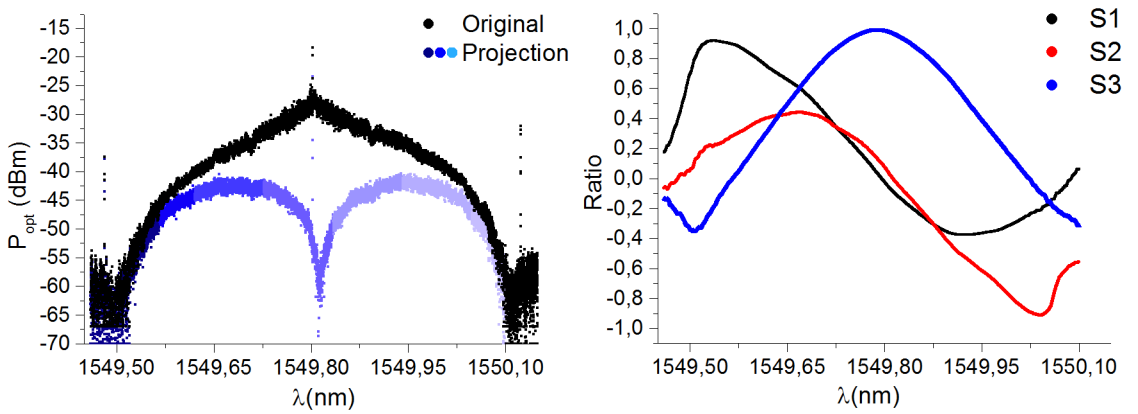

Figure III.20. (Left) Spectra for a 40G modulated signal and one projection after going through the DGD generation stage. (Right) Recovered Stokes parameter of the signal.

The Poincare sphere representation is represented in figure III.21. The SOP of the signal and the calculated birefringent vector. With the information measured for several points across the depicted arc the value of the birefringent vector can be calculated more precisely. To that end, the calculation of the rotation axis was performed for a wide range of point and the average vector calculated.

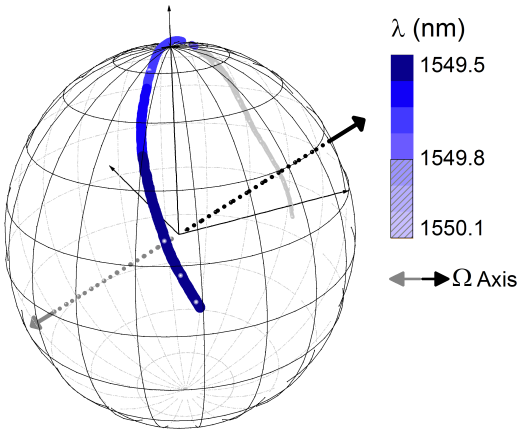

Figure III.21.Poincare representation of the Birefringent axis calculation over the SOP measured

In this case, the birefringent media was set so the rotation would be maximal and thus the trajectory depicts a maximal circle perpendicular to the vector. This representation enables a visualization of the polarization properties of the signal.

The system can achieve a high resolution in DGD values well below the bit-time. In the figure III.22, it can be seen the measured DGD for different reference values.

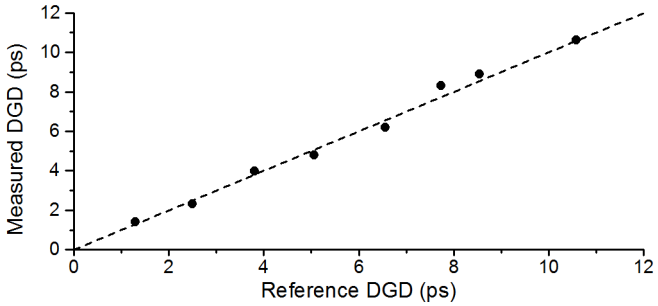

Figure III.22. Measured values for the DGD versus reference induced DGD

So far, all the measurements have been performed across the bandwidth of the signal. However, the sweeps can be performed along greater spans. This feature allows the simultaneous characterization of multiple signals. The sweeps don not need to be reconfigured and the calculation can be performed separately in the analysis stage.

In figure III.23 and figure III.24, it is depicted the case with two different signals with different modulation and different systems. There, it is shown the potential of the technique as it allows a full characterization of the individual channels without filtering or ad-hoc tuning for the detection.

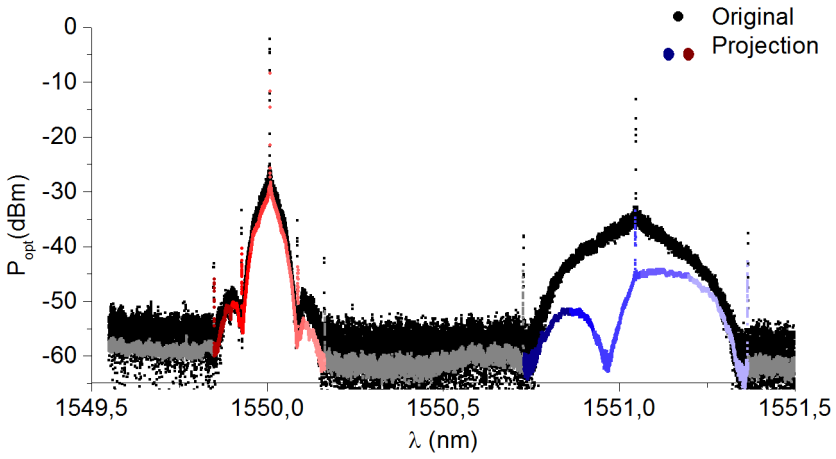

Figure III.23. Spectra obtain for two modulated signal affected by PMD in one state of the Pump and the original signals without PMD.

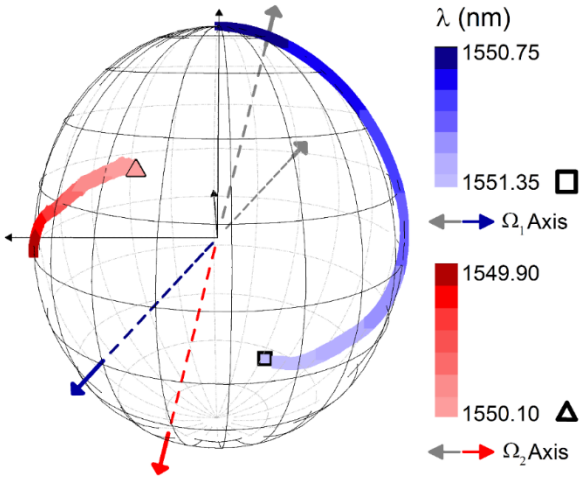

Figure III.24. Retrieved SOP resolved spectrally for two channels. Ω_1 , Ω_2 represent the different DGD axis for both channels

The analysis for two signal does not require different elements or tuning the system. The processing time required in the analysis does not imply a delay in the calculations neither. The method, as it is presented here can perform the sweep without prior knowledge of the system and analyze the polarization impairments in parallel, by processing the data.

III.2.3. PMD characterization

The measurement of the final degradation of the signal in the electrical domain gives an effective but averaged value of the distortion present in the signal. Normally, by measuring this degradation over a long series of measurements and performing the statistical analysis, the transmission system is characterized and the compensation is done according to the analyzed statistics.

The output characterization given with the presented technique allows a further characterization and a deeper understanding of the degradation. Following the approach explained previously, the effect of the PMD represented in the Stokes space can also be explained as the effect of the multiple DGD trunks randomly aligned.

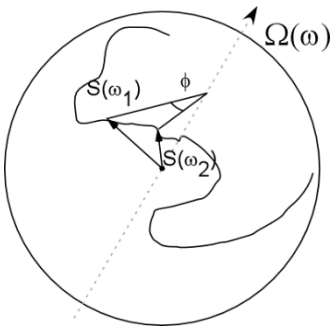

Figure III.25. SOP string depicted in the sphere for a signal with PMD

The most common model in this aspect assumes a large number of concatenated trunks of fiber with equal DGD value but random birefringence axes. The final effect can be

simulated in the Mueller formalism as the resulting matrix of n rotational matrixes with same DGD and different orientation axis.

$$\Omega_{\omega}^{n} = \Omega_{\omega} + R_{n}\Omega_{\omega}^{n-1} \qquad \text{[III.6]}$$

The birefringent effect of a *n* number trunks can be expressed as the summation of all the previous birefringent trunks. This implies that the final value of the vector Ω can be simulated as a random walk process over the sphere. Where the number of trunks approaches to infinity, the components of the birefringent vector become Gaussian random variables. The final value of the DGD has been proved to follow a Maxwellian distribution over the possible DGD values.

On the other hand, the depicted trajectory in the sphere at the end would be an erratic trajectory with no defined axis or angle of rotation. Although this trajectory does not represent a unique state, it parameterizes all the necessary information of this polarization impairment, necessary to achieve a complete compensation.

The effective value of the PMD can be worked out from a mean angle measurable in the trajectory; however, the total length of the arc provides a better insight of the distortion present in the signal [Cornick '05]. The most simple way to simulate the effect of the PMD in a set up is to alternate trunks of high birefringent fiber with single mode fiber paying no attention to alignments in any of them. In figure III.26, the trajectory for two different scenarios is plotted.

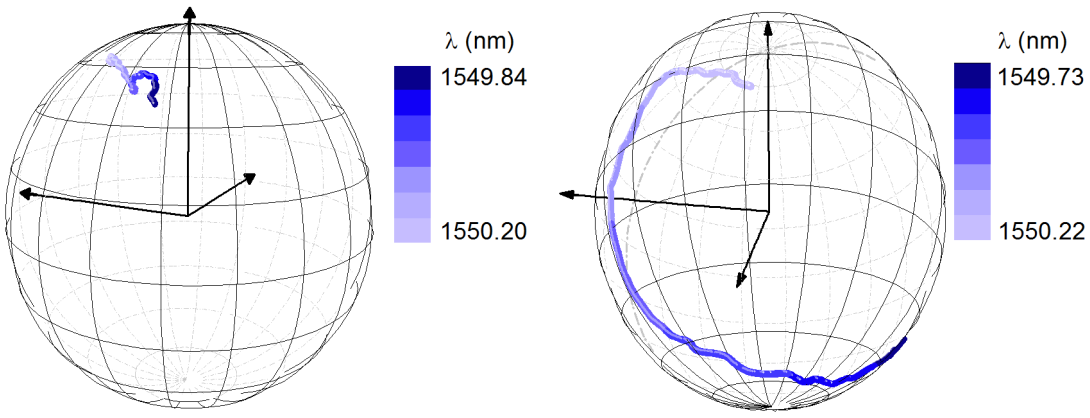

Figure III.26. Measurements of distorted PMD signals by using non-aligned polarization maintaining fiber and standard monomode fiber.

Unlike the simple DGD cases, here it can be appreciated the irregular curvature of the trajectory. There is no single axis of rotation that can be defined for the entire system. However, the length of the depicted trajectory is directly related to the distortion present of the signal [Cornick '08]. The full parameterization of the curve could be used for a complete compensation with fast PMD compensators [Cai '08] [Bülow '04].

III.2.4. Selective Polarization suppression

Based on this high resolution spectrally resolved SOP, we can suppress any desired spectral component of the signal individually. If we now recall the polarization nulling technique depicted in section 2.4 where we induced a DGD on the signal, we see that in that set-up, we had to induce a full rotation of the SOP of the signal. This was a consequence of analyzing the system with just two orthogonal polarizations and thus, we see just the projection on to the plane define by these two states. In that case, we had to induce a high DGD value and we could not fully control the suppression, as we did not know the initial SOP of the incoming signal. Furthermore, in that section we also discussed how there could be cases where the SOP rotation and the plane defined by the SOPs of the pump would not intersect and thus, further alignment or rotation of the signal SOP would be needed.

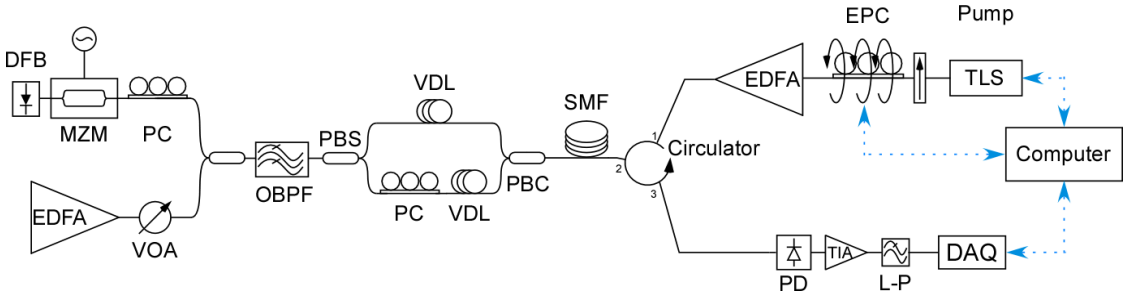

Figure III.27. Set-Up for the polarization drift generator and the spectrally resolved polarimetry

In this case, the measurement performance and the full control over the SOP of the pump enable a precise suppression of any desired component. Here we have tested the system in a 40GHz OOK-NRZ signal modulated with a Mach-Zhender and fed with a pseudorandom bit sequence. The signal was coupled with a -28dB noise level measured over a 0.1nm bandwidth. Once the signal and noise are coupled into the DGD generator, the two VDL are set to induce a delay of 17.1ps. In figure III.28, it is depicted the recovered Stokes vector across its bandwidth. Once the SOP of all the spectral components is calculated, the system can rotate the SOP of the pump to align its state to the orthogonal position of any selected component. Here we have selected three spectral components, which SOP in the sphere is highlighted in red. With the SOP of the pump rotated orthogonal to the selected states, the spectrum is recorded, and the registered optical level at the selected wavelength corresponds only to the noise contribution.

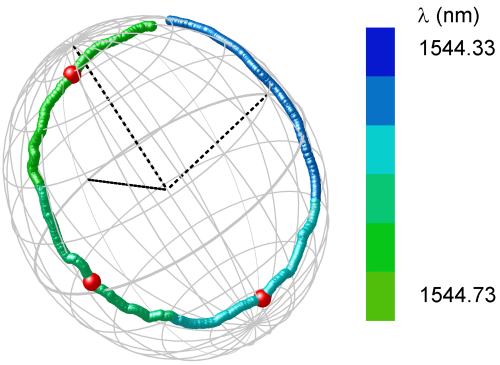

Figure III.28. Poincare representation of the Stokes vector resolved in spectrum for an induced DGD of 17.1ps.

In figure III.29, it can be seen three spectra for the three orthogonal position of the selected points, which are marked in figure III.28. In all of them, the black line corresponds to the registered spectrum of the signal without DGD induced on it. In this case, no polarization drift is present and the whole signal bandwidth presents the same state of polarization. The red trace represents the depolarized noise level introduced by the ASE source and it is registered once the signal is turned off. Each of the gray traces corresponds to the registered spectrum for the different positions of the SOP of the pump. The positons were chosen based on the information recovered from the spectral polarimetry. Based on this information, the orthogonal position for each of spectral components was calculated and the SOP of the pump was rotated to achieve their suppression. In the three cases, it can be seen the suppressed component and the registered value that corresponds to the noise. In this case, an in-band OSNR of 23dB is measured. Results show that, with this method, deviances below 0.5dB can be achieved.

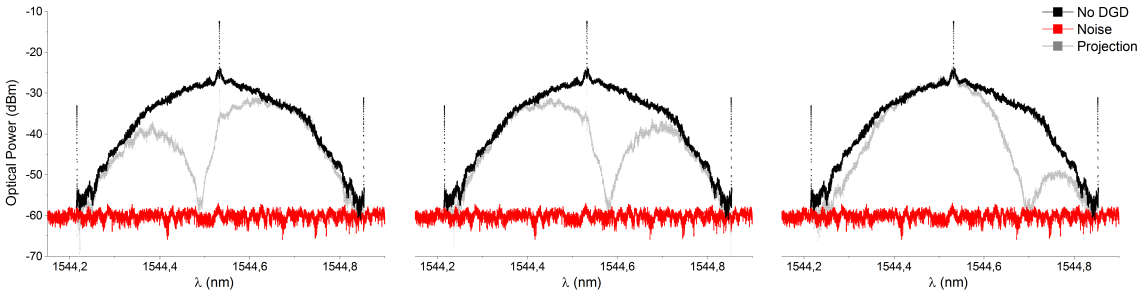

Figure III.29. Spectra for the undistorted signal (black). Spectra affected by DGD with polarization nulling (gray). Noise level (red).

Furthermore, with this characterization, the polarization suppression can be selectively applied for any specific spectral component independently of its SOP. By rotating the SOP of the pump to the orthogonal positions of the arc depicted in the sphere, the system can perform the suppression of every spectral component and thus map the underlying noise level for the whole signal bandwidth.

III.2.5. Non Linear Coefficient measurements

The information extracted from the depicted arc could also be used to assess other polarization related impairments. Earlier in the group, a vast work was performed to formally characterize the polarization distortion present in the non-linear effects. At that time with the available technology, some of the features described could not be resolved. With the developed method, that work is revised and extended.[Heras '07]

Here for the sake of simplicity we recall the widely studied simple model of two co-propagating optical waves in a single model fiber. The non-linear evolution of the SOP of the two signal, pump and probe, can be described with the Manakov equations [Bononi '03]. The evolution of the polarization states represented in the Stokes space can be describes as [Heras '07]:

$$\begin{aligned}\frac{\partial}{\partial z}\hat{s} &= -\frac{8}{9}kn_2t_0^2\hat{t}\times\hat{s}\\ \frac{\partial}{\partial z}\hat{p} &= -\frac{8}{9}kn_2t_0^2\hat{t}\times\hat{p}\end{aligned} \qquad \text{[III.7]}$$

Where $\hat{s}$ and $\hat{p}$ states for the polarization states of signal and pump respectively and the vector $\hat{t}$ is the sum vector of $\hat{s}$ and $\hat{p}$, and thus $t_0^2\hat{t} = p_0^2\hat{p} + s_0^2\hat{s}$. The coefficient *k* states for the wavelength number and n_2 in this case is the non-linear refractive index normalized to the effective area. Operating from [III.7] and having in account [Heras '07]. It can be deduced that the evolution of both vectors is related:

$$\frac{\partial}{\partial z}(\hat{s}\cdot\hat{p}) = \frac{\partial}{\partial z}(\hat{s}\cdot\hat{t}) = \frac{\partial}{\partial z}(\hat{p}\cdot\hat{t}) = 0 \qquad \text{[III.8]}$$

This equations asserts that the relative orientation between pump and probe is fixed and they both rotate around the sum vector $\hat{t}$. Considering now their evolution along the whole fiber, the change of the state of polarization for the signal can be described as depicted in figure III.30.

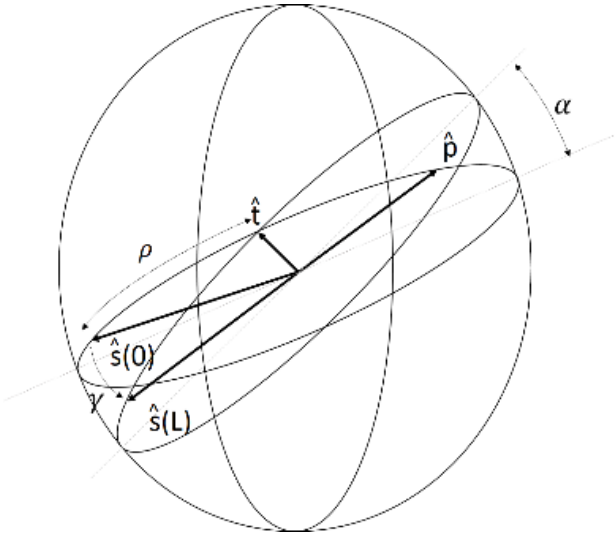

Figure III.30. Stokes representation of the SOP involved in the XPM.

The evolution of the vector $\hat{s}$ can be characterized as a rotation which axis is determined by the sum vector $\hat{t}$. The angle of rotation depends on the relative orientation between $\hat{s}$ and $\hat{p}$ reaching the maxima for $\hat{p}\cdot\hat{s}=0$. The maximum angle of rotation is then:

$$\alpha = \frac{8}{9} k n_2 t_0^2 L_{eff} \qquad \text{[III.9]}$$

Where L_{eff} stands for the effective length of the non-linear interaction. At the end, the deviation of the polarization state of the signal can be described by the angle between the states before and after the amplification, γ. This angle depends on the aforementioned angle α and the angle ρ. Therefore according to this rotation depicted in the figure III.30 the rotation can be describes as:

$$\cos(\gamma) = \cos(\rho)^2 (1-\cos\alpha) + \cos\alpha \qquad \text{[III.10]}$$

This expression allows a full characterization of the non-linear system, through the coefficient n_2, based on the analysis of the polarization rotation of the SOP of the signal.

The setup for the experiment is depicted in the figure III.31. The pump signal is generated with an external cavity TLS and modulated with a Mach Zhender modulator (MZM) biased at the quadrature point. An electrical signal generator provides a 3GHz pure tone for the MZM. The modulated pump is highly amplified with an EDFA before it is coupled with the signal into the spool of fiber. The continuous probe signal is generated with a second TLS. The emission wavelength of the signal was set close enough ($\Delta\nu$<4nm) to guarantee the same polarization evolution along the system. In order to control the SOP of the signal, an electronic polarization controller, PC1, is placed right before it is coupled into the fiber. This controller consists of a polarizer, a half wavelength plate and a quarter wavelength plate and thus the output state and its variations are always known. A second manual polarization controller, PC2, for the pump is placed before the EDFA in order to control the relative

orientation between pump and probe. The spool of fiber was an 11km dispersion shifted fiber (DSF) to increase the non-linear effect.

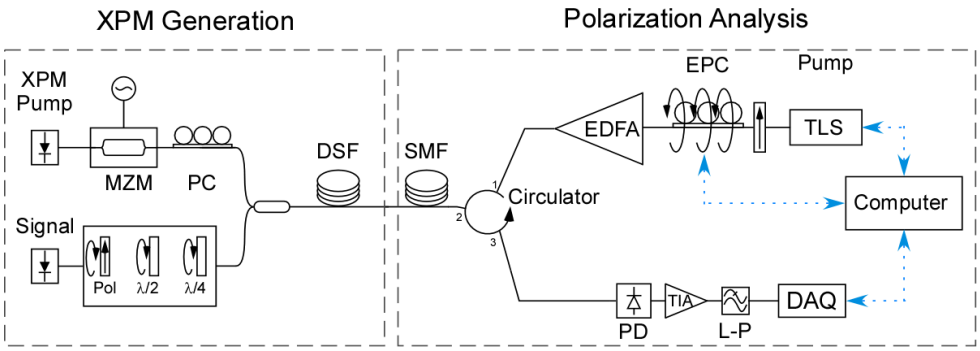

Figure III.31. Experimental set-up for the wavelength resolved polarization analysis of non-linear effects.

With the aid of the PC1, the SOP of the signal is controlled in its origin. On the other end the spectrally resolved polarimetry records the final SOP for the signal and the non-linear induced components. The final state of polarization and/or its change with respect to the original is related with the non-linear coefficient of the system. Analyzing then this information, the efficiency of the non-linear effect can be characterized.

The power spectrum for an arbitrary polarization is depicted in figure III.32. It can be clearly seen in the spectra the modulation band induced by the XPM in the probe signal. The separation of this band with respect to the signal is the same to the pump's modulation frequency. The induced spectral components of the four-wave mixing (FWM) can be also clearly identified, F_3 and F_4. As is widely known, the relationship of central wavelengths for the degenerate case can is $\nu_{F_3} = 2\nu_p - \nu_s$ and $\nu_{F_4} = 2\nu_s - \nu_p$. Once the power spectra is recovered and the non-linear induced components are identified the wavelength-resolved polarization analysis is performed.

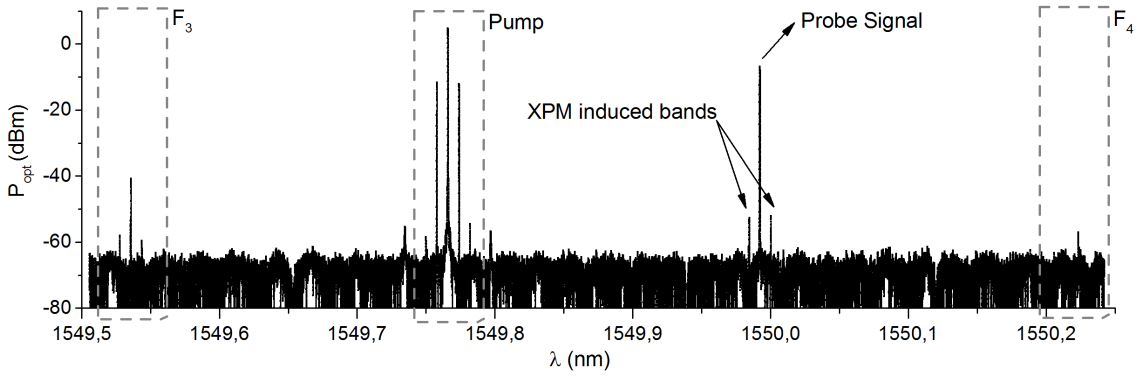

Figure III.32. Optical spectra measured at the output of the DSF.

Once the state of polarization for each component is retrieved, the signals' state was rotated with the polarization controller until the two interacting waves, pump and probe, were aligned. After the origin position was set, aided with the PC1, the SOP of the probe is rotated so its relative orientation with respect to the pump goes from parallel to perpendicular, in

Jones space. In the Stokes space the SOP of the pump remains constant and the SOP of the signal describes an arc from this position to its opposite location in the sphere. Figure III.33 depicts the Stokes representations of the polarization states for the analyzed spectral components. The SOP for all the components are recorded after the signal rotates $\pi/15$ in the Stokes space representation. In figure III.33 the single black vector represents the SOP of the 10mW pump and its modulation bands as their SOP was fixed for the experiment.

The blue trajectory depicts the SOP of the 0.3mW signal in the absence of pump, *s(0)*, and thus non-linear polarization rotation is not present. The red line on the other hand depicts the SOP of the signal once the pump was turned on, and the non-linear interaction takes place, *s(L)*. It can be seen that, when the signal and pump are either parallel or perpendicular, in Jones space, the polarization rotation of the signal is null. On the other hand the maximum deviation, as predicted in equation [III.10], occurs when the signal and pump are perpendicular in Stokes space. Attending to figure III.30, α is depicted here as the angle formed by the planes formed by the SOP of the signal before and after the non-linear rotation. In figure III.33 the normal vectors of the planes are depicted in dark blue and dark red.

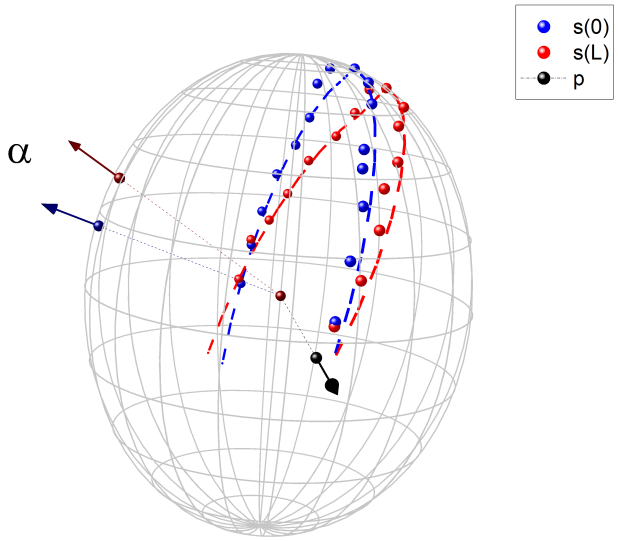

Figure III.33. Stokes space representation of the SOP of the signal when there is no pump (blue) and when the pump is switched on (red) for different relative orientation between pump (black) and signal. Vectors depicts the normal to the rotation plane.

It has been showed the characteristics that the technique can resolve. Not only provides information for wide spectra but also can sense small polarization deviances. Based on its performance and the affordable set-up needed, the system was implemented in the commercial devices developed by Aragon Photonics Lab SLU.

III.3. Implementation

In 2013, the technique was patented first national and later extended to United States. The main claim presented in the patent is the use of the SBS as a polarization

selectivity filter. With this filter, the patent presents a method to spectrally resolved the SOP of optical signals to assess the polarization impairments present in the signal.

At the end of the year, the system was implemented as an optional add-on in one of the products of the company Aragon Photonics SLU. The basic BOSA equipment is based on the Stimulated Brillouin Scattering, hence the task was to implement the polarization control elements necessary in the original schematics without lessening its original specs.

III.3.1. Hardware

The main element that was added in the system was the polarization controller for the pump. The available polarization rotators do not achieve the expected performance. These devices are based on multiple piezoelectric squeezer that, by pressing the fiber, rotates the polarization of the income signal an angle proportional to the induced stress. The voltage supplied to the piezoelectrics drives the stress induced on the fiber. Controlling this voltage, the SOP of the signal changes. However, the device presents a slow deviation with the temperature. Due to this thermal dependences, the calibration of the system with respect to the voltage changes, and the output polarization is not repetitive. This prevents the use of this system, as the orthogonality must be assured at all the time to guarantee the correct recovery of the SOP.

Electronic Polarization state generators on the other hand present a robust alternative. The core of the system is similar to polarization controller, it presents a line of piezoelectrics that induce a stress on the fiber. In this case the induced pressure is fixed and does not range among different values. By polarizing the incoming signal in the device at a known angle, and calibrating the rotation with respect to the applied voltage, the six principal states of the Stokes space can be generated. [Yao '05]

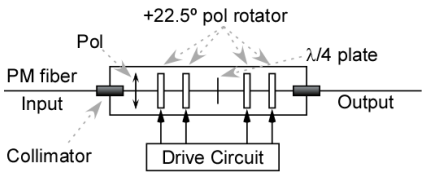

Figure III.34. Schematics of the polarization state generator.

The module is controlled through a TTL electric signal that is fed in a 10-pin port. The signal is generated by the digital output port of the same DAQ that samples the output signal of the detector. This DAQ is connected to the motherboard of the systems that also controls the sweep of the laser. As we have shown, the analysis of the data plays an important role in the results and thus great part of work was devoted to development of the treatment and analysis of the data

III.3.2. Software

The software was developed using C# aided by the Visual Studio IDE. This language presents default control libraries for the DAQ and the GPIB. In the main routine the DAQ samples the signal from the detector, controls the polarization state of the pump via its digital outputs and acquires the trigger signal from the pump. The laser sweep is controlled via GPIB but due to the technical requirements, the synchronization is done using the trigger instead the GPIB.

In the first stage the measurement of the spectra for the six states is done. These six spectra are saved in the buffer and from these data the stokes parameters are obtained. The acquisition rate of the DAQ and the sweep speed of the system allow a high density of points in every sweeps. The spectral sampling can rise up to 1MHz. However the width of the filter limits the resolution to 10MHz. The vast amount of points that can be registered in the sweeps was a major issue especially when the calculations were done.

In order to reduce the complexity and processing time of the data analysis, the software presented two routines for two different scenarios. The first scenario was the measurement of narrow spectral signal such as single lasers, modulation tones or train pulses. The second scenario is intended for the analysis of modulated signals and monitoring its polarization related impairments.

In the first scenario, either the user or the system itself selects the peaks which SOP is requested. In the software routine, the system performs the six spectra measurement and forces their convolution based on the spectral position of the selected peaks. The SOP of the selected signals is later displayed in the Poincare sphere. The interface also provides angles, rotation and some other relevant information of the spectra.

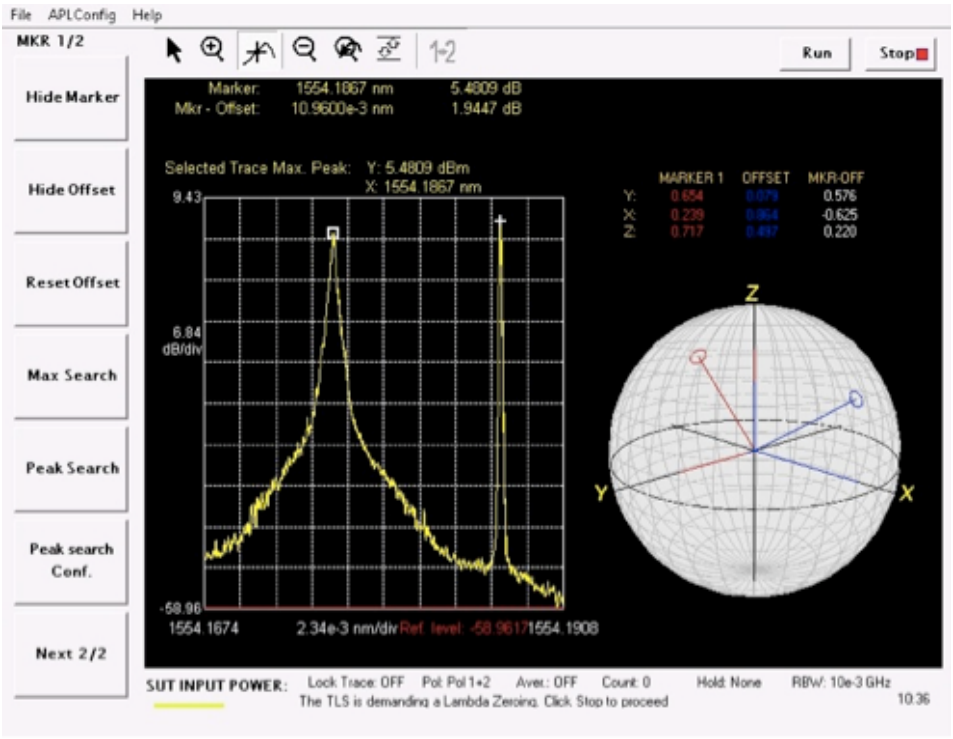

Figure III.35. Interface of the polarimetry module for the SOP of single peak analysis.

The second application has been designed for the analysis of polarization impairments in modulated signals. In this case, as the modulated signals are wider the system performed first a selection of the bandwidth of the signal. To that end, two option are available, the first one is the manual selection of the spectral region and the second one is an automatic identification based on the power levels. Later on, the arc described by the SOP of the whole bandwidth is plot in the sphere as a continuous string. In this case, the analysis of the SOP for the bandwidth includes the estimated rotational axis and the estimated DGD based on the rotation of the values and its deviance from a circle fit.

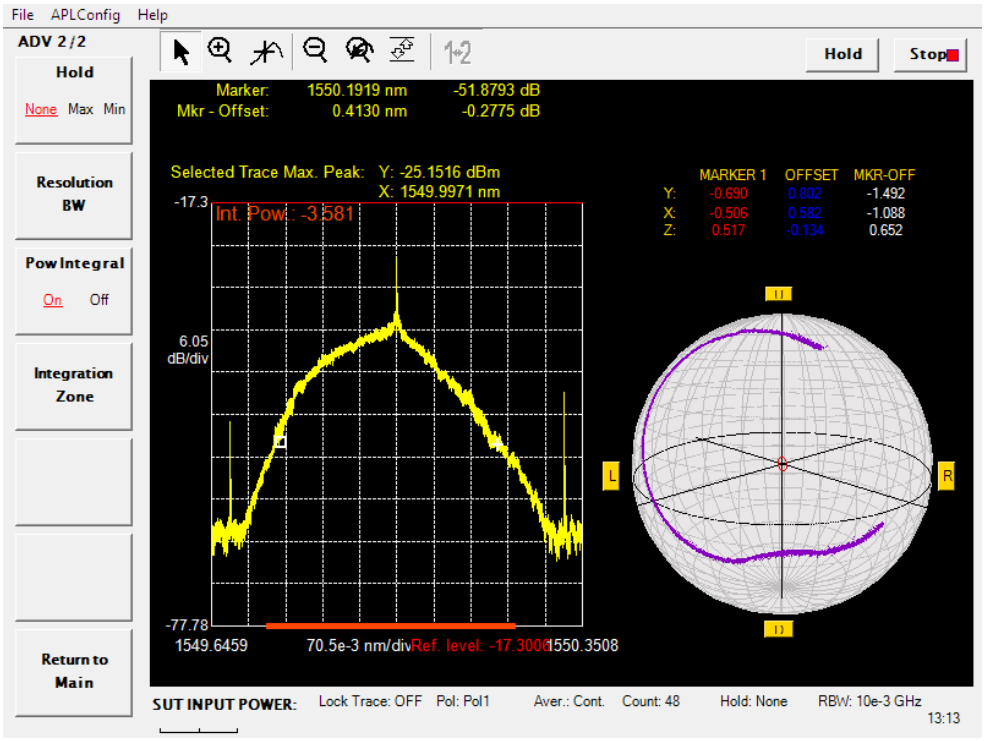

Figure III.36. Interface of the polarimetry module for PMD measurement.

In both cases, the designed user interface was integrated in the prior frame according to the same aesthetic principles. In the developer layer, all the analysis routines and variables were encapsulated in such way that new analysis procedures could be easily implemented for ad hoc customization.

III.4. Conclusion

We have presented a new method for the measurement of spectrally-resolved SOP of optical signals taking advantage of the spectral and polarization selectivity of SBS. Based on its spectral resolution, the technique achieves a high resolution to measure the SOP and also a high rejection ratio as it can measure spectrally close components. So far the SBS has been used only because of its narrowness and, except for a few cases [Wise '11], its polarization dependence has been compensated rather than exploited. Throughout the characterization of the polarization discrimination we have proved that with the appropriate control all the polarization characteristics of the signal can be obtained in the same way

Without need of high rate detection, the system outcomes a complete characterization of the SOP that allows a visualization of any polarization related impairments for multiple channels, without losing in band resolution. Unlike state-of-the-art methods [Xia '11] [Xia '12], that require alignment for each channel, the proposed system can measure in-channel polarization drifts along the whole C+L band, which yields to a full characterization of all-order PMD values for each channel without need of channel filtering, demultiplexing or alignment. Its all-optical origin makes it also insensitivity to other

dispersion effects such as Chromatic Dispersion and makes it scalable to higher transmission rates.

The spectrally resolved SOP of the signal has been proved a useful characterization of the signal beyond the monitoring polarization related impairments. So far, the analysis has never reached the resolution achievable with the SBS and because of that it has not been deeply studied. This technique allows discriminating the contribution of different linear and non-linear impairments to the polarization dispersion that are present in a traffic optical signal, which can be useful to determine if such a scenario is suitable for applying conventional PMD compensation techniques. By analyzing the relative orientation between the Stokes vectors of the involved spectral components, the optimization of this dispersion compensation can be performed. It has been shown that, the effects induced by the PMD and those caused by the non-linear effect are different, based on this difference the polarization impairment present in the signal can be classified as well.

Based on the acquired background for the last years in the development of technical equipment, the technique and the algorithms for the calculation and analysis of the state of polarization were implemented in a commercial devices. Two tasks were addressed at the same time, the development of the systems and its merge on an already functional device without lessening its actual performance.

IV. High-Resolution Spectral Density histograms

The aim of this chapter is to study the ultimate properties of the optical spectrum analysis to identify noise and signal. The development of optical communications has always sought for more efficient modulation schemes. In order to increase the spectral efficiency, different physical properties of light have been used to carry data. By conveying the signal's physical characteristics with non-periodic data, its difference with the noise gradually fades. With the development of dense wavelength multiplexing, the signal loses its unique traceability in the conventional optical spectrum analysis because then, noise and signals share the shame bandwidth. However, the spontaneous origin of the noise and its lack of coherence could be employed for the differentiation with modulated signals.

IV.1. Introduction

The most common analysis technique in electrical domain is the eye diagram, as it is widely known is based on the synchronous sampling of the amplitude values over a lapse of time. With the recovered sampling points, the shape of the pulse is reconstructed for several pulses and its degradation can be estimated. Traditional eye diagram measurement usually involves using a digital oscilloscope and requires collecting many data during a certain lapse of time [Ohteru '99]. Most of the analysis techniques in the electrical domain require prior knowledge of the incoming signal and hence, the analysis becomes format dependent. Ultimately, this effect narrows its appropriateness in flexible and adaptive networks.

In this chapter, we studied the suitability of improved optical spectrum analysis for the differentiation of signal and noise. The measurement principle lays on the inherent physical difference that exists in the coherence of noise and signal. Optical noise, due to spontaneous emission cannot interfere with itself as it lacks coherence. This means that, in the reception-end, all the properties associated to coherence, such as interference or polarization state, cannot be registered. The signal on the other hand because of its nature, is set as monochromatic as possible, which increases its coherence and grantees the possibility of longer transmission distances, reducing also the impact of wavelength dependent impairments.

In the most simple digital communication scheme, the optical carrier is modulated in the time domain with a bit stream that codifies the transmitted information. In the frequency domain, the recovered spectrum can be depicted as a convolution of the spectrum corresponding to the optical carrier and the modulation data. These data are made up by a sequence of unitary bits which duration is related to the modulation rate and which value, 1 or 0, depends on the transmitted information. If we now think of a repetitive sequence of information, this bit stream then can be plotted in the frequency domain as a single bit convolved with a comb spaced according to the information sequenced. This iteration of equally shaped bits generates spectral gaps which power spectral density is zero. This effect is caused by the interference between successive bits and their relative phase difference due to their time difference. The periodicity in the stream analyzed determines the position and width of these gaps in the spectra.

The spectra of repetitive data patterns consist of combs of discrete lines. The spacing of the discrete lines is inversely proportional to the pattern length. Short patterns have greater spacing between spectral components and longer patterns present closer components . For an infinitely long pattern, the spectral line spacing is infinitesimal, effectively making the spectrum continuous. The resolution bandwidth of the technique employed to resolve the spectrum might alter the appearance of the spectrum. If the resolution is greater than the spacing of the discrete lines, the original shape of these lines would not be resolved and the spectrum would appear to be continuous. Techniques with narrow spectral filter imply lower

spectral density and thus problems associated to sensitivity and low power values are involved. The trade off between high enough resolution and sufficient measurable power limits the employability of high resolution. Unlike the signal, the shape of the PSD of the noise does not depend on the filtering technique employed or its resolution.

Here, the principle of operation is based on the analysis of the registered values of the spectra due to the presence of noise. For that purpose we study and analyze different scenarios for both contributions and their interaction.

IV.2. Power spectral density

IV.2.1. Modulated signal

The optical power spectral density of a given function indicates the distribution of the optical energy for the different spectral components of the signals. As it is a value that depends on the width of the spectral components involved, the value is given either in dBm/Hz or dB and the measurement bandwidth employed. Generally, it is obtained from the squared modulus of the Fourier transform of the temporal signal. However in the case of modulated signals, the use of the Fourier transform may no longer be valid.

The complex field of an electromagnetic wave can be expressed in terms of its spatial and temporal dependence.

$$\tilde{E}\left(\vec{r},t\right)=\hat{e}\cdot E\left(r,\rho,\phi\right)\cdot E\left(t\right) \qquad \text{[IV.1]}$$

The temporal evolution of the optical carrier can be expressed considering its amplitude term modulated.

$$E(t)=A\left(t\right)\exp\left(i\omega_0 t\right) \qquad \text{[IV.2]}$$

In digital communication, the information is coded as a stream of n bits with binary values 0 or 1, and their width is characterized by their bit time, T_b. The amplitude can be then represented as:

$$A\left(t\right)=\sum_n b_n A_p\left(t-nT_b\right) \qquad \text{[IV.3]}$$

Where the values for b_n are defined by the coded information, and A_p stands for the pulse shape, which normally is a rectangular pulse. It is usual to express the bit stream as Dirac comb multiplied by the bit sequence analyzed.

$$b\left(t\right)=\sum_n b_n \delta\left(t-nT_b\right) \qquad \text{[IV.4]}$$

According to [IV.3] and [IV.4] the power spectrum of the total signal *A(t)* can be expressed as

$$S_A(\omega) = \left|\tilde{A}_P(\omega)\right|^2 \cdot S_b(\omega) \qquad \text{[IV.5]}$$

Where $\tilde{A}_p$ is the Fourier transform of the pulse amplitude A_p, and S_b states the power spectra of the bit sequence.

$$\tilde{A}_p(\omega) = \int_{-\infty}^{\infty} A_p(t)\exp(i\omega t)\,dt \qquad \text{[IV.6]}$$

$$\left|\tilde{A}_p(\omega)\right|^2 = P_0 T_b^2 \sin c^2(\omega T_b/2) \qquad \text{[IV.7]}$$

The shape of the spectral density of the rectangular pulse is the widely known *sinc* function with zero values for those spectral components that match the condition $\omega = 2\pi n/T_b$ for $n>0$.

The Fourier transform of any function exists only if the function is integrable, which in most of the cases works only for functions that have significantly non-zero values only in a finite time interval. Here, the random sequence of bit does not satisfy that restriction. However, the Wiener-Khinchin theorem states that, for stationary random processes the PSD can be obtained from the Fourier transform of the correlation function. In that case the correlation function, Γ_b, of the bit sequence can be calculated as:

$$\Gamma_b(\tau) = \frac{1}{T_b}\sum_m r_m \delta(\tau - mT_b) \qquad \text{[IV.8]}$$

Where the correlation factor would depend on the sequence transmitted.

$$r_m = \lim_{N\to\infty}\frac{1}{N}\sum_n b_n b_{n+m} \qquad \text{[IV.9]}$$

If we assumed an infinite long random sequence, i.e. that 0 and 1 have equal probability, the factor reduces to $r_0=1/2$ and $r_m=1/4$ when $m\neq 0$.

Finally, the spectral density of an optical bit stream can be expressed replacing in [IV.5] the Fourier transform of [IV.8]:

$$S_A(\omega) = \left|\tilde{A}_p(\omega)\right|^2 \frac{1}{T_b}\sum_{m=-n}^{n} r_m \exp(im\omega T_b) \qquad \text{[IV.10]}$$

$$S_A(\omega) = \frac{\left|\tilde{A}_p(\omega)\right|^2}{4T_b}\left(1 + \sum_{m=-n}^{n} \exp(im\omega T_b)\right) \qquad \text{[IV.11]}$$

When substituting [IV.7] in [IV.11], only the term with *m=0* remains as the *sinc* function vanishes for all frequencies such that $\omega = 2\pi m/T_b$ except for *m=0*. The shape then is the expected for a single pulse of duration T_b.

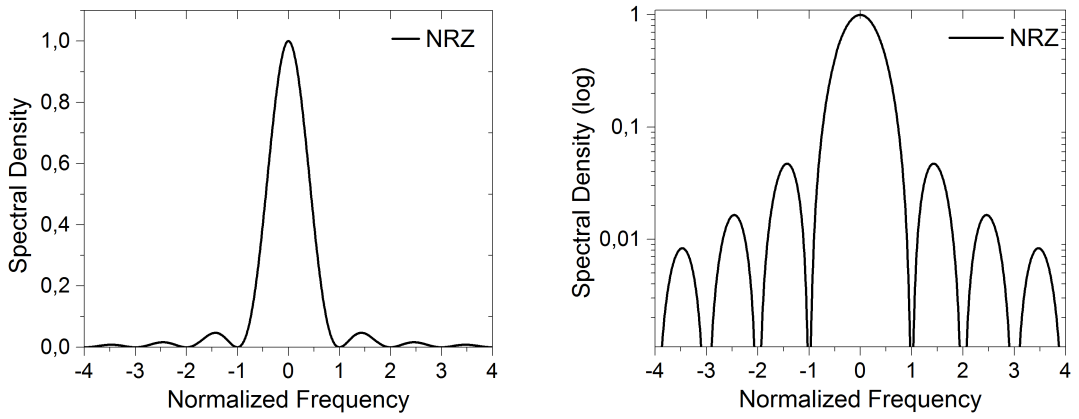

Figure IV.1. Power Spectral Density of a NRZ modulation

If we know think of the same scenario but this time with a repetitive pattern the shape of the spectral power density changes. If we assume that we have a pattern formed by *L* bits that is repeated continuously, we can now describe the stream as the convolution of this repetitive pattern with a Dirac comb, which separation between deltas will be the length of the pattern.

$$b(t) = \sum_n b_n \delta(t - nT_p), \quad T_p = L \cdot T_b \qquad \text{[IV.12]}$$

The envelope of this final spectrum will correspond to a *sinc* shape, because its origin is the bit square shape and thus its zero points lay in multiples of the inverse of the bit-time. Likewise, the pattern iteration is described in the spectral domain as a comb of deltas; therefore the resulting PSD is a convolution of the *sinc* with the comb. Thus, the pattern length generates some zeros in the PSD related with its length. The longer the pattern is, the closer the zeros lays.

$$S_A(\omega) = \frac{\left|\tilde{A}_p(\omega)\right|^2}{4LT_b}\left(1 + \sum_{m=-n}^{n} \exp(im\omega T_b)\right)\sum_{s=-n}^{n} \exp(is\omega LT_b) \qquad \text{[IV.13]}$$

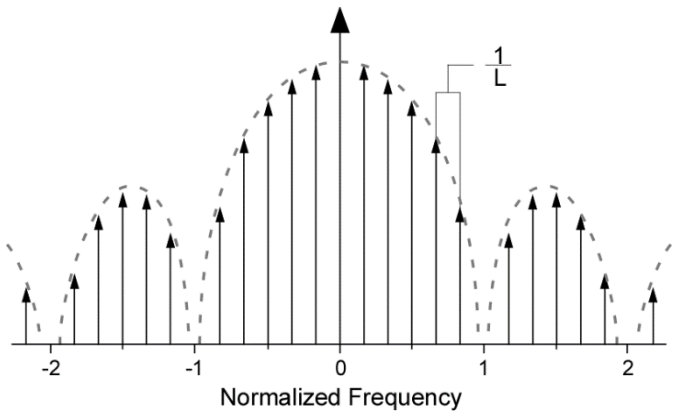

Figure IV.2. Power Spectral density of a pattern signal

The main difference of these two scenarios is the correlation of the bit sequence. In the case of completely random bit sequence the spectral density preserves the shape of the single pulse, on the other hand the iteration of the pattern generates that the PSD exhibits a concentration of the power of the signal in discrete spectral components which position and spacing is related to the pattern.

It can be seen in the figure IV.2 that the narrower the gaps, the more performance is required to fully characterize the PSD of the signal. When the spectra is recorded with resolution in the range of the spectral gaps or above it, the PSD is averaged and thus the gaps cannot be resolved.

In fig. IV.3(b) we can see the PSD generated by a 10G NRZ modulation with a repetitive pattern of 2^7-1 sequence. It can be seen the spectral components corresponding to the 128 length repetitive pattern, and the $sinc^2$ shape can be noticed in the envelope. In the detailed graph, we can see the shape of the comb and how the intermediate spectral components present no power. If we analyze now a longer pattern, such as a 2^{23}-1 pseudorandom sequence bits (PRBS), the sequence is longer and the spectral components appear closer. In that case, with the spectral resolution used here, the whole spectra appears as a continuous. This situation resembles an infinite random sequence, which yields to the conclusion than the spectral density recovered and its features depend on the resolution of the spectral analysis.

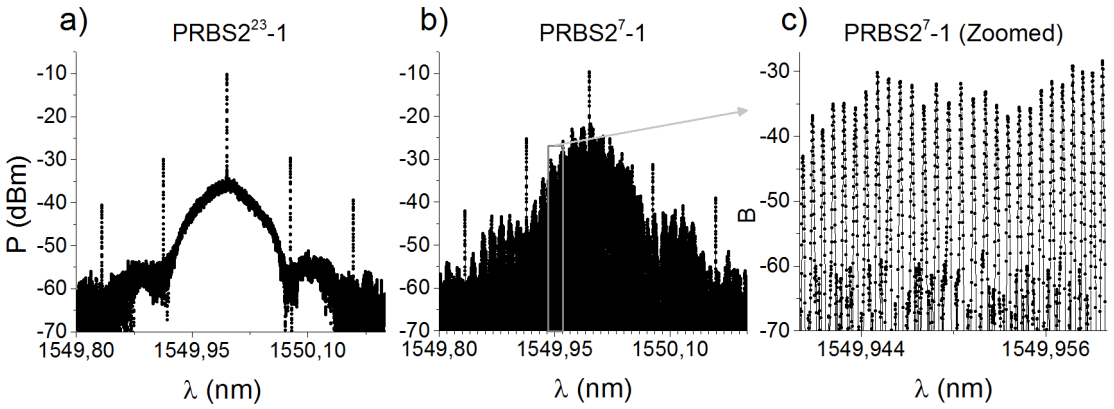

Figure IV.3. Power spectra depending on the length of the PRSB sequence

IV.2.2. Noise

The most common noise in real scenarios comes from the spontaneous emission of EDFA. This spontaneous emission can be characterized as the emission of non-correlated photons which energy range is limited by the fluorescence band of the Erbium present in the EDFAs. Usually, the modelling of this kind of noise is done by simulating an infinite number of non-correlated emissions, which yields to a flat shape for the power spectral density. Precisely, it can be defined as a flat function with constant value N across the bandwidth of the EDFA amplification range.

$$N(t) = \sum_{\Omega} C_k \cos(\omega_k t + \theta_k) \qquad [IV.14]$$

$$N(\omega) = N \qquad [IV.15]$$

In fig. IV.4, it is depicted the spectral shape of the output of and EDFA with no input signal on it. Unlike the signal, the noise presents no coherence, which leads to a flat spectrum. The limited bandwidth in this case is due to the optical band-pass filter placed right after the output of the EDFA. The spectral density of the noise generated by the EDFA and the noise floor of the optical spectrum analyzer can be indentified. The registered value of the noise PSD depends on the width of the filtering used while the total noise value is independent on the filtering technology. In this case, the PSD values correspond to the 0.08pm filter employed by the BOSA.

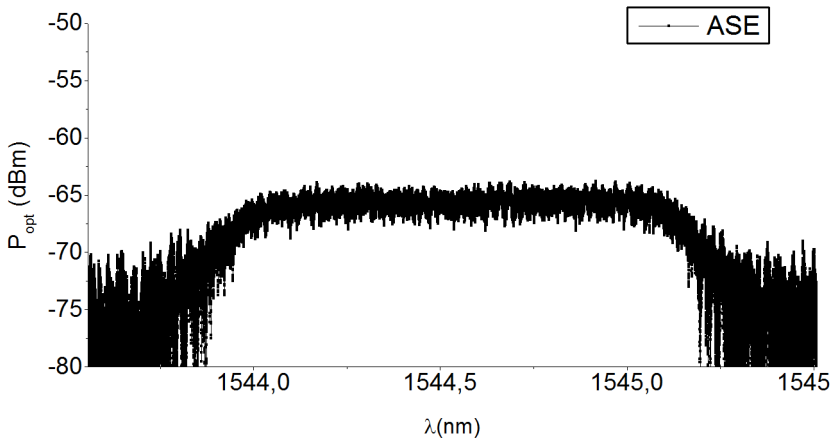

Figure IV.4. Power Spectra of filtered noise.

IV.2.3. Channel

Active channels present both components, signal and noise. For this analysis, we couple the 2^7-1 PRBS signal employed in the previous section with the filtered noise. The recorded spectra is depicted in fig. IV.5.

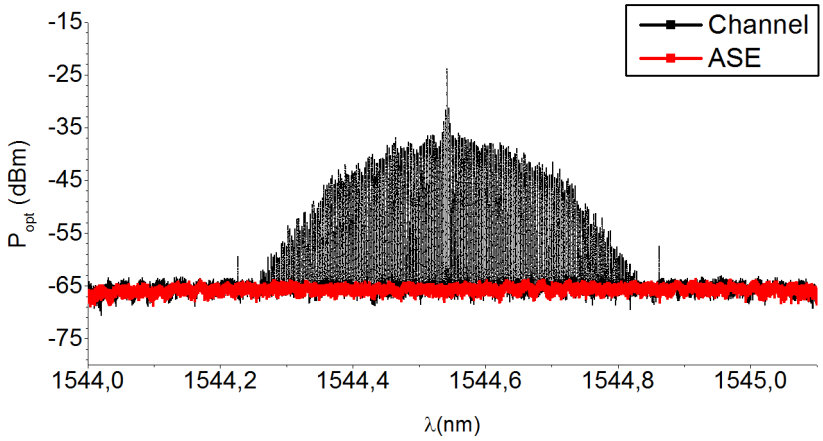

Figure IV.5. Power spectra of a distorted channel

In the black line, we can see the coupled signal and noise and in the red line, we picture only the noise recovered when the signal is turned off. If we zoom in, we can identify the different spectral components.

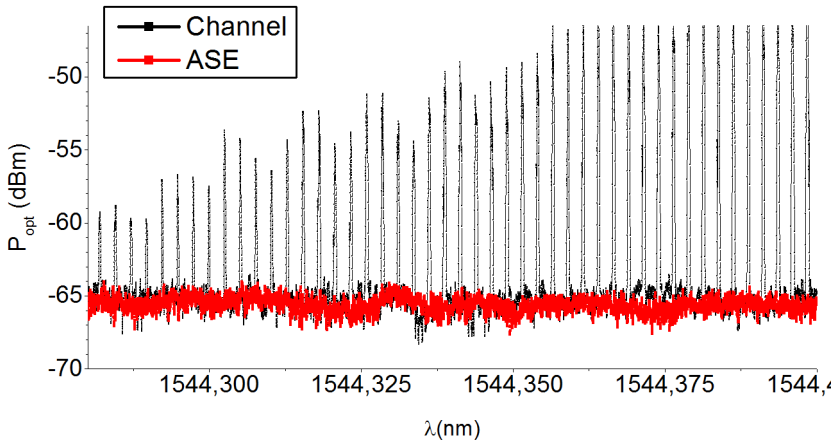

Figure IV.6. Zoomed in region of the power spectrum of a pattern signal with underlying noise.

Here, it can be clearly seen that in those spectral gaps where the signal presents no component, the PSD corresponds only to the noise. On the other hand, when signal and noise are present, the PSD of the noise cannot be resolved and thus the corresponding signal and noise ratio cannot be estimated.

IV.3. Instantaneous Power Spectrum.

Normally the PSD of the optical signals is recovered with optical spectrum analyzers employing different filtering techniques. The most basic OSA consists of a tunable optical filter, that can be tuned along the desired wavelength range, and a photodetector that registers the optical power passing through the filter. The technical restrictions present in the design of the device impose a thorough analysis of the measurement that is intended to obtain and the physical limitations in the actual registered values.

The PSD measurement, as it has been defined previously, requires the analysis of an infinite long stream of bits. In practical cases, that may not be achieved and depending on the filtering technique, the recovered value of the PSD may vary. In our case the limitation is imposed by the acquisition time in the registering stage of the BOSA and the effective time that the SBS filters any precise spectral component of the signal while sweeping the whole spectra. The registered signal at the detector can be then defined as the instantaneous power spectra for a finite time of the incoming signal.

This windowing analysis is cited in the bibliography as instantaneous power spectrum or periodogram and is defined as follows [National Semiconductor '80] [Hobbs '11]:

$$\hat{P}_P\left(e^{j\omega}\right)=\frac{1}{N}\left|\sum_{n=0}^{N-1}x(n)e^{-j\omega n}\right|^2 \qquad \text{[IV.16]}$$

It can be mathematically demonstrated that the expectancy of the Periodograms tends to the PSD when the analyzed signal is long enough.

$$PSD\left(e^{j\omega}\right) = \lim_{N\to\infty} E\left\{\frac{1}{N}\left|\sum_{n=0}^{N-1} x(n)e^{-j\omega n}\right|^2\right\} \quad \text{[IV.17]}$$

Note that we are only considering random processes because stationary signals present temporal repetitions and then its PSD can be directly calculated from Fourier transform, considering it as a piecewise function of a finite sequence. In random processes, the periodograms are employed to estimate the PSD, if no other consideration is taken, by repeating its acquisition and averaging over a given number of samples.

In the case of random signals, it can be considered that the periodogram evaluates the squared Fourier transform of a finite sequence of bits. This truncation and the continuous change of the analyzed stream causes the variation of the values of the periodogram for each component. Giving thus a variation of the registered value in a range of values determined but the uncontrolled series of bits analyzed. By performing an average over multiple measurements, we can obtain the real PSD of the spectra.

Based on this approach, when random signals are employed, the recovered values filtered by the SBS technique for a specific component can be considered an effective measurement of its instantaneous power spectra. The filter, based on the interaction between acoustic and optical waves, can be considered and evanescent Bragg grating with limited length that filters part of the incoming signal on the fiber [Govind P. '06b]. Based on that premise, the system can evaluate the dynamic of the instantaneous power spectra of a defined component. The main purpose is to find certain situations for the signal in which, as it was shown in static measurement, the spectral power of certain components vanishes and the noise is revealed.

IV.4. Measurement Methodology

The principle of the technique proposed here lays on the different coherent properties of the signal and the noise for different scenarios. The optical noise, which origin is based on a spontaneous emission process, cannot interfere with itself and thus present no coherence. This means that there is no correlation between consecutive photons at any time. On the other hand, the signal is generated by a stable source that, within a limit, ensures the correlation between successive photons and thus enables interference phenomena.

When an optical signal is modulated with a repetitive pattern, for instance a series of bits, the spectral shape is the convolution of the laser spectra, ideally a narrow delta, with the modulation shape which in turn is the convolution of the comb and the pulse. The result is a spectrum with ideally zero value for several spectral components. This outcome is caused by the interference between successive bits, which has the same amplitude, but their phase differs according to the relative time distance. This temporal difference can set the phase of the different bits in such way, that they interfere destructively and several spectral

components cancel. In order to resolve these spectral gaps, where the signal presents no contribution, the optical spectra must be recovered with high enough resolution.

In live traffic scenarios, the signal can be considered as a random series of bits which PSD is shaped as a sinc as long as a large number of bits are considered. However, for a given spectral component its instantaneous power density fluctuates when a single finite stream of bits it's analyzed. The composition of the partial bit stream determines the values of the instantaneous PSD for the spectral components. By selecting a narrow filter and performing the analysis over a signal which contains a short repetitive pattern within the long random stream, we ensure that the instantaneous PSD at a certain time corresponds to the ideally repetitive comb which present zero value for several spectral components and thus reveals the PSD of the uncorrelated noise.

The width of the selected filter not only limits the achievable spectral resolution when filtering individual points, but also constrains the length of the transmitted pattern so the induced spectral gaps are not averaged. Narrower filtering also implies that the total power received in the detection competes with electrical noises and requires post processing time for noise reduction. Wider filters have opposite behavior and the registered power is greater, on the other hands, their spectral integration translates in the time domain as a reduced chance of detecting spectral gaps which spectral power density would drops to zero.

Our proposal is based on the observation and analysis of the instantaneous power spectral density of the signal and its variations. Right after the optical filter, the signal is detected, downconverted to the electrical domain and registered with an acquisition card. With the proper disposition of these elements, the main idea is to evaluate the different registered value of the filtered spectrum, for several points at different times and analyze their values and evolution over time. Based on the different behavior that signal presents, depending on the series of bits that is carrying, and its coherence, the idea is to observe the spectral density of the noise as constant values over which the signal spectral component varies among different values depending on the transmitted stream.

In fig. IV.7, it is depicted the employed set-up using the Stimulated Brillouin Scattering as the filtering technique.

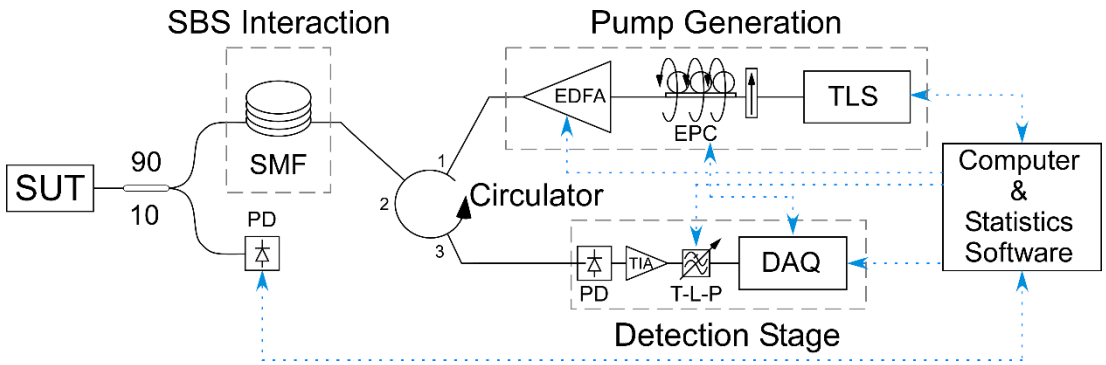

Figure IV.7. Schematics of the set-up necessary for the statics spectral analysis.

The signal under test is introduced in a reel of single mode fiber aided by an optical circulator in which the stimulated Brillouin scattering takes place. In one of the branches of the circulator, the high intensity SBS pump is coupled. Due to the interferometric origin of the Stimulated Brillouin Scattering, the relative polarization between signal under test and stimulus must be controlled and thus, the use of a polarization controller is needed. In the detection end, the signal was detected with a photodiode with a transimpedance stage, and then the electric signal was registered with a Data Acquisition Card. The recovered signal was then processed and analyzed with a computer. Parallel to the amplified signal detected, a 1% of the original signal was split and detected with another photodiode so the direct contribution of the SUT could be estimated and subtracted from the final signal. In order to filter spurious noise in the signal a tunable electrical filter was developed and integrated previous to the data acquisition card.

A schematic of the measurement procedure is depicted in fig. IV.8. In the first stage, the signal is analyzed with the SBS by using the standard set-up employed so far. However, in this case, we do not sweep the central emission of the pump laser, so the analysis can be performed over one narrow spectral region. Due to the nature of the Brillouin scattering, the sweeping mode and the static analysis present some differences such as the spontaneous Brillouin contribution when the amplification takes place [Govind P. '06b]. For that reason, special care must be taken with the calibrations and several routines where included where the signal and the EDFA where blocked to register their independent contribution.

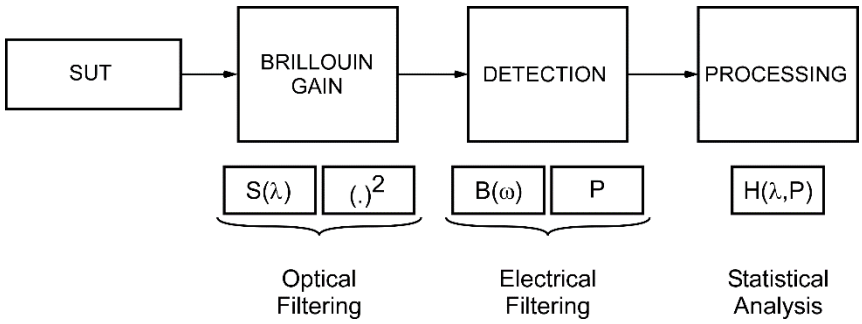

Figure IV.8. Conceptual Schematic of the proposed system for the statistical analysis of the different spectral regions.

In the second section the electrical filtering is done, due to non-static nature of the signal that we are analyzing, the detection stage was modified and a variable width electrical filter was placed after the photodetector in order to perform a selectable filtering of the detected signal. With a wide electrical filter, high frequency noises of electrical nature influence the final performance of the system, while narrow filters average the detected signal and reduce the possible range of detected values. The selectable width of the filter was set according to the requirements of the scenario ranging from 33kHz to 150kHz. After the detection, the signal was acquired with a DAQ sampling at 1.25MSa/s.

In the final stage the statistics of the registered signal is performed. In most of the cases a sample of 100.000 values was taken and the histogram was done according to the registered maximum and minimum values.

In the previous section it has been explained, the effect of the different coherence for signal and noise. It has been shown the different effect depending on the length of the pattern for long and short cases. In real scenarios, neither of these cases would be applicable. Usually, real traffic signals follow standardized protocols to transfer multiple bit streams synchronously. In this protocols the data for transportation, referred as payload, is divided in packages and multiplexed with headers, referred as overhead, that contain information about the transmission characteristics, e.g. destination, origin, size, etc…, according to the protocol. The final effect is the generation of repetitive short patterns interleaved with more complex data, as we can see in figure IV.9. This yields to a non-static value for the instantaneous power spectral density of the signal. The noise, on the other hand, present a flat spectrum.

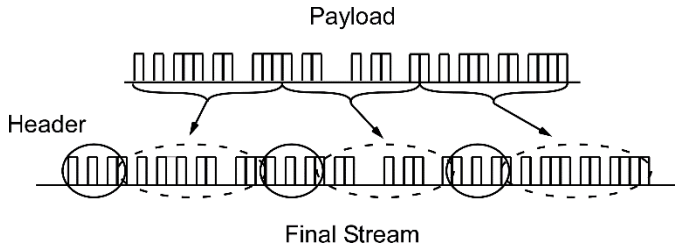

Figure IV.9. Schematic of the bit stream construction

In fig. IV.10, we can see a depiction of the commented effect. As the bit stream is changing, the different partial sections of the stream are analyzed when lying in the effective area of the filter. On the right, we can see the instantaneous spectra that would be reordered at each situations

Based on the value and the dynamic of the power spectral density registered for the different components of the spectra, we aim to evaluate the ratio of noise and signal for different scenarios. In order to corroborate our hypothesis we evaluate first the different scenarios stated in the regulations.

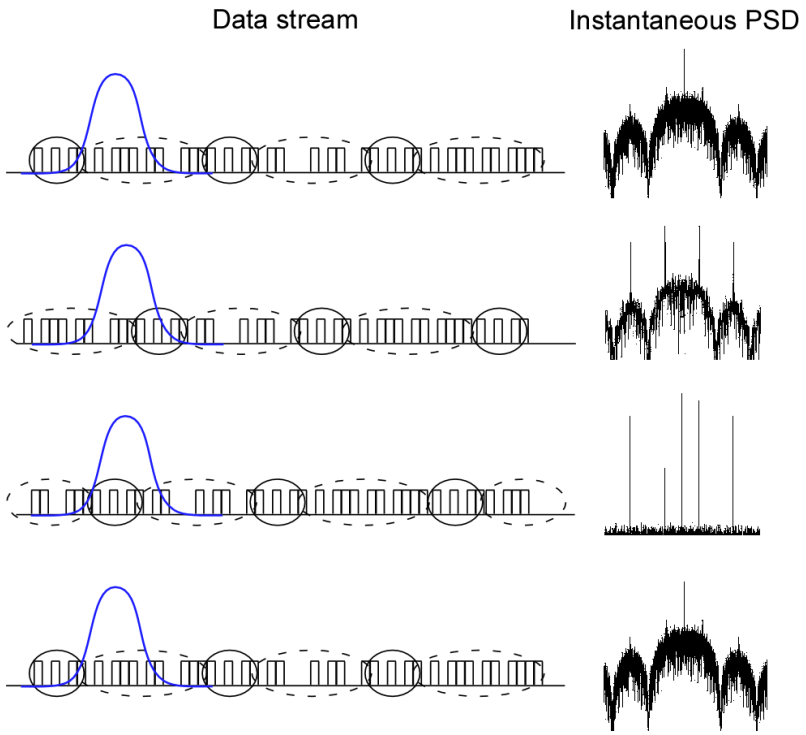

Figure IV.10. Different instantaneous PSD for a traffic carrying signal with headers at different times.

IV.5. PSD Characterization

IV.5.1. Modulated Signal characterization

The first tests were carried out to characterize the different features present in the signals for different scenarios. Following the schematics presented in fig. IV.8, two different framing structure where analyzed. These two structures differ in the length of the transmitted payload, which corresponds to the most random part of the bit stream, and thus present more or less repetitive headers that introduces periodicity.

The signal under test is generated by a high-performance optical network analyzer, designed to evaluate the performance of complex networks for different communications protocols. This equipment integrates the generation and detection stages both in the electrical domain. Using external modulators and detectors connected to the network under test, the system measures the BER for different scenarios and evaluates the actual performance of the system. With the proper set-up, this system has been used in the past in our research group to assess the health of complex optical networks. This particular model, Anritsu MP1577A, allows the generation of the two main protocols, so far, in Europe and USA for optical networks. In the generation stage, several parameters enable a full control of the different characteristics that the standard leaves for diverse configurations. In fig. IV.11, we show the different mappings available in the aforementioned analyzer. For the sake of simplicity, we have selected just two different cases according to their respective payload to overhead ratio.

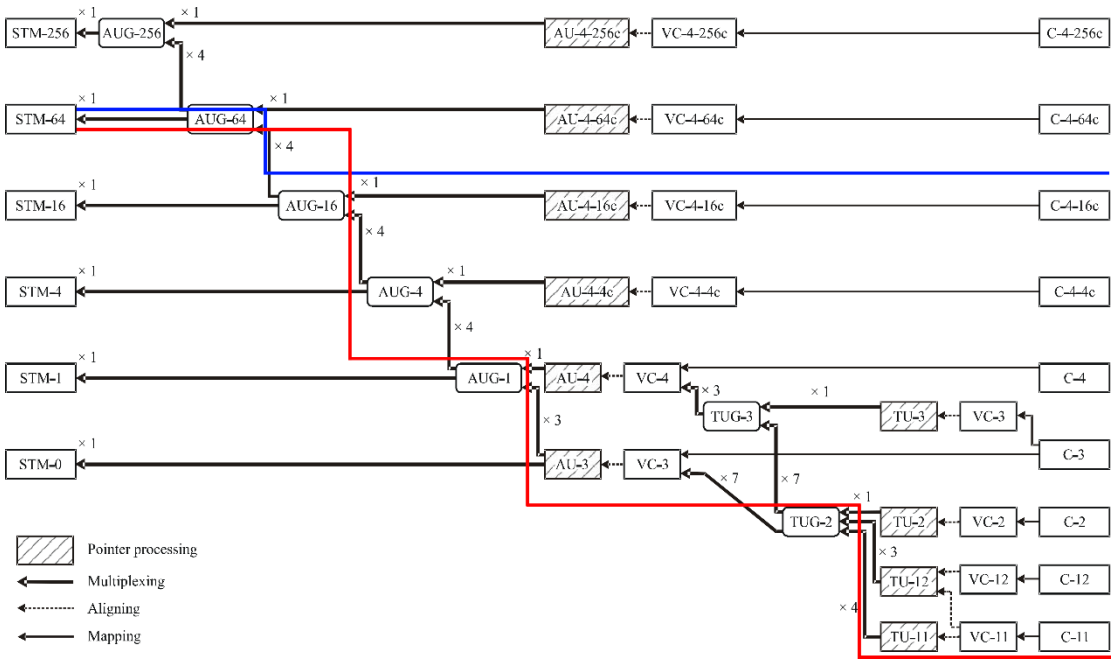

Figure IV.11. Multiplexing structure

The laser employed for the detection stage is an external cavity tunable laser. In contrast to what we needed for previous uses, here the laser is intended to keep its central wavelength as static as possible, rather than sweeping continuously. However, the use of a tunable spectral filtering enables the opportunity to analyze diverse spectral components where the intrinsic signal to noise ratio has different values. Those spectral points close to the clock frequencies have relative OSNR lower than the spectral point close to the optical carrier frequency and therefore higher noise contribution.

The first case was selected from the BER analyzer in order to have a high repeatability, which correspond to the mapping selected in the red line in fig. IV.11.

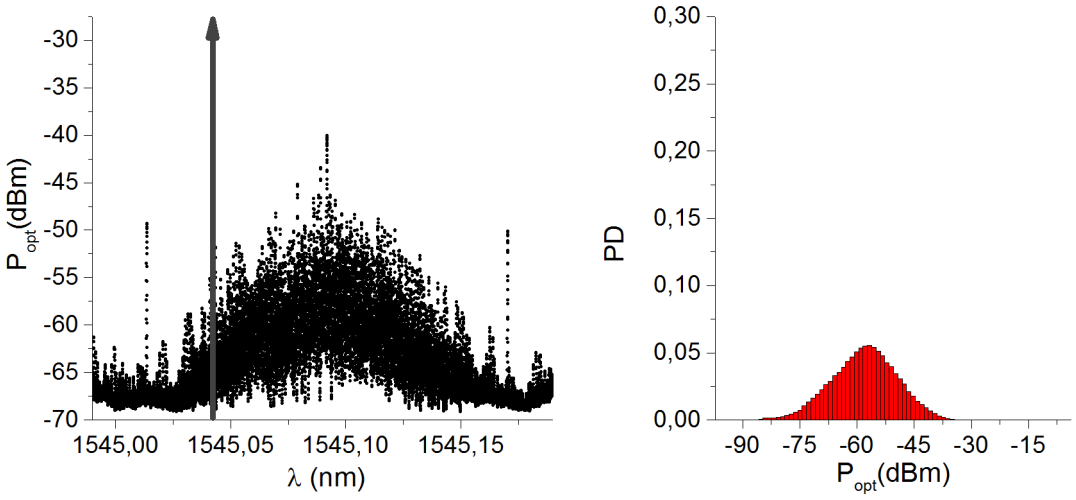

Figure IV.12. Spectrum and statistical analysis of a signal multiplexing according to case A (red).

What we can see in the left image, in figure IV.12, is the recovered instantaneous optical spectrum. In the right, we can see the histograms of the PSD for a certain spectral component marked in the image on the left. We can see that for a short time the registered valued have changed along a wide range of values.

In the second scenario, the stream was set so the repeatability was lower than in the previous case, which correspond to the blue line in fig. IV.11. The registered spectrum and histogram are depicted in figure IV.13.

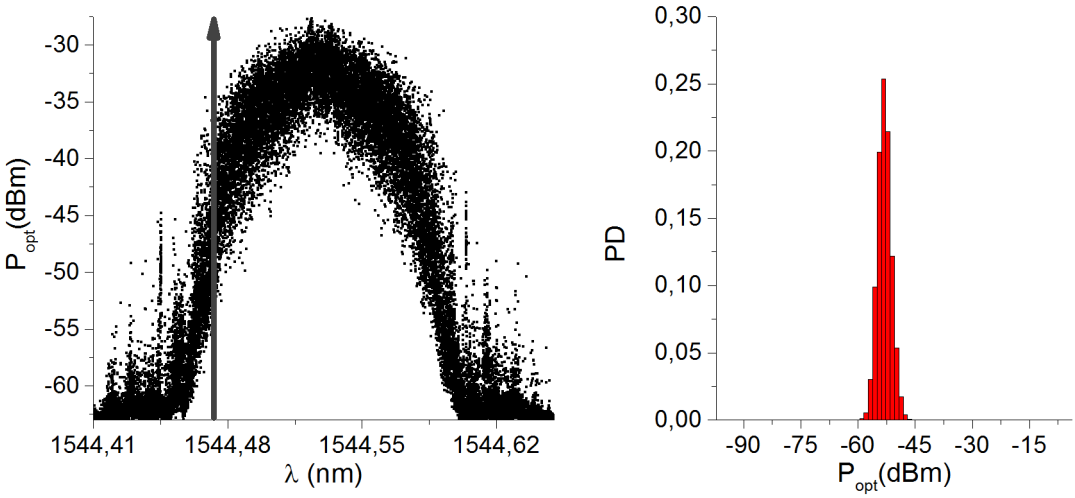

Figure IV.13. Spectra and statistical analysis of a signal multiplexing according to case B (blue).

In this case, we see in the spectrum on the left far less range of variations of power across its bandwidth. The difference can be seen in the histogram shape for both cases. Traffic structure with high enough repeatability depicts a wide distribution of values around a mean value, while in more random data the recovered spectra with this optical filtering does not reveal any dynamic for the PSD of the analyzed spectral component.

The distribution also depends on the spectral component. As the system filters in a 10Mhz band, the influence of the noise is more noticeable in those regions where its ratio with respect to the noise is higher. Thus, those spectral components near the clock frequency, i.e. ($1/T_b$) show a statistical behavior more influenced by the noise. Following this lead, the system must be flexible enough to select different wavelengths to analyze their dynamic. At the end, by performing an analysis over a discrete number of spectral components the dynamic of the whole system can be recovered.

In figure IV.14, we can a see the different shape of different spectral components for a signal coupled with a -45dBm ASE, measured with 10Mhz resolution.

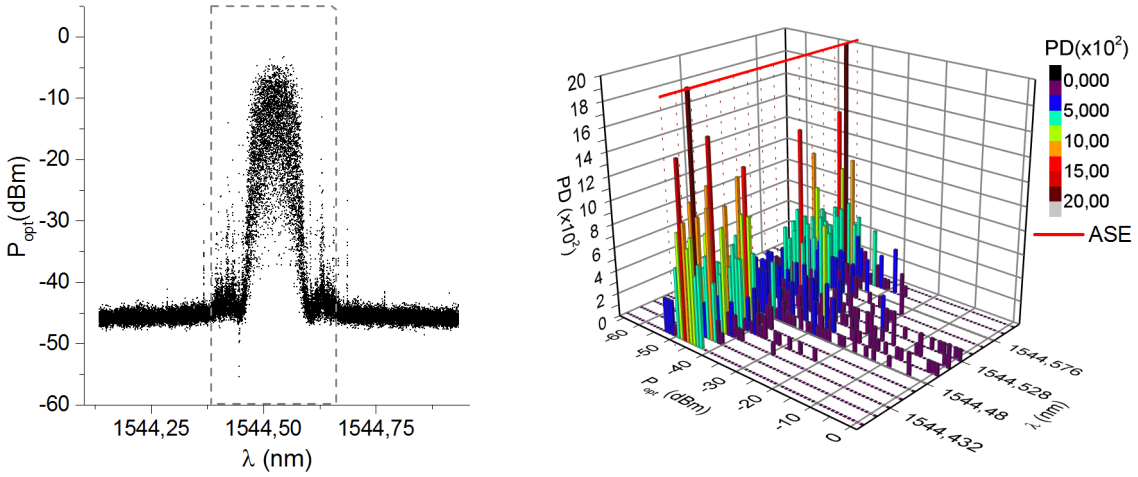

Figure IV.14. Spectrum and statistical analysis of a channel with underlying noise for different spectral components.

IV.5.2. Noise Characterization

In order to distinguish between noise components and signal they must show different dynamic. As mentioned above, the dynamic of the noise spectral density is expected to remain constant.

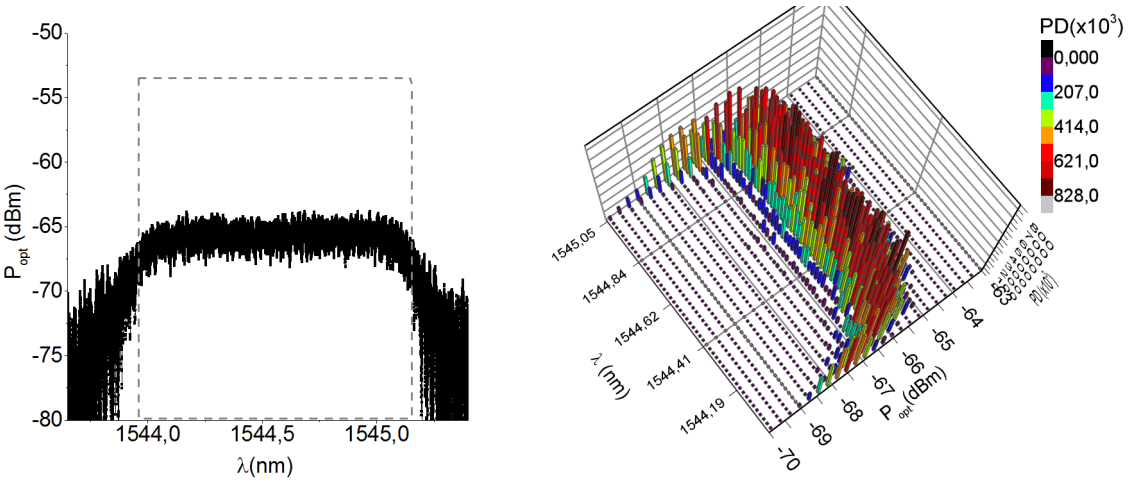

Figure IV.15. Spectra and statistical analysis of a channel with underlying noise for different spectral components.

Figure IV.15 shows that, there is no difference for the spectral components analyzed across the spectral bandwidth and the behavior for all of them is similar. In this case, the range of values for any spectral point, i.e. the width of the distribution at any point, is related to electrical and detection noise and thus only proportional to the optical level.

IV.5.3. Active Channel

The aim now is to have a first look at a signal with underlying noise, for that purpose an active channel is reproduced by coupling white additive noise to the live signal generated by the BER analyzer. In the case depicted in fig. IV.16 we have set and EDFA running with no feed signal and thus it outputs the fluorescence of the erbium across the C-Band. The

output of the EDFA was controlled with a variable optical attenuator (VOA) placed right before its output. Prior to the detection and for the sake of the equipment's safety, a 150GHz Fabry-Perot filter was placed in order to avoid high power income.

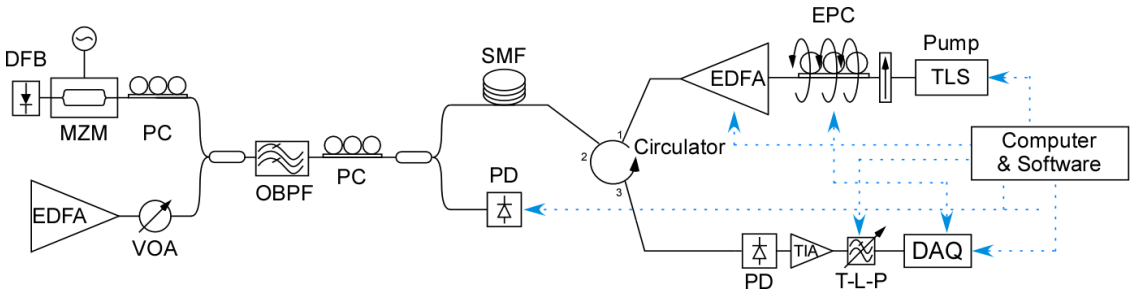

Figure IV.16. Schematics for the generation and analysis of the reference values

Fig IV.17 shows the depicted spectra for the active channel after averaging several spectra, the registered signal when the EDFA is switched off and the registered noise when the signal is switched off. In this figure, it can be seen that there are spectral region which do not present significant variations when the noise is present or not, in these spectral regions the PSD of the signal is predominant and its level is barely altered by the noise. On the other hand there can be easily identified spectral point hardly affected by the noise contribution.

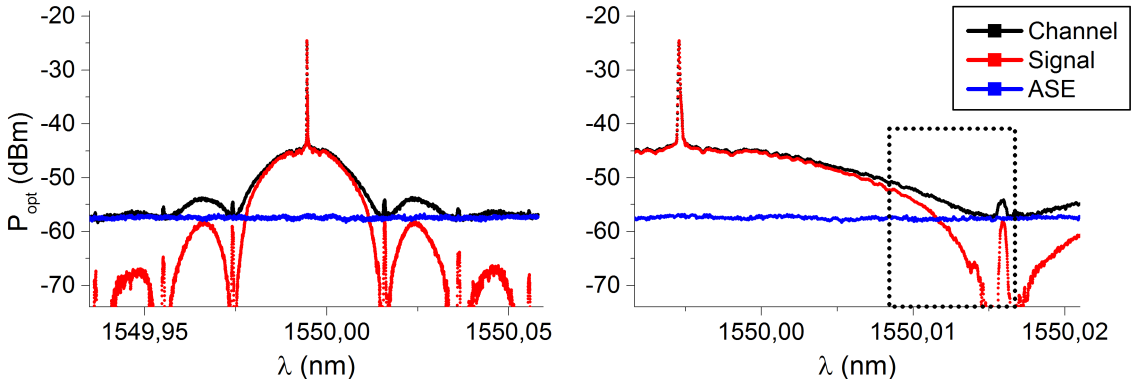

Figure IV.17. Spectra showing the relative values of OSNR that can be found across a modulated signal.

Attending to the behavior explained before, the system is analyzed for different spectral components. In order to do so, the TLS is now set to tune its wavelength so the aimed component can be analyzed. By keeping its central emission wavelength constant and registering the detected values over a period of time, the statistical analysis is performed.

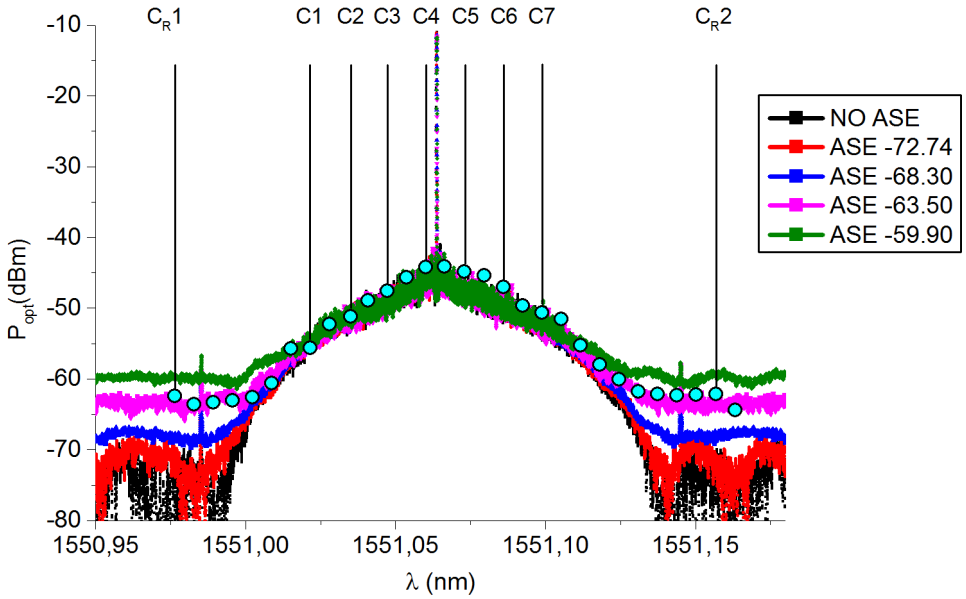

Figure IV.18. Optical spectra for different levels of ASE. The different spectral components selected for the statistical analysis are marked and labeled.

In fig IV.18, we can see the averaged spectra registered for different levels of OSNR, attending to these spectra we have chosen several points in which the analysis is going to be performed. The selected points for the analysis are marked and labeled in figure IV.18. The PSD exhibits different shape for the different components. As is expected, those spectral components where the signal-noise ratio is lower than others share some characteristics. In figure IV.19, it can be seen the different shape for the different components and its different levels of noise. From the depicted behavior, we can conclude that the shape of the distribution is related to the noise level at least up to certain value of the signal.

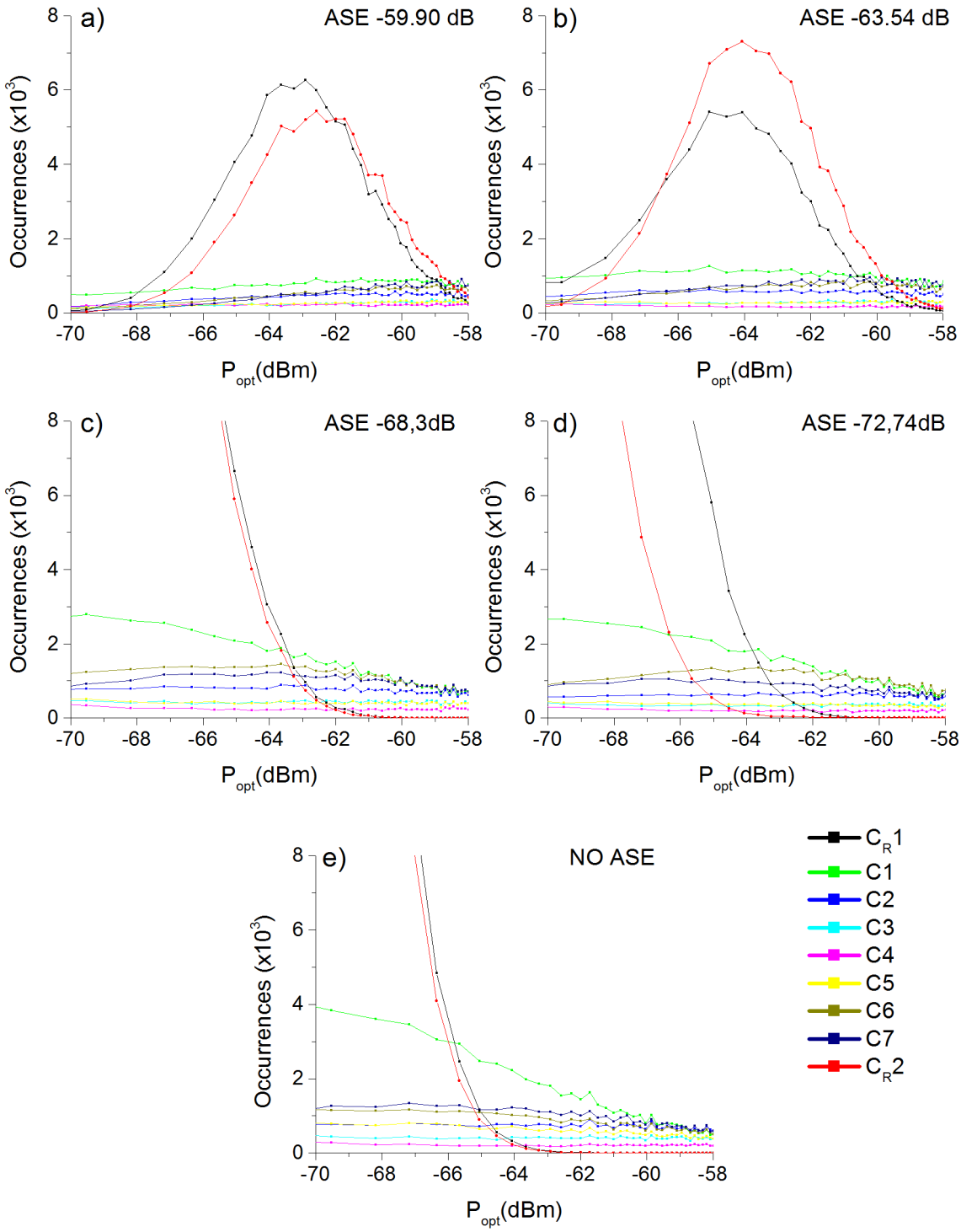

Figure IV.19. Statistical analysis of the different spectral components for different levels of ASE

Giving the shape of the different histograms for the different ASE levels, bounding the value of the noise from these measurements seems feasible but no methodology has been studied, so far. Based on our experience in previous statistical analysis in other phenomena, and after discarding other techniques, we concluded that the best way to address the problem was to the estimate the value of the noise from the calculated histograms of the measured

instantaneous power spectra. By comparing the histograms with values generated from the simulated scenarios in which noise and signal can be generated, we can change the values of the scenarios so we can bound and extract the value of the noise when the simulated and measured histogram of the PSD match. In order to perform a realistic simulation, we must synthesize first the different component and establish their correct interaction.

IV.6. Simulation and synthesis.

IV.6.1. Signal Bit stream construction.

As the final goal is to monitor live stream channels, the research is focused on simulating the most common structure data, which is based on the ITU-T G.707/Y.1322 recommendation, the synchronous digital hierarchy (SDH). The SDH was conceived as a flexible protocol and thus, it can be composed by multiple arrangement of substructures which payload data ratio can fluctuate. The structure of several SDH configuration was simulated according to the ITU specifications and later, with the help of a Pulse Pattern Generator and a Mach Zhender Modulator, were analyzed in the spectral domain.

The simplest structure for the data transmission in this protocol is the Synchronous Transport Module (STM). This frame structure in SDH has the peculiarity that the transmission rather than be sequential for the frame, i.e. the overhead is transmitted first and then the payload, it interleaves the overhead and the payload. This means that the whole payload is not transmitted at once but it is split in multiple parts and sent with different parts of the overhead.

One of the multiple advantages of this protocol is that it can be used to encapsulate earlier digital transmission standards. This simple frame structure can be made of smaller frames with their own payload and overheads, this leads to a decrease of the number of bits that can be considered live information. As the number of concatenated elements increases, the final bit stream exhibits a lower level of randomness and the number of short sequences of repetitive patterns increases.

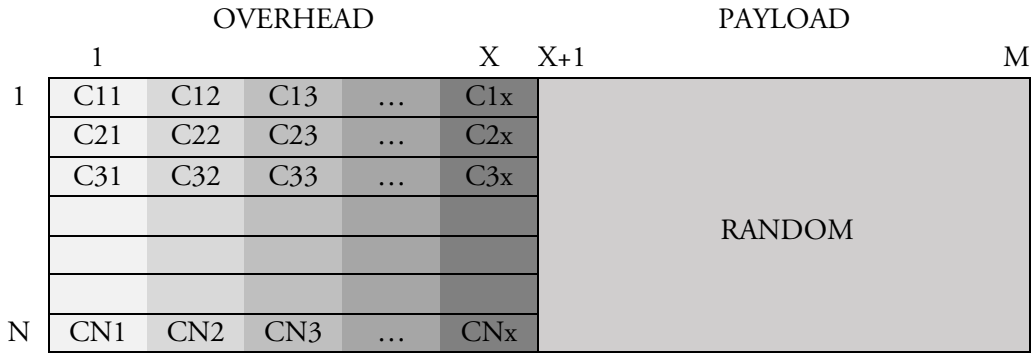

Figure IV.20. Schematics of the frame construction.

In order to simulate the behavior of real traffic, we designed several routines to generate different streams of bits. These routines were programmed with Matlab, in all of

them the construction of the different sub-part of the frames was programmed according to the regulations. The regulation states all the different formats and structure that all the sub-systems must follow. For the payload, we also employed standard pseudorandom bit generation sequences (PRBS) to fill the ultimate containers as the regulation points.

Figure IV.20 shows a conceptual diagram of the construction of a general STM. Due to the flexibility of the SDH the payload can be made up of sub STM with their own structure which corresponds to other networks. Finally, the stream is serialized row after row. All the steps were synthesized and the output of the simulation routines corresponds to the serialized stream of bits to be transmitted. This implies that not only the system concatenated the desired number of sub-frames with the requested payload, but also sorted them according to the designated order. The stream was saved in a standard file and uploaded into a pulse pattern generator (PPG), precisely Anritsu MP1800.

Here In fig IV.21, it is depicted the recovered spectra for three different cases synthesized for three different scenarios according to different level of concatenations. These scenarios differ in the ratio of overhead to payload information in the frame. The ratio decreases from the left figure to the right, where the ratio was set to the minimum possible according to the regulations.

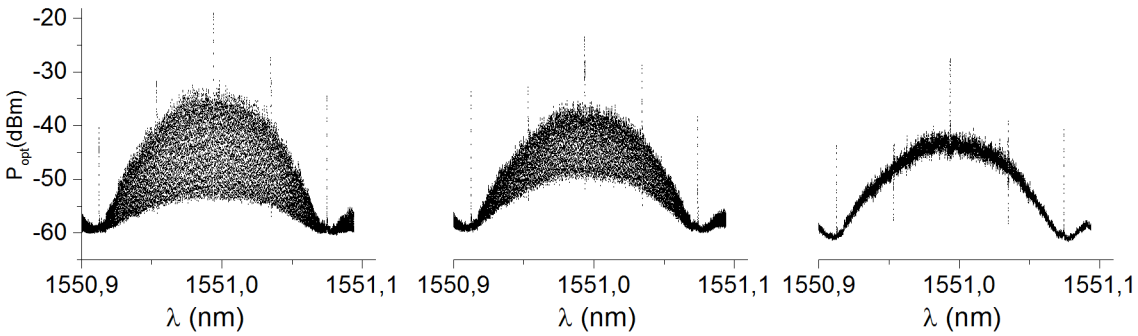

Figure IV.21. Spectra for the different cases generated based in the regulation.

It can be clearly seen how the ratio plays an important role in the PSD . As it was shown with the commercial BER tester, the level of randomness present in the stream limits the spectral resolution needed for the resolution.

In order to assess the synthesis method, we generated with our routines the same multiplexing structure generated by the BER tester and compared the results. Precisely we used the STM64-AUG64-AUG16-AUG4-AUG1-AU3-VC3-TUG2-TU11-VC11-C11. The results are depicted in fig. IV.22.

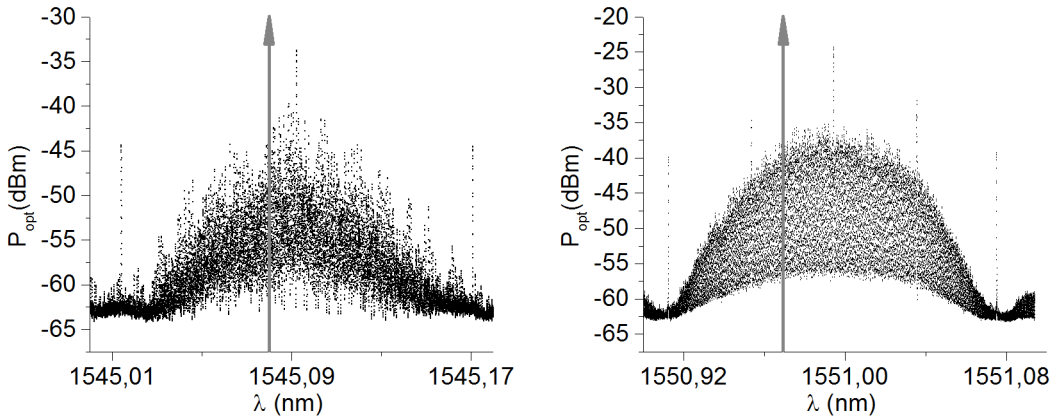

Figure IV.22. Comparison between spectra of the stream generated with the standard BER analyzer and the spectra of the synthesized signal.

There, it can be seen that both the synthesized bit stream and the standardized one share some spectral properties. Figure IV.23 plots the histogram of the optical values for a precise spectral region, marked in figure IV.22 with and arrow; for a series of instantaneous PSD measured for the signal generated by the BER, and the histograms of the values for synthesized scenarios.

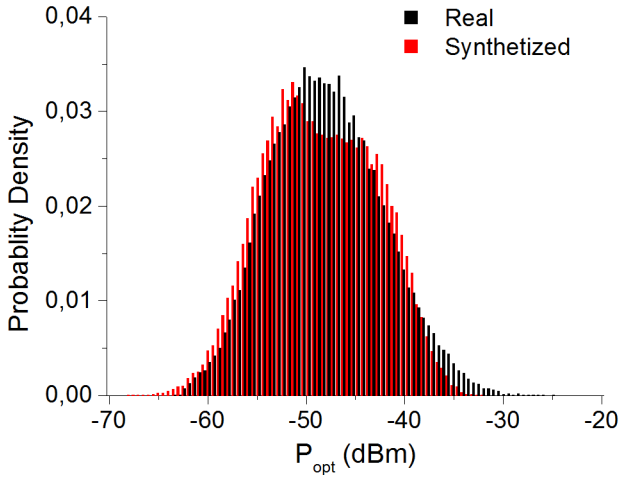

Figure IV.23. Histograms of the optical values of a spectral component for a synthesized signal compared with that obtained from the measured PSD of one of the SDH scenarios.

In the figure IV.23 we can see that the synthesized scenario can be used to simulate the behavior of the system. Based on the synthesized structure that we can achieve we will study now how the noise and signal component can be separated attending to their characteristics.

IV.6.2. Noise

The simulation of the emitted noise was performed assuming the most common case, which corresponds to a constant PSD along the amplification band of an EDFA. The most employed model for the noise modelling consist of a range of values distributed along the EDFA amplification band and a random distribution of the phase value for each generated

photon. [Agrawal '05]. The histograms for the real case of an EDFA without input signal and the simulated one are compared in figure IV.24.

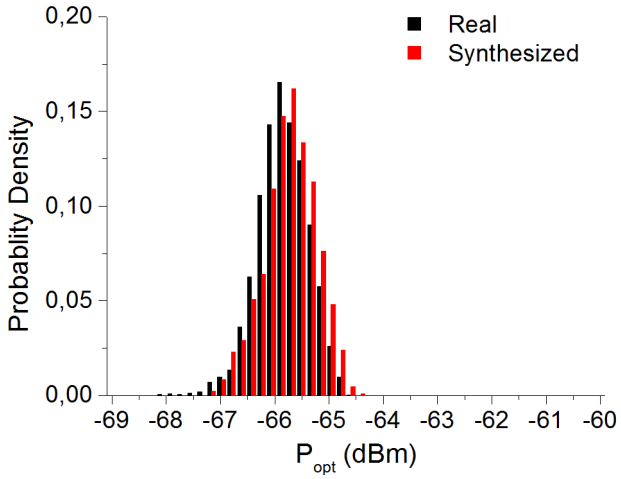

Figure IV.24. Histograms of the optical values of a spectral component for a synthesized noise compared with that obtained from the measured PSD of an EDFA wihtout input signal.

IV.6.3. Channel

In the model, both component were coherently superposed and the statistical analysis was performed over a high number of samples. In fig. IV.25, it can be seen the resulting histogram analysis for different values of the header payload ratio.

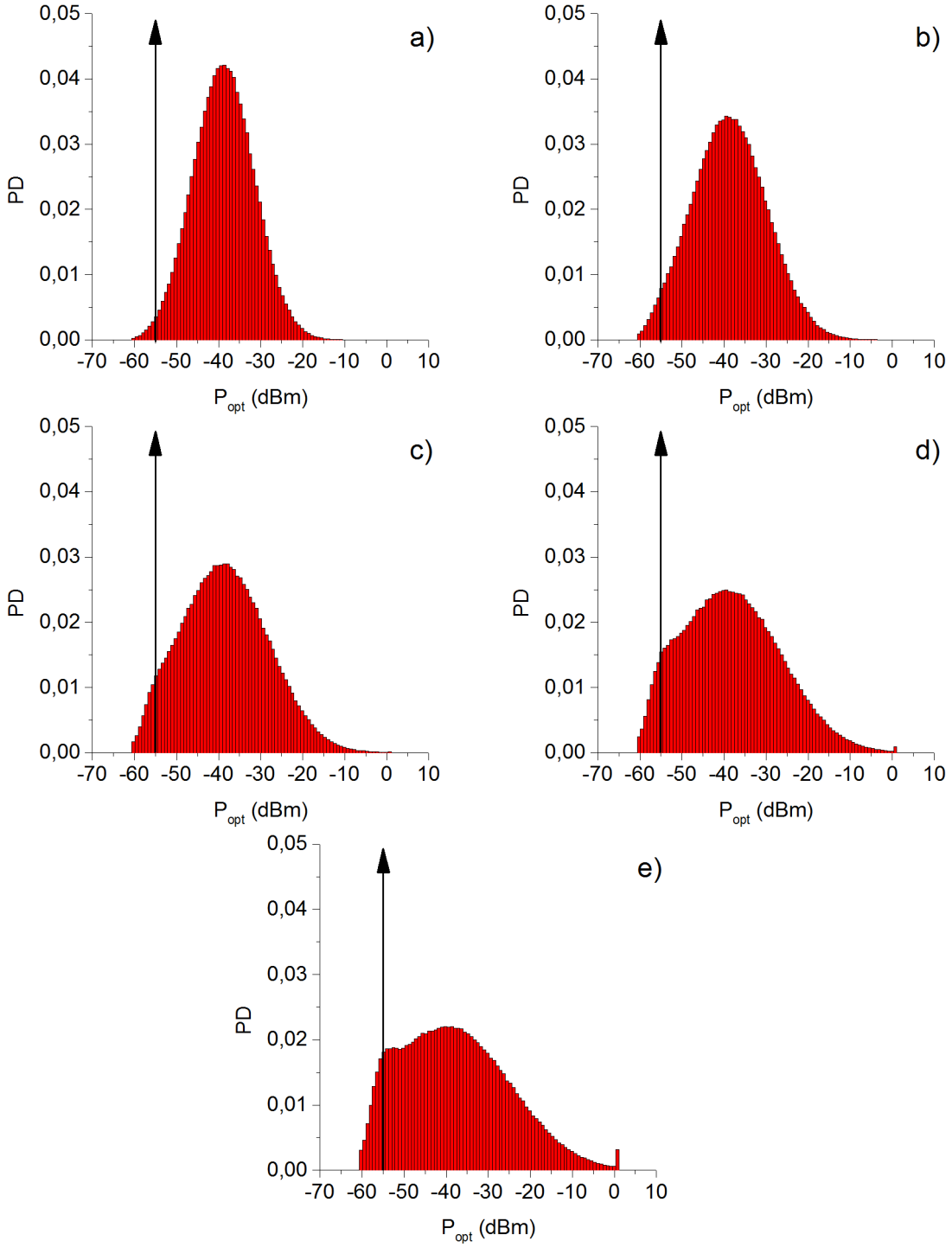

Figure IV.25. Statistical analysis of the resulting interaction between noise and synthesized signal for different ratios between overhead and payload.

Here we can see how this ratio will change the final shape of the statistical distribution. We can see that when the distribution is wide enough, i.e. there are repetitive patterns in the stream, the distributions is altered and the number of occurrences of a certain value increases far more than the others. In the graphs, we can see the shape of the distribution, the prominent lumps arising in the low region and it is depicted the value of

the underling noise. So far, we focus just on the spectral features that we can see for the same OSNR value and the different structure of the signal.

We have seen how the periodicity of the signal affects the shape of the recovered histogram which eases or worsens the effect of the noise in the signal. In the next test we will check how the shape of the histograms is affected by the level of the ASE. In fig. IV.26, it is depicted histograms for a wide distribution signal with different levels of ASE.

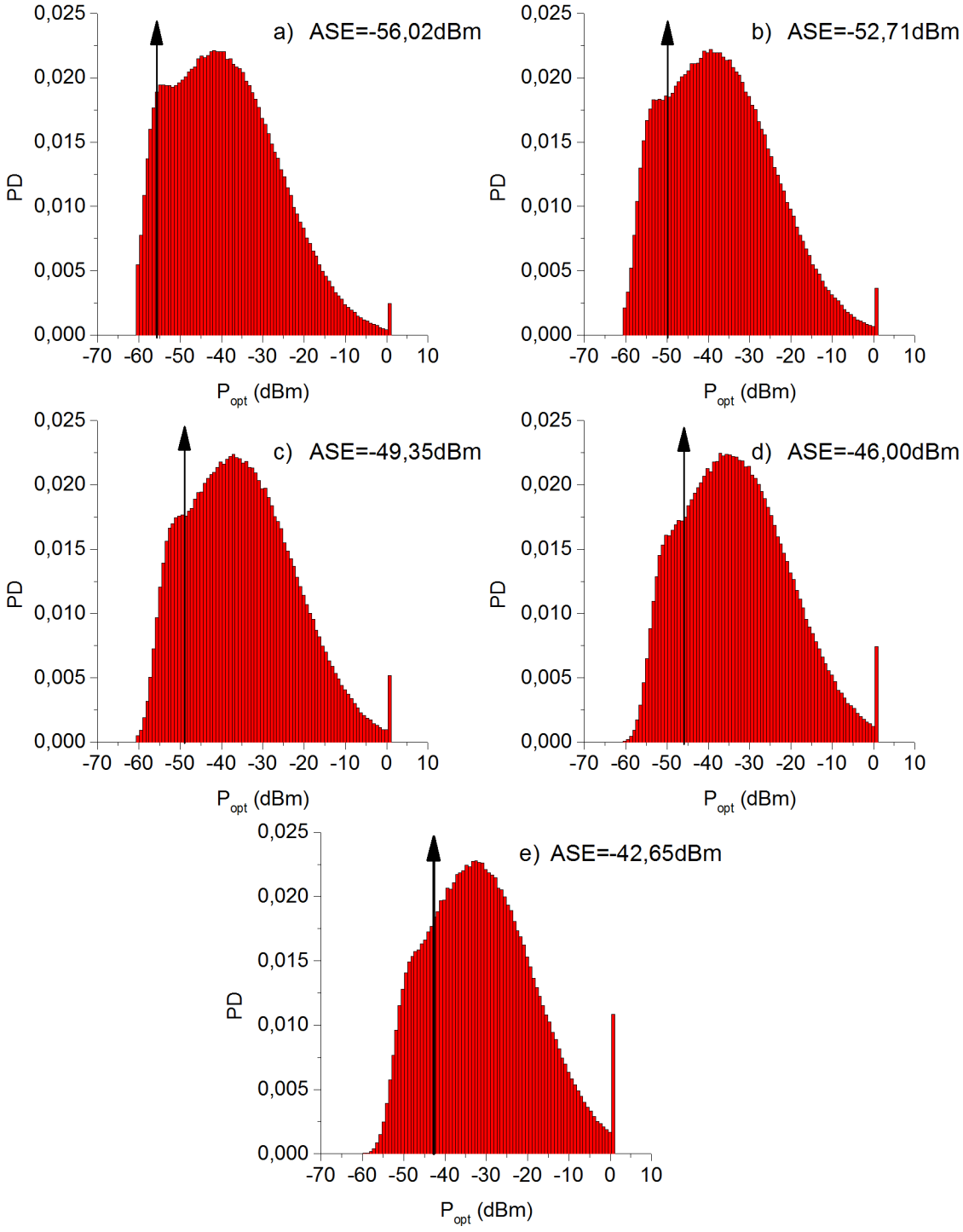

Figure IV.26. Statistical analysis of the resulting interaction between noise and synthesized signal for different ASE levels. The represented values were measured with a 10 MHz resolution.

We can see that the different levels of the ASE alters the shape of the distribution. In the cases with low ASE can see how the distortion present in the distribution matches the center of the ASE level, but for higher values the distortion does not seem to follow the center value of the ASE. Although there are noticeable difference between the shape of the distributions which suggest that from the altered shape, the value of the noise could be extracted or at least bounded.

IV.6.4. Model and data fitting

Based on the characterized distribution of the signal and the noise, we can now simulate the final effect of the different values for these parameters and evaluate the expected result in the measurement. By doing it in the inverse order, we can estimate the values of the different parameters by trying to fit the measured result with the output model of our simulation where we can modify the mean value of the noise and signal.

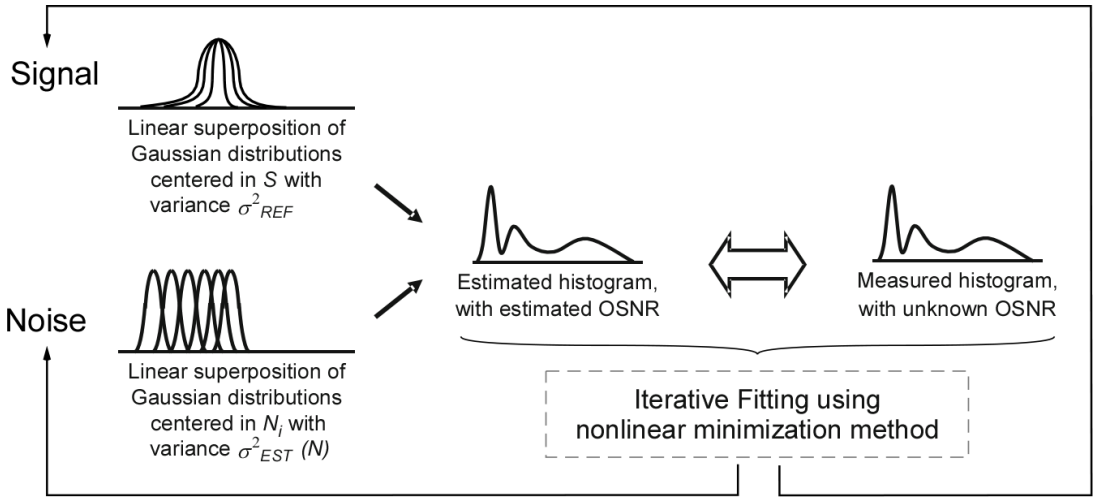

Figure IV.27. Schematics of the generation and fitting of the different parameters for noise and signal.

To do so we first start from initial parameters, generate the expected distribution for the signal and noise. Then, we analyze the outcome distribution and try to fit to the measured values. The sum of the quadratic residual of every point, referred as the residual sum of squares (RSS), will be used to compare the different fittings. In the next step, a slightly different parameter is used to generate the same process and the RSS between them is compare. Based on their difference, and the change introduced in the parameters, the systems outcomes the final values for the different parameters changed in the fitting until the optimum fit with the lowest RSS is achieved.

For the sake of simplicity, we will only show a few cases of the whole range of measurements taken for the different scenarios. As we faced an enormous range of measurements we decided to modify the system to program an automatic fit in the live signal. For that purpose, we prepared new routines to implement in the system. As the whole measurement equipment was controlled by a PC motherboard with a commercial processor and memory, we decided to implement the control of the subsystems via Matlab software.

Supported by the pre-installed drivers in the software, we could manage the acquisition and control of the measurement set-up.

The acquisition was performed by the same software and later in the same task the data were fitted. To do so the system controlled the TLS, set the central wavelength. After that, the signal from the detector was acquired at the maximum rate for a short period of time and saved as an array in the workspace. The software worked out the statistical analysis of the data, and proceeded to the fitting. Based on a standard minimum search algorithm, the software output the parameters that present the lowest residuals with respect to the measured data.

In figure IV.28, the systems present the statistical analysis of the registered values for different ASE levels.

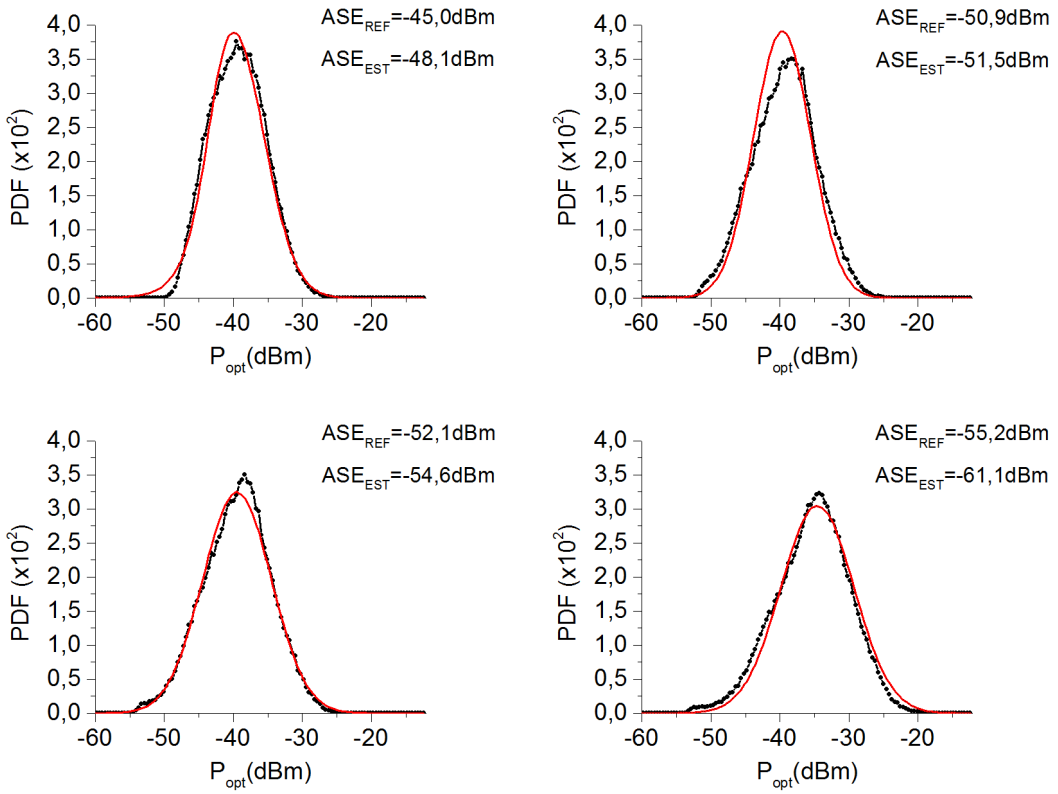

Figure IV.28. Measured data and fitting curve for different values of OSNR.

In figure IV.29, we show the mean different values obtained for the different scenarios studied.

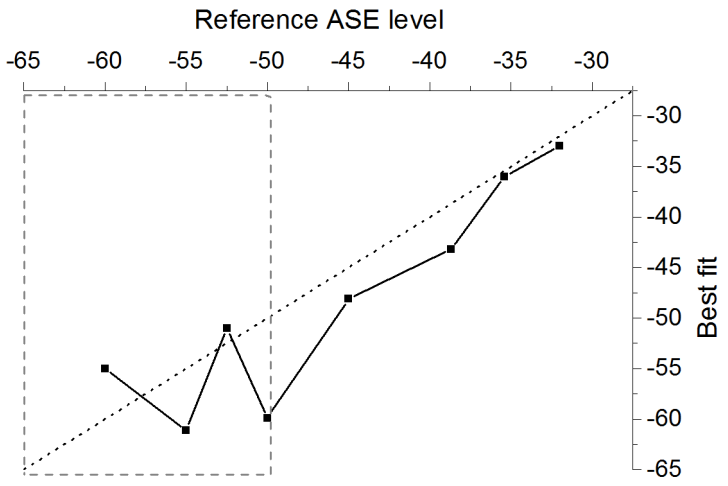

Figure IV.29. Obtained values and reference values showing the divergence for low values of ASE.

In the graph IV.29, it can be seen that for a certain range of values the system exhibits good results; however for low values of ASE it does not achieve acceptable results. For low ASE values, i.e. below -50dBm measured in a 10Mhz resolution, the systems final values deviated more than 5 dB from the reference values. Our first guess was a duplicity of minimum residual for different parameters or an inefficient minimum search algorithm that cannot get out of a local minimum. After analyzing the residual function for the values of the different parameters, we realized that even for the correct values the model could not reproduced the expected statistical behavior. So far, although it can be seen the different shape in the histograms for the different values, we have not been able to extract the real value of the underlying noise for low ASE values.

IV.7. Conclusions

In this chapter, we have studied the use of the ultra-high resolution spectroscopy to analyze the dynamic of the instantaneous power spectral density in live signals. We have focused the research in the use of stimulated Brillouin scattering and the analysis of 10MHz wide spectral regions. We also have centered the analysis in live signals following the ITU recommendations for SDH protocol.

Throughout the chapter the main goal has been the search and study of new techniques that could be employed in those scenarios were the polarization has been used for modulation too, i.e. PolMux. This polarization multiplexing impedes the use of the polarization selective techniques as, in times longer than the bit, the signal can be considered depolarized, like the noise. In our proposal, we studied and focused on one of the remaining physical properties that might be exploited for their differentiation, the coherence.

Our starting point was the assumption that due to their different source of origin the signal and the noise present different coherence. We tested how the length of the pattern and the resolution of the pattern affected the recovered optical spectrum of the signal. In the cases

where short patterns were introduced in the data stream, we were able to resolve spectral components, which PSD was zero and thus the power detected would correspond to other noise sources than the signal.

Based on the regulations, we studied the constraints imposed in the construction of the final data streams to be transmitted. We identified several cases in which the protocol established short pattern repetitions for management purposes. Aided by a commercial generator we studied the spectral shape of different mappings and multiplexing depending of the origin of the signal. Later on, we developed algorithm to synthesize the final stream according to the regulations and tested with a pulse pattern generator.

The technique developed after the study relies on the statistical analysis of the optical power from the instantaneous power spectra registered for different spectral components of the signal. We redesigned the optical spectrum analysis to switch the sweeping mode to a static registering of the instantaneous PSD for narrow spectral regions over a period of time. Based on the recovered optical spectrum of the signal, the system select suitable points to perform the statistical analysis of the registered power values. By sampling these spectral regions over a brief period of time, the statistical distribution of the registered power is calculated. The statistical analysis presents different features that respond to the values of the noise. The distortion when the noise was present or not and also its modification when the noise values increase or decrease corroborates the influence stated from the theoretical analysis.

With this information, we analyzed the influence of the noise and worked out a model of interaction between them. Based on the simulated model, we generate the expected histogram for a certain value of incoherent noise in the signal, and compare with the measured values. By controlling the simulation values, we expected to fit the two histograms and thus estimate the reference ASE value from the best fit. The main goal was to monitor the noise level from the value and shape of the registered histogram.

V. Conclusions

Throughout this thesis, novel approaches for the measurement of impairments in the optical domain have been studied. Due to the advantages that the analysis in the optical domain presents, compared to the analysis in the electrical domain; the research has been focused on the analysis and identification of the inherent limitations, that the common impairments present for its measurement with all-optical techniques.

Searching for higher spectral efficiency, the new modulation schemes have been designed to code the information using the different physical properties of the electromagnetic waves. We have studied how the conveying of these physical properties in the signal affects its differentiation with the optical noise when all-optical techniques are employed. We have also presented the new challenges that the current and future monitoring techniques must address in the next generation.

In order to assess the ultimate limitations of the analysis in the optical domain, we have employed the Stimulated Brillouin Scattering as the filtering technique to resolve the spectra. Due to its high resolution and its polarization selectivity the technique recovers most of the available information that can be extracted from the optical spectrum.

In the light of the results of the work carried out throughout this thesis, the main findings and conclusions can be summarized as follows:

- The use of U-DWDM and narrow filtering harshens the measurement of OSNR based on the identification of noise and signal in the optical spectrum. In these scenarios, the resolution of the filtering technique plays a major role and thorough analysis of the measurements must be done when ROADM are employed. The SBS filtering presents great performance in this scenario due to its high resolution, although this narrow filtering comes with a reduced sensitivity that limits the measureable PSD of the noise.

- The analysis of the impairments for multicarrier modulation formats schemes cannot be performed in the optical domain with the current regulations because they were designed for singles carrier schemes. For these schemes, the use of high resolution presents additional advantages as it can characterize the quality of the modulation based on the spectra recovered.

- SBS filtering can be used to achieve an individual characterization of the subcarriers involved in MCM schemes, such as the OFDM. We developed an algorithm in order to measure and isolate the optical power values of the different subcarriers present, with this data we analyzed the distortion in the reception and we found out a

relationship between these two parameters. Based on this defined SC-OSNR we managed to measure the individual performance of the different subcarriers. This characterization opens the possibility of designing schemes attending to the distortion of each sub-carrier, instead of a global averaged performance for the complete multicarrier modulation.

- When signal and noise share the same bandwidth in the spectrum, there may exist no points where the ASE can be measured. In these scenarios the different polarization properties of the noise and signal can be exploited for its differentiation. Taking advantage of the vectorial properties of the SBS, the OSNR can be resolved in-band by generating, in the signal, a selective and severe drift of the SOP of different spectral components. Without needing a polarizer and taking advantage of its high-resolution, the system can selectively suppress the signal contribution in several spectral components and reveal the underlying noise.

- By improving the polarization control of the pump in the SBS, a new method for the measurement of the SOP across the signal bandwidth has been developed. Based on the SBS spectral resolution and its polarization dependent gain we achieved a fully spectrally resolved polarimetry with the spectral resolution of the standard SBS. Without prior alignment or knowledge of the SUT, it can resolve the SOP for multiple signals in wide spans without losing the in-band resolution.

- Polarization can be used to differentiate noise and signal as long as it is not Pol-MUX. However, the depolarization nature associated with the noise can be misunderstood with the depolarization phenomena associated with PMD or non-linear effects in polarized signals. In these cases, an ordinary measurement of the degree of the polarization, or a simple projection over a linear polarizer proves to be insufficient, in order to distinguish between signal and noise according to their SOP. For these cases, the high-resolution spectrally-resolved polarimetry can obtain the full characterization of the SOP across the signal bandwidth. With this information, all the polarization impairments present in the signal can be quantified and classified according to its value and variations across the signal bandwidth.

- The polarization multiplexing schemes preclude the use of polarization nulling techniques. When the signal is modulated with two uncorrelated streams of data in two orthogonal polarization, the use of the polarization properties is no longer valid, as the outcome presents an effective depolarization, which resembles to the noise. For these cases, a novel technique is proposed. Based on the measurement of the instantaneous power spectra and its dynamic, the system can differentiate between the signal and noise components, due to the remaining correlation that exists in the modulated signal when following the communications standards. Although the measurements agree with the initial assumptions, we only succeeded in those cases

where the noise level was high and we could not measure significant values for a robust technique.

ANNEX A

References

Agrawal G.P. 2005. "Chapter 6. Optical Amplifier Noise". In *Lightwave Technology: Telecommunication Systems*. John Wiley & Sons.

Agrawal G.P. 2012. *Fiber-Optic Communication Systems*. John Wiley & Sons.

Baney D.M., B. Szafraniec, and A. Motamedi. 2002. "Coherent Optical Spectrum Analyzer". *Ieee Photonics Technology Letters* 14, no. 3 (March): 355–357.

Becker P.M., A.A. Olsson, and J.R. Simpson. 1999. *Erbium-Doped Fiber Amplifiers: Fundamentals and Technology*. Academic Press.

Bononi A., A. Vannucci, A. Orlandini, E. Corbel, S. Lanne, and S. Bigo. 2003. "Degree of Polarization Degradation due to Cross-Phase Modulation and Its Impact on Polarization-Mode Dispersion Compensators". *Journal of Lightwave Technology* 21, no. 9 (September): 1903–1913.

Buchali F., W. Baumert, H. Bulow, and J. Poirrier. 2002. "A 40 Gb/s Eye Monitor and Its Application to Adaptive PMD Compensation". In *Optical Fiber Communication Conference and Exhibit, 2002. OFC 2002*, 202–203.

Bülow H., and S. Lanne. 2004. "PMD Compensation Techniques". *Journal of Optical and Fiber Communications Reports* 1, no. 3 (November 1): 283–303.

Cai J.-X., M. Nissov, A.N. Pilipetskii, and N.S. Bergano. 2008. "Automatic PMD Compensation over Transoceanic Distance with Time Varying SOP, PSP, and PMD". In *Conference on Optical Fiber communication/National Fiber Optic Engineers Conference, 2008. OFC/NFOEC 2008*, 1–3.

Campos J.M., A. Destrez, J. Jacquet, and Z. Toffano. 2004. "Ultra-Fast Optical Spectrum Analyzer for DWDM Applications". *Ieee Transactions on Instrumentation and Measurement* 53, no. 1 (February): 124–129.

Chan C.C.K. 2010. *Optical Performance Monitoring: Advanced Techniques for Next-Generation Photonic Networks*. Burlington, MA: Academic Pr Inc.

Chang R.W. 1966. "Synthesis of Band-Limited Orthogonal Signals for Multichannel Data Transmission". *Bell System Technical Journal, The* 45, no. 10 (December): 1775–1796.

Choi H.Y., Y. Takushima, and Y.C. Chung. 2008. "OSNR Monitoring Technique for DPSK/DQPSK Signals Based on Self-Heterodyne Detection". *Ieee Photonics Technology Letters* 20, no. 13-16 (August): 1124–1126.

Collett E. 2005. *Field Guide to Polarization*. Bellingham, Wash: SPIE Publications.

Cornick K.E., S.D. Dods, M. Boroditsky, and P.M. Farrell. 2005. "All-Order PMD Penalty Prediction Using SOP String Lengths". In , 702–703.

Cornick K.E., K. Hinton, S.D. Dods, and P.M. Farrell. 2008. "A Framework for Evaluating the System Penalty From Polarization-Mode Dispersion Using Different Performance Monitoring Techniques". *Journal of Lightwave Technology* 26, no. 13 (July): 1790–1797.

Dahan D., U. Mahlab, A. Teixeira, I. Zacharopoulos, and I. Tomkos. 2011. "Optical Performance Monitoring for Translucent/transparent Optical Networks RID D-6304-2011". *Iet Optoelectronics* 5, no. 1 (February): 1–18.

Derickson D. 1997. *Fiber Optic Test and Measurement*. 1 edition. Upper Saddle River, N.J: Prentice Hall.

Van Deventer M.O., and A.J. Boot. 1994. "Polarization Properties of Stimulated Brillouin Scattering in Single-Mode Fibers". *Journal of Lightwave Technology* 12, no. 4 (April): 585–590.

Fabrega J.M., M.S. Moreolo, M. Chochol, and G. Junyent. 2013. "Impact of Modulator Driving on Constant Envelope Optical OFDM Based on Hartley Transform". *IEEE Photonics Technology Letters* 25, no. 6 (March): 598–601.

FERREIRA M.F., A.N. PINTO, P.S. ANDRÉ, N.J. MUGA, J.E. MACHADO, R.N. NOGUEIRA, S.V. LATAS, M.H. SOUSA, and J.F. ROCHA. 2005. "Polarization Mode Dispersion in High-Speed Optical Communication Systems". *Fiber and Integrated Optics* 24, no. 3-4 (May 1): 261–285.

Gordon J., and H. Kogelnik. 2000. "PMD Fundamentals: Polarization Mode Dispersion in Optical Fibers". *PROCEEDINGS OF THE NATIONAL ACADEMY OF SCIENCES OF THE UNITED STATES OF AMERICA* 97, no. 9 (April 25): 4541–4550.

Govind P. A. 2006a. *Nonlinear Fiber Optics*. Fourth. San Diego: Academic Press.

Govind P. A. 2006b. "Chapter 9 - Stimulated Brillouin Scattering". In *Nonlinear Fiber Optics (Fourth Edition)*, 329–367. San Diego: Academic Press.

Gumaste A., and T. Antony. 2003. *DWDM Network Designs and Engineering Solutions*. Cisco Press.

Heras C., J.M. Subias, J. Pelayo, and F. Villuendas. 2007. "Polarization Properties of Optical Spectral Components Generated by XPM Effect". *Journal of Lightwave Technology* 25, no. 5 (May): 1313–1321.

Hill G., P. Chidgey, F. Kaufhold, T. Lynch, O. Sahlen, M. Gustavsson, M. Janson, et al. 1993. "A Transport Network Layer Based on Optical Network Elements". *Journal of Lightwave Technology* 11, no. 5-6 (June): 667–679.

Hobbs P.C.D. 2011. *Building Electro-Optical Systems: Making It All Work*. John Wiley & Sons.

IEC. 1992. *IEC 61280-2-9:2009. Fibre Optic Communication Subsystem Test Procedures - Part 2-9: Digital Systems - Optical Signal-to-Noise Ratio Measurement for Dense Wavelength-Division Multiplexed Systems*.

ITU-T. 2004. *G.697 : Optical Monitoring for DWDM Systems*.

ITU-T. 2007. *G.650.2.Definitions and Test Methods for Statistical and Non-Linear Related Attributes of Single-Mode Fibre and Cable*.

ITU-T. 2012. *G.694.1 : Spectral Grids for WDM Applications: DWDM Frequency Grid*.

Jose Martinez J., A. Villafranca, C.D. Heras, M.I. Roche, J.M. Subias, J. Pelayo, E. Pellejer, P. Blasco, and J.I. Garces. 2010. "In-Band Optical Signal-to-Noise Ratio Monitoring Method Based on High-Resolution Polarization Analysis and Induced Differential Group Delay". *Applied Optics* 49, no. 32 (November 10): 6213–6216.

Kao K.C., and G.A. Hockham. 1966. "Dielectric-Fibre Surface Waveguides for Optical Frequencies". *Proceedings of the Institution of Electrical Engineers* 113, no. 7: 1151.

Keiser G. 2010. *Optical Fiber Communications*. 4 edition. New York, NY: McGraw-Hill Science/Engineering/Math.

Kilper D.C., S. Chandrasekhar, L. Buhl, A. Agarwal, and D. Maywar. 2002. "Spectral Monitoring of OSNR in High-Speed Networks". In *28th European Conference on Optical Communication, 2002. ECOC 2002*, 3:1–2.

Lachs G. 1998. *Fiber Optics Communications*. 1 edition. New York: McGraw-Hill Professional.

Lee J.H., D.K. Jung, C.H. Kim, and Y.C. Chung. 2001. "OSNR Monitoring Technique Using Polarization-Nulling Method". *Ieee Photonics Technology Letters* 13, no. 1 (January): 88–90.

Lee J.H., N. Yoshikane, T. Tsuritani, and T. Otani. 2008. "In-Band OSNR Monitoring Technique Based on Link-by-Link Estimation for Dynamic Transparent Optical Networks". *Journal of Lightwave Technology* 26, no. 9-12 (June): 1217–1225.

Liu X., Y.-H. Kao, S. Chandrasekhar, I. Kang, S. Cabot, and L.L. Buhl. 2007. "OSNR Monitoring Method for OOK and DPSK Based on Optical Delay Interferometer". *Ieee Photonics Technology Letters* 19, no. 13-16 (August): 1172–1174.

Luis R.S., A. Teixeira, and P. Monteiro. 2009. "Optical Signal-to-Noise Ratio Estimation Using Reference Asynchronous Histograms". *Journal of Lightwave Technology* 27, no. 5-8 (April): 731–743.

Luo T., C.Y. Yu, Z.Q. Pan, Y. Wang, Y. Arieli, and A.E. Willner. 2005. "Dispersive Effects Monitoring for RZ Data by Adding a Frequency-Shifted Carrier along the Orthogonal Polarization State". *Journal of Lightwave Technology* 23, no. 10 (October): 3295–3301.

MICIN. 2010. *TEC2010-17869 Monitorización de Las Prestaciones Ópticas de Redes de Nueva Generación.*

Moller L., and L. Buhl. 2001. "Method for PMD Vector Monitoring in Picosecond Pulse Transmission Systems". *JOURNAL OF LIGHTWAVE TECHNOLOGY* 19, no. 8 (August): 1125–1129.

National Semiconductor. 1980. "Power Spectra Estimation". Application Note 255. http://archive.org/details/bitsavers_nationalap_328213.

Nezam S.M.R., J.E. McGeehan, and A.E. Willner. 2004. "Theoretical and Experimental Analysis of the Dependence of a Signal's Degree of Polarization on the Optical-Data Spectrum". *Journal of Lightwave Technology* 22, no. 3 (March): 763–772.

Ohteru S., and N. Takachio. 1999. "Optical Signal Quality Monitor Using Direct Q-Factor Measurement". *IEEE Photonics Technology Letters* 11, no. 10 (October): 1307–1309.

Pelayo Z.F.J., E.R. Alonso, H.P. Blasco, G.J.I. Garces, V.C. Heras, T.F.M. Lopez, D.J. Subias, and Y.F. Villuendas. 2004. "Dispositivo Analizador de Espectros Opticos Por Difusion Brillouin Y Procedimiento de Medida Asociado".

Proakis J.G. 2001. *Digital Communications*. McGraw-Hill.

Rogers A. 2008. *Polarization in Optical Fibers*. Norwood, MA: Artech House.

Roudas I., G. Piech, M. Mlejnek, Y. Mauro, D. Chowdhury, and M. Vasilyev. 2004. "Coherent Frequency-Selective Polarimeter for Polarization-Mode Dispersion Monitoring". *JOURNAL OF LIGHTWAVE TECHNOLOGY* 22, no. 4 (April): 953–967.

Saleh A.A.M., and J.M. Simmons. 2006. "Evolution Toward the Next-Generation Core Optical Network". *Journal of Lightwave Technology* 24, no. 9 (September 3): 3303.

Schonfelder T., and DE. 2003. "United States Patent: 6580535 - Polarization Division Multiplexing in Optical Data Transmission Systems".

Sevillano P., J. Subias, Z. Pelayo, V. Heras, V. Villafranca, and T. Lopez. 2014. "System and Method for Measuring a Wavelength-Resolved State of Polarization of an Optical Signal".

Shake I., W. Takara, S. Kawanishi, and Y. Yamabayashi. 1998. "Optical Signal Quality Monitoring Method Based on Optical Sampling". *Electronics Letters* 34, no. 22 (October 29): 2152–2154.

Shieh W., and C. Athaudage. 2006. "Coherent Optical Orthogonal Frequency Division Multiplexing". *Electronics Letters* 42, no. 10 (May 11): 587–589.

Subías J., J. Pelayo, F. Villuendas, C. Heras, and E. Pellejer. 2005. "Very High Resolution Optical Spectrometry by Stimulated Brillouin Scattering". *Ieee Photonics Technology Letters* 17, no. 4 (April): 855–857.

Tomkos I., M. Angelou, R.J.D. Barroso, I. de Miguel, R.M.L. Toledo, D. Siracusa, E. Salvadori, A. Tymecki, Y. Ye, and I.T. Monroy. 2012. "Next Generation Flexible and Cognitive Heterogeneous Optical Networks". In *The Future Internet*, ed. F. Álvarez, F. Cleary, P. Daras, J. Domingue, A. Galis, A. Garcia, A. Gavras, et al., 225–236. Lecture Notes in Computer Science 7281. Springer Berlin Heidelberg.

Vandeventer M., C. Deblok, and C. Park. 1991. "High-Dynamic-Range Heterodyne Measurement of Optical-Spectra". *Optics Letters* 16, no. 9 (May 1): 678–680.

Villafranca A. 2008. "Development of Brillouin Optical Spectroscopy Techniques and Application to the Characterization of Optical Sources, Modulators and Communication Signals". Universidad de Zaragoza.

Villafranca A., J. Lasobras, J.A. Lazaro, and I. Garces. 2007. "Characterization of the Main Semiconductor Laser Static and Dynamic Working Parameters from CW Optical Spectrum Measurements". *Ieee Journal of Quantum Electronics* 43, no. 1 (February): 116–122.

Walker G., D. Spirit, D. Williams, and S. Davey. 1991. "Noise Performance of Distributed Fiber Amplifiers". *Electronics Letters* 27, no. 15 (July 18): 1390–1391.

Weinstein S., and P. Ebert. 1971. "Data Transmission by Frequency-Division Multiplexing Using the Discrete Fourier Transform". *IEEE Transactions on Communication Technology* 19, no. 5 (October): 628–634.

Wise A., M. Tur, and A. Zadok. 2011. "Sharp Tunable Optical Filters Based on the Polarization Attributes of Stimulated Brillouin Scattering". *Optics Express* 19, no. 22 (October 24): 21945–21955.

Xia T., G.A. Wellbrock, D.L. Peterson, F. Heismann, V. Lecoeuche, F. Sauron, and A. Champavère. 2012. "Field Trial of a Novel Non-Intrusive Method for In-Service PMD Measurements in Fiber-Optic Networks". In *National Fiber Optic Engineers Conference*, NTu2E.5. Optical Society of America.

Xia T., G. Wellbrock, D.L. Peterson, D.Z. Chen, H. Chen, G.W. Schinn, N. Cyr, S. Yao, X. Chen, and B. Zhang. 2011. "Field Trial of In-Service PMD Measurement Using Idle DWDM Channels in Operational Long Haul Network". In *National Fiber Optic Engineers Conference*, NWC4. Optical Society of America. http://www.opticsinfobase.org/abstract.cfm?URI=NFOEC-2011-NWC4.

Xu L., S.X. Wang, H. Miao, and A.M. Weiner. 2009. "Polarization Mode Dispersion Spectrum Measurement via High-Speed Wavelength-Parallel Polarimetry". *Applied Optics* 48, no. 24 (August 20): 4688–4697.

Yang J.-Y., L. Zhang, L.C. Christen, B. Zhang, S. Nuccio, X. Wu, L.-S. Yan, S. Yao, and A.E. Willner. 2007. "Chromatic-Dispersion-Insensitive PMD Monitoring of 20-Gb/s DQPSK and 10-Gb/s DPSK Using DGD-Generated Polarization-Based Interferometer Filter". In *2007 33rd European Conference and Ehxibition of Optical Communication (ECOC)*, 1–2.

Yao X.S., L. Yan, and Y. Shi. 2005. "Highly Repeatable All-Solid-State Polarization-State Generator". *Optics Letters* 30, no. 11 (June 1): 1324–1326.

Zadok A., E. Zilka, A. Eyal, L. Thevenaz, and M. Tur. 2008. "Vector Analysis of Stimulated Brillouin Scattering Amplification in Standard Single-Mode Fibers". *Optics Express* 16, no. 26 (December 22): 21692–21707.

ANNEX B

Auhtor's Publications

Publications derived from this thesis:

- Journals

P. Sevillano, J. M. Subias, A. Villafranca, and J. Pelayo, "In-Band DGD Monitoring Based on Polarization Controlled Stimulated Brillouin Scattering," *IEEE Photonics Technol. Lett.*, vol. 25, no. 16, pp. 1586–1588, Aug. 2013.

J. M. Fabrega, P. Sevillano, M. Svaluto Moreolo, A. Villafranca, F. J. Vílchez, and J. M. Subías, "OFDM subcarrier monitoring using high resolution optical spectrum analysis," *Optics Communications*, vol. 342, pp. 144–151, May 2015.

- Patents

P. Sevillano, J. Subias, Z. Pelayo, V. Heras, V. Villafranca, and T. Lopez, "System and Method for Measuring a Wavelength-Resolved State of Polarization of an Optical Signal," ES2441915 (A2) Abstract of corresponding document: US2013314706 (A1), 06-Feb-2014

- Conferences:

M. I. Roche, P. Sevillano, A. Villafranca, J. Subias, and I. Garces, "Estudio de nuevas técnicas de medida de OSNR in-band basadas en espectroscopía óptica de alta resolución," in *VII Reunión Española de Optoelectrónica, OPTOEL'11*, Santander, 2001.

J. M. Fabrega, P. Sevillano, M. Svaluto Moreolo, J. Jose Martinez, A. Villafranca, and J. Subias, "All-Optical In-Band OSNR Measurement in Intensity-Modulated Direct-Detection Optical OFDM Systems," *2013 15th International Conference on Transparent Optical Networks (ICTON 2013)*, 2013.

A. Villafranca, P. Sevillano, E. Pellejer, J. Pelayo, and J. Subias, "Novel Method for the Measurement of the Wavelength-Resolved High-Resolution Polarization State of Optical Signals and Application to the Monitoring of Communication Signals," *2013 15th International Conference on Transparent Optical Networks (ICTON 2013)*, 2013.

P. Sevillano, J. Subias, A. Villafranca, and J. Pelayo, "Medida de la dispersión del vector de polarización mediante difusión Brillouin estimulada," *VIII Reunión Española de Optoelectrónica, OPTOEL'13*, Alcalá de Henares, 2013.

P. Sevillano, A. Villafranca, J. Subias, J. Pelayo, and C. D. Heras, "Analysis of the Polarization Dependence of Non-Linear Effects using High-Resolution Spectrally-Resolved Polarimetry," *2014 16th International Conference on Transparent Optical Networks (ICTON 2014)*, 2014

Publications not directly related with the topic of the thesis topic but derived from the work performed through its developing.

P. Sevillano, J. Subias, C. Heras, J. Pelayo, and F. Villuendas, "Brillouin induced self-heterodyne technique for narrow line width measurement," *Opt. Express*, vol. 18, no. 14, pp. 15201–15206, Jul. 2010.

1586 IEEE PHOTONICS TECHNOLOGY LETTERS, VOL. 25, NO. 16, AUGUST 15, 2013

In-Band DGD Monitoring Based on Polarization Controlled Stimulated Brillouin Scattering

Pascual Sevillano, Jesús M. Subías, Asier Villafranca, and Javier Pelayo

***Abstract*— In this letter, we present a new all-optical method for the measurement of the wavelength-resolved state-of-polarization vector across the bandwidth of multiple in-service channels. Taking advantage of the narrow spectral selectivity of stimulated Brillouin scattering and its dependence with the relative polarization alignment between the pump and the stimulus, polarization selective spectral measurements are performed on the signal under test. Obtaining the spectra for three pairs of orthogonal polarization states of the pump, the three Stokes parameters are retrieved for each spectral component. Differential group delay is then calculated from the spectral evolution of the polarization state.**

***Index Terms*— Nonlinear optical devices, Stokes parameters, optical fiber polarization, optical communication equipment, optical fiber communication.**

I. Introduction

THE deployment of 100G channels over existing DWDM infrastructure is requiring a massive requalification of existing fibers due to the higher sensitivity to polarization mode dispersion (PMD) [1]. Performing these measurements without interrupting the service is essential for telecom operators, thus limiting the use traditional PMD measurement hardware and methods. State-of-the-art monitoring techniques for PMD in non-coherent conventional modulation schemes can be divided in post-filtering RF analysis [2], eye pattern analysis [3] and State of Polarization (SOP) evolution monitoring [4]. The latter is the only one that can be performed in the optical domain without the need for demodulation, and is based on the identification of the polarization plane with the highest delay between orthogonal polarizations for a given signal under test (SUT), measuring the differential group delay (DGD) from the interferometer-like effect of this delay over the spectrum. However, all published methods based on resolved polarization analysis of the signal spectrum require either previous alignment of the system or manipulation of the signal polarization state [5]–[7], thus limiting the measurement to individual channels.

Manuscript received April 29, 2013; revised June 7, 2013 and June 19, 2013; accepted June 20, 2013. Date of publication July 4, 2013; date of current version July 29, 2013. This work was supported in part by the Spanish MICINN under Project TEC2010-17869 and in part by the Spanish MINETUR under Project TSI-020100-2011-423.

P. Sevillano, J. M. Subías, and J. Pelayo are with the Photonic Technologies Group, Instituto de Investigación en Ingeniería de Aragón, University of Zaragoza, Zaragoza 50018, Spain (e-mail: psevi@unizar.es; jesus.subias@unizar.es; pelayo@unizar.es).

A. Villafranca is with the Aragon Photonics Labs S.L.U., Zaragoza 50009, Spain (e-mail: a.villafranca@aragonphotonics.com).

Digital Object Identifier 10.1109/LPT.2013.2271509

In this letter, we propose a method for live monitoring of the DGD values for any given number of channels simultaneously and without the need of system or signal alignment, thus enabling a much faster measurement of a full DWDM system. Thanks to the speed of the measurement, this method could also be applied to monitor instantaneous DGD.

For this purpose, we rely on the use of Stimulated Brillouin Scattering (SBS) high spectral and polarization selectivity to obtain high-resolution polarization selective spectra of the SUT for 6 different polarizations of the pump. From these spectra, we obtain the three Stokes parameters of the whole signal along its bandwidth and thus calculate the wavelength-resolved SOP. From the evolution of the in-band SOP, we can easily extract DGD and thus PMD for each channel individually and simultaneously without prior knowledge of the modulation format or fast electronics detection. Determination of spectral evolution of PMD vector along a channel spectrum allows accurate all-order PMD measurement.

II. Theoretical Background

Stimulated Brillouin Scattering is known to couple two counter-propagating waves, SUT and pump, through an acoustic wave due to an electrostriction effect. This phenomenon has been previously used as a high-gain swept-tunable optical amplifier for spectrometry thanks to its narrow width (∼10Mhz) and large dynamic range [8]. The polarization dependence of the Brillouin gain arises from the absence of the phenomenon when the pump and signal under test (SUT) fields are orthogonal. When the scattering takes place in a spool of fiber, both fields experience the same evolution of their SOP along the fiber with respect to their original states. This yields to a differential gain of the filter which depends on the relative polarization of pump and SUT that is given by:

$$\gamma_b = \frac{\gamma_0}{2}\left(1 + \left\langle \hat{s}_p \cdot \hat{s}_{SUT} \right\rangle_L\right). \tag{1}$$

Where the two vectors stand for the Stokes space representation of the SOP for the pump and the SUT. The length-averaged dot product of both vectors along the fiber has been proved to vary from minus one third, when they are orthogonal in one end, to one third, when they are parallel [9]. So the SBS can be treated as a polarization selective element that presents two different gains for the states parallel and perpendicular to the pump when it is injected in the spool of fiber $[\hat{s}_p(z = L), \hat{s}_p^{\perp}(Z = L)]$. This behavior has been recently studied and proposed as a high-rejection bandpass gain filter [10]. These different gain values for the two orthogonal

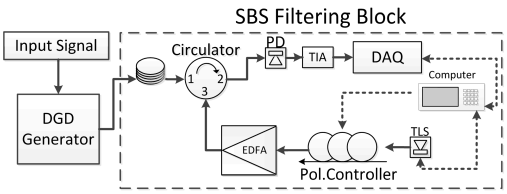

Fig. 1. Schematic of the necessary set-up for the retrieving of the frequency resolved state of polarization divided in three blocks.

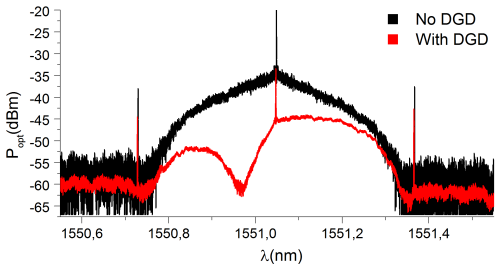

Fig. 2. Measured single-polarization spectra for a 40 G OOK-NRZ SUT with no DGD (black) and 8.55 ps DGD (red).

polarization states yields to a different final output value of the amplified spectral component when it exits the fiber depending on its income polarization. For high enough power of the pump this gain difference can be considered as an effective rejection ratio between these orthogonal states that depends on the range of powers, reaching values above 30dB polarization selective gain between orthogonal states [9]. Thanks to this polarization sensitivity, six high resolution spectra can be obtained, which correspond to the projection of the SUT to three pairs of orthogonal states of the pump matching the three axes of the Stokes space. The ratios between corresponding spectra return the evolution of the Stokes parameters with wavelength.

III. Experimental Setup

The pump for SBS is generated by an external-cavity TLS that emits linearly polarized light and is continuously swept over the wavelength region of interest (see Fig. 1). The pump polarization is controlled with a piezoelectric polarization state generator, capable of generating the six polarization states required for a full Stokes vector characterization (0, 45, 90 and -45 degrees of linear polarization (LP), right-hand circular (RHC) and left-hand circular (LHC) polarization) with a switching time lower than 1ms, which allows seamless switching of states. Pump power is controlled by an EDFA working in constant power mode. An optical circulator is used to inject the pump into the fiber spool and retrieve the backscattered light produced by SBS, detected by the Photodetector (PD) and acquired by a data acquisition card (DAQ) right after the Transimpedance Amplifier (TIA). The SUT is injected directly on the opposite termination of the fiber spool. DGD of the SUT is induced by a passive PMD generator. Specific parameters of fiber length and pump power, to reproduce the Brillouin spectrum analysis technique, can be found in previous work [8].

As the TLS is swept along the spectral region of the SUT for six SOP generated with the polarization controller, the high-resolution optical spectra of the SUT are revealed and the Stokes parameters calculated.

IV. Results and Discussion

The measured power spectra for a 0 deg LP pump is shown in fig. 2 for an OOK-NRZ 40-GHz signal modulated with a pseudo-random bit sequence of $2^{31}-1$ bit pattern length both with and without PMD. The spectrum of the PMD-free SUT corresponds to what has been widely reported for this kind of PRBS modulation, i.e. a sinc shape with the carrier and clock-frequency components. On the other hand in the spectrum where DGD has been induced on the SUT, the spectrum exhibits distortion in the shape of the spectrum with one prominent minimum value in its spectral width. Note that due to its narrowness, noise levels registered in the power spectra would be 30dB lower than grating-based spectrum analyzers.

This spectral shape is the consequence of the evolution of the SOP through the spectral components of the signal produced by DGD. Due to the sensitivity of the SBS effect to the polarization state, the amplification of each spectral component depends on its relative polarization to the pump TLS; yielding to a minimun for those componets with a relative orthogonal polarization state and a maximun for those parallel. Then, it can be easily deduced that this shape is the product of the sinc function, corresponding to the case without PMD, with the periodic variation of the polarization due to the PMD induced in the generator. Now by switching the polarization state of the pump to its perpendicular state (90 deg LP), the complementary spectrum is obtained, and then the maximum points turn to be minimum and likewise for the prior minimum, hence the combination of both recovers the original shape of the sinc function for the non-distorted signal.

Using a complete controller, the polarization state of the pump TLS can be rotated to the other four principal polarization states. Thus by rotating the pump to $+45$ LP and then to -45 LP, the normalized ratio of these two spectra corresponds then to the second Stokes parameter resolved spectrally. Finally, by setting the pump to LHC and RHC the third Stokes parameter can be retrieved [11]. In the fig. 3, the three Stokes parameters for the signal are depicted across the signal bandwidth, together with the Ponicaré sphere representation of the spectrally-resolved SOP.

These parameters determine completely the evolution of the polarization vector in the Stokes space. Unlike the measurement methods using one single axis, this analysis provides information of the full SOP evolution, allowing higher-order PMD effects to be easily observed. To obtain effective DGD values, the trajectory of the SOP in the sphere is integrated. Power spectra for the six states are optimally performed sweeping the pump TLS frequency at the speed of 10nm/s and the rotation between the states is performed while the data is processed. With these measurements the

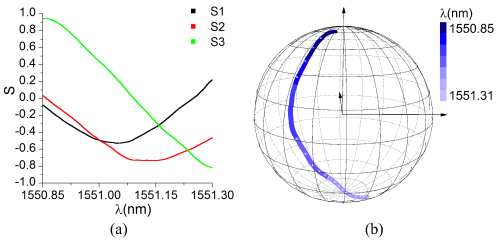

Fig. 3. (a) Recovered Stokes parameters resolved spectrally. (b) Representation of the SOP vector along the signal bandwidth in the Poincare sphere.

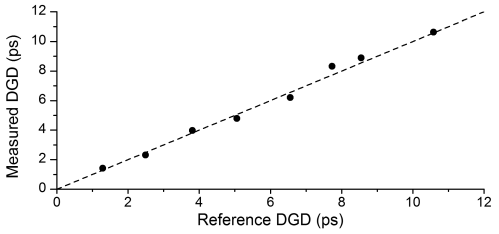

Fig. 4. Measured values of DGD for the different reference DGD values.

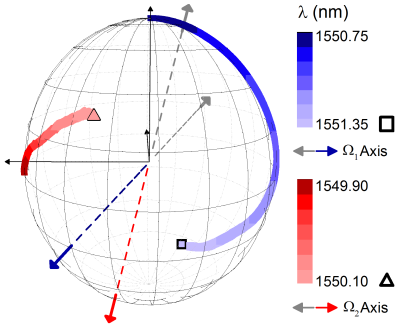

Fig. 5. Retrieved SOP resolved spectrally for both channels. Ω_1, Ω_2 represent the different DGD axis for both channels.

complete characterization of the signal polarization state can be resolved across its bandwidth, $[S1(\omega), S2(\omega), S3(\omega)]$, in times below 0.5 sec for a 100GHz span with an spectral resolution of 0.08pm. The measured values of the DGD for the different values set in the DGD generator are depicted in Fig. 4. Measurement range is limited by the accuracy in the acquisition of the power spectra, optimizing TLS sweep in this experiment the limit was set to 0.8ps.

One of the main advantages of the method is its capability to measure the DGD of several channels simultaneously without prior knowledge. In fig. 5 we can see the evolution of SOP of two NRZ-OOK signals at 40GHz and 10GHz modulation rates spaced by less than 50GHz. The two signals experience the same DGD but as the rates are different, the effects are much more evident for the high rate one. It is also calculated the axis of rotation for both signals. More realistic scenarios require statistical treatment of the measured DGD values in order to fully characterize PMD due to the random birefringence present in the deployed lines. It can be seen that with this high-resolution spectral polarimetry, high order PMD effects can be analyzed and monitored from the depicted arc and its axis, or their evolution.

V. Conclusion

We have presented a new method for the measurement of spectrally-resolved SOP of optical signals taking advantage of the spectral and polarization selectivity of SBS. This complete characterization allows live monitoring of polarization dispersion related impairment such as PMD, and gives a complete visualization of the polarization Stokes vector shift along the spectral components for multiple channels, without losing in-band resolution. Unlike state-of-the-art methods that require alignment for each channel, the proposed system can measure in-channel polarization drifts along the whole C+L band which yields to a full characterization of all-order PMD values for each channel without need of channel filtering, demultiplexing or alignment.

References

[1] E. Pincemin, *et al.*, "Challenges of 40/100 Gbps and higher-rate deployments over long-haul transport networks," *Opt. Fiber Technol.*, vol. 17, no. 5, pp. 335–362, Oct. 2011.

[2] T. Luo, C. Y. Yu, Z. Q. Pan, Y. Wang, Y. Arieli, and A. E. Willner, "Dispersive effects monitoring for RZ data by adding a frequency-shifted carrier along the orthogonal polarization state," *J. Lightw. Technol.*, vol. 23, no. 10, pp. 3295–3301, Oct. 2005.

[3] S. Lanne, W. Idler, J. P. Thiery, and J. P. Hamaide, "Fully automatic PMD compensation at 40 Gbit/s," *Electron. Lett.*, vol. 38, no. 1, pp. 40–41, Jan. 2002.

[4] F. Buchali, W. Baumert, H. Bülow, and J. Poirrier, "A 40 Gb/s eye monitor and its application to adaptive PMD compensation," in *Proc. OFC*, 2002, pp. 202–203.

[5] T. Xia, *et al.*, "Field trial of a novel non-intrusive method for in-service PMD measurements in fiber-optic networks," in *Proc. NFOEC*, Mar. 2012, pp. 1–3, paper NTu2E.5.

[6] I. Roudas, G. Piech, M. Mlejnek, Y. Mauro, D. Chowdhury, and M. Vasilyev, "Coherent frequency-selective polarimeter for polarization-mode dispersion monitoring," *J. Lightw. Technol.*, vol. 22, no. 4, pp. 953–967, Apr. 2004.

[7] L. Moller and L. Buhl, "Method for PMD vector monitoring in picosecond pulse transmission systems," *J. Lightw. Technol.*, vol. 19, no. 8, pp. 1125–1129, Aug. 2001.

[8] J. Domingo, J. Pelayo, F. Villuendas, C. Heras, and E. Pellejer, "Very high resolution optical spectrometry by stimulated Brillouin scattering," *IEEE Photon. Technol. Lett.*, vol. 17, no. 4, pp. 855–857, Apr. 2005.

[9] A. Zadok, E. Zilka, A. Eyal, L. Thevenaz, and M. Tur, "Vector analysis of stimulated Brillouin scattering amplification in standard single-mode fibers," *Opt. Express*, vol. 16, no. 26, pp. 21692–21707, Dec. 2008.

[10] A. Wise, M. Tur, and A. Zadok, "Sharp tunable optical filters based on the polarization attributes of stimulated Brillouin scattering," *Opt. Express*, vol. 19, no. 22, pp. 21945–21955, Oct. 2011.

[11] R. A. Chipman, "Polarimetry," in *Handbook of Optics*, vol. 2, 2nd ed., M. Bass, Ed. New York, NY, USA: McGraw-Hill, 1994, ch. 22, pp. 22.1–22.33.

Optics Communications 342 (2015) 144–151

Contents lists available at ScienceDirect

Optics Communications

journal homepage: www.elsevier.com/locate/optcom

OFDM subcarrier monitoring using high resolution optical spectrum analysis

Josep M. Fabrega [a,*], Pascual Sevillano [b], Michela Svaluto Moreolo [a], Asier Villafranca [c], F. Javier Vílchez [a], Jesús M. Subías [b]

[a] Centre Tecnologic de Telecomunicacions de Catalunya (CTTC), 08860, Castelldefels, Spain
[b] University of Zaragoza, 50018 Zaragoza, Spain
[c] Aragon Photonics Labs S.L., 50009 Zaragoza, Spain

ARTICLE INFO

Article history:
Received 23 September 2014
Received in revised form
18 December 2014
Accepted 22 December 2014
Available online 24 December 2014

Keywords:
Optical spectrum analysis
Optical performance monitoring
Fiber optic communications

ABSTRACT

In this paper, we demonstrate in-band OSNR monitoring of individual subcarriers in optical OFDM using a high-resolution optical spectrum analyzer. The relationships between OSNR, electrical SNR and BER at the receiver are experimentally analyzed and compared to theoretical results. A linear dependency in dB is found between electrical SNR and subcarrier OSNR for total OSNR values below 26 dB. Above this limit, the correlation degree decreases due to the electrical SNR degradation at the edge subcarriers. The BER analysis per subcarrier also shows a clear correlation with the proposed in-band optical measurements.

1. Introduction

Optical performance monitoring of signal quality is one of the key enablers of intelligent optical networks [1]. Precisely, transmission impairments monitoring is needed at the nodes of the network, where add/drop, routing and grooming functionalities are performed. Reconfigurable optical add-drop multiplexers and optical cross-connects are usually configured and managed by a control plane, which requires also in-band knowledge of the transmission impairments (e.g. noise, cross-talks, filtering effects, non-linearities, attenuation, dispersion, and component faults). The monitoring information is used by the control layer for configuring and optimizing optical paths, determining the causes of potential problems, setting up signal degradation alarms, preventing failures, and activating the corresponding resiliency mechanisms [2]. For example, the monitoring information can be disseminated by the control layer in order to compute spatial and spectral routes by means of impairment aware algorithms [3]. Then, a suitable network resources allocation and management can be performed. The optical signal to noise ratio (OSNR) is the most common parameter used to measure the degradation of signal quality, because it is transparent to bit rate and modulation format, and can be easily related to the bit error ratio (BER), which is the main performance indicator [1].

The advent of new and advanced optical modulation formats is attractive for improving the transmission performance; even they pose new challenges and/or opportunities from the optical performance monitoring point of view. Precisely, optical orthogonal frequency division multiplexing (O-OFDM) has gained attention in optical communications as it represents a promising candidate for high data rate optical systems and enables software-defined optical transmission [4]. In fact, this modulation format is able to provide high spectral efficiency, robustness to chromatic dispersion and scalability to higher bit rates. Furthermore, this multicarrier-modulation is suitable for future elastic and adaptive optical networks [4,5]. In these networks, the bandwidth and bit rate of the OFDM-based transponders can be configured by the control layer, varying the electronic digital signal processing (DSP) of the transponder and, thus, properly selecting the number of subcarriers and the modulation format.

Additionally to the robustness against transmission impairments, O-OFDM can provide electronic dispersion compensation. The overhead of information (e.g. pilot tones, training symbols, cyclic prefix), which must be allocated for correctly recovering the signal, allows monitoring system parameters for channel estimation and performance optimization [4,6]. However, this self-performance monitoring technique is performed in the electrical domain, requiring an optical receiver front-end. For an appropriate network management, a more simple and non-intrusive signal quality monitoring per subcarrier would be desirable at the nodes of the network. Thus, the control layer could dynamically

* Corresponding author.
E-mail address: jmfabrega@cttc.es (J.M. Fabrega).

http://dx.doi.org/10.1016/j.optcom.2014.12.062
0030-4018/

reconfigure the parameters of each O-OFDM transponder in order to overcome the signal degradation for specific subcarriers without the need for optical to electrical conversion. This can be achieved by balancing the modulation format per subcarrier and/or adding/suppressing subcarriers, when transmitting along a specific lightpath.

Among the DSP-based O-OFDM options, those based on intensity modulation and direct detection (IM/DD) constitute a cost-effective solution for the implementation of bit-rate and bandwidth variable transponders. So, these subsystems can be used in networks designed for more cost-sensitive market segments [7].

In this paper, subcarrier OSNR measurements for IM/DD O-OFDM systems are demonstrated using high-resolution optical spectrum analysis. We extend our previous work [8] by developing a method for relating the optical domain measurements with fundamental figures of merit for IM/DD O-OFDM, such as the electrical/digital signal to noise ratio (SNR) and the BER, each of them at a subcarrier level. This method is experimentally evaluated for an IM/DD O-OFDM system based on the Hartley transform, corroborating the above-mentioned relationships.

The remainder of the paper is organized as follows. Section 2 deals with the method for estimating the OSNR per subcarrier (SC-OSNR). Afterwards, in Section 3, an experimental setup is detailed. Next, Section 4 reports and discusses the results of the experiments. Finally, the main conclusions are drawn in Section 5.

2. OSNR estimation method

The impact of the optical noise on each O-OFDM subcarrier can be assessed by a simple optical spectrum analysis. This allows obtaining an OSNR measurement in the optical domain, at the subcarrier level. However, some processing of the acquired optical spectrum samples must be performed in order to properly relate these measurements with the signals recovered at the receiver, in the digital domain.

A typical IM/DD O-OFDM power spectrum is depicted in Fig. 1. Fig. 1(a) shows the baseband electrical spectrum, before upconversion and optical modulation. As can be seen, the multiple subcarriers are centered in the origin of the frequency axis (f=0).

The OFDM subcarriers are numbered for the sake of clarity. As the signal is real-valued, the subcarriers feature an Hermitian symmetry with respect to 0. Thus, according to the numbering in Fig. 1 (a), subcarrier 1 is the mirror-symmetric of subcarrier N, subcarrier 2 is the mirror-symmetric of subcarrier $N-1$, and so on.

For the case of real-valued fast Fourier transform (FFT), the symmetry of Fig. 1(a) is forced at the DSP of the transmitter [9]. There, only half of the subcarriers support data (e.g. 1 through $N/2$). The other half (e.g. $N/2+1$ through N) carry the complex-conjugate of this data.

Alternatively, when the fast Hartley transform (FHT) is used for OFDM modulation, the spectral symmetry is obtained with no additional processing [10]. In the following lines, we will go through some concepts of the FHT, in order to detail how digital data are finally mapped onto the electrical and optical spectra following the transmission scheme depicted in Fig. 2. At the transmitter DSP, input data are first parallelized and mapped onto a real constellation (e.g. binary phase shift keying – BPSK). Next, the training symbols (TS) are added and the transform is performed. It is worth noting that the FHT is a real transform with kernel [10]

$$\cos\left(\frac{2\pi kn}{N}\right)+\sin\left(\frac{2\pi kn}{N}\right), \tag{1}$$

N being the total number of subcarriers, n the number of samples, and k = 1, 2, 3, …, N the subcarrier number. An interesting property of the Hartley transform is that it is self-inverse [10] and, thus, the same implementation can be used at the transmitter and receiver signal processing.

After performing the transform, a cyclic prefix (CP) is added. Next, the resulting signal is serialized and upconverted to an intermediate frequency f_c. So, the upconverted OFDM signal after the digital to analog converter (DAC) can be described as

$$m(t) = V_{\mathrm{DAC}}\cos(2\pi f_c t)s(t), \tag{2}$$

where V_{DAC} corresponds to the voltage swing present at the output of the DAC and $s(t)$ is the OFDM signal itself

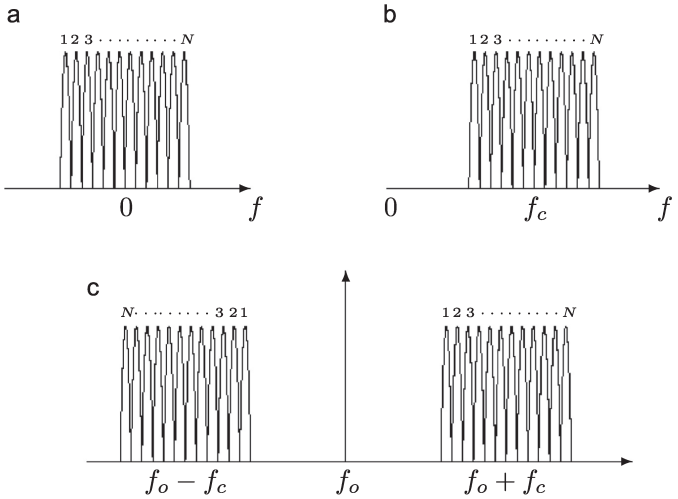

Fig. 1. Spectra of an IM/DD O-OFDM signal: baseband in the electrical domain (a), upconverted to f_c (b), and after modulation in the optical domain (c).

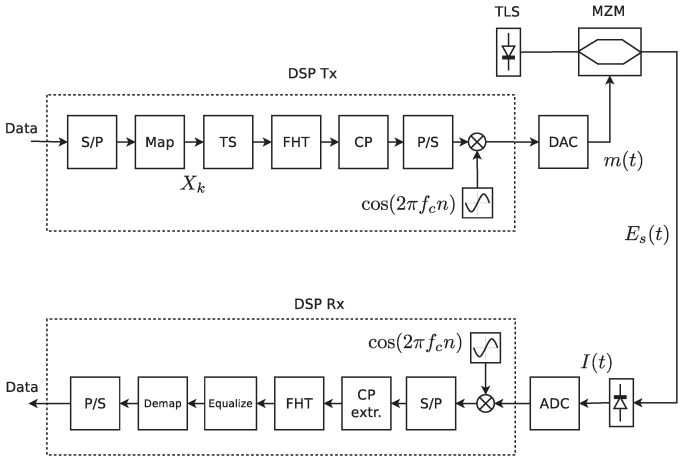

Fig. 2. Simplified transmission scheme.

$$s(t) = \frac{1}{\sqrt{N}} \sum_{k=1}^{N} X_k T_k(t), \tag{3}$$

with X_k indicating the data symbol carried by the k-th subcarrier, and $T_k(t)$ standing for the k-th coefficient of the FHT

$$T_k(t) = \cos(2\pi f_k t) + \sin(2\pi f_k t) \tag{4}$$

being $t = nT$ and f_k the k-th subcarrier frequency

$$f_k = \frac{k}{T} - \frac{N}{2T} \tag{5}$$

where T is the symbol period.

So, the optical field at the output of the Mach–Zehnder modulator can be expressed as

$$E_s(t) = \sqrt{P_s} \cos\left(\frac{\pi}{2V_\pi}(m(t) + V_b)\right) \exp(j2\pi f_o t), \tag{6}$$

where P_s is the optical power at the output of the modulator, V_b is the bias voltage, V_π is the switching voltage of the modulator, and f_o is the optical carrier frequency.

In case the bias point of the Mach–Zehnder modulator is set to $V_b = -V_\pi/2$ and assuming low voltage swing of $m(t)$, a pure intensity modulation is achieved and $|E_s(t)|^2$ can be approximated as

$$|E_s(t)|^2 \simeq \frac{P_s}{2} + \frac{P_s}{2}\frac{\pi}{V_\pi} m(t). \tag{7}$$

Fig. 1(c) shows the double sideband optical spectrum after optical modulation. As expected, the electrical spectrum is symmetrically repeated at both sides of the optical frequency f_o.

At the receiver, a standard photodiode with responsivity R is used, giving as output current

$$I(t) = R\frac{P_s}{2} + R\frac{P_s}{2}\frac{\pi}{V_\pi} m(t) + n(t), \tag{8}$$

$n(t)$ being a noise process, mainly contributed by optical noise.

After photodetection, the signal $I(t)$ is converted into the digital domain by an analog to digital converter (ADC). The resulting digital signal is processed in the DSP following the equivalent steps made in transmission, but in reverse order.

As expected, the digital OFDM signal is linearly mapped into the optical power, and can be recovered after photodetection with no distortion. Thus, if a direct spectrum analysis is made in the optical domain (prior to detection), the status of the OFDM signal carriers can be conveniently monitored.

The digitization, downconversion and FHT processing can be considered as a correlator bank plus sampling. Thus, after some algebra, the demodulated signal can be written as

$$Q_k = \frac{1}{T}\int_0^T \left[\frac{\pi R P_s V_{DAC}}{4V_\pi} s(t) + n(t)\right] T_k(t)\, dt = S_k + N_k; \tag{9}$$

S_k is the undistorted signal and N_k is the noise term. Similar to [11], S_k can be found as

$$S_k = \frac{1}{T}\int_0^T \frac{\pi R P_s V_{DAC}}{4V_\pi} s(t) T_k(t)\, dt = \frac{\pi R P_s V_{DAC}}{4V_\pi} X_k \tag{10}$$

and its power can be written as

$$P_X = \frac{\pi^2 R^2 P_s^2 V_{DAC}^2}{4V_\pi^2 N}. \tag{11}$$

Now, some assumptions on the noise should be considered. When the signal $E_s(t)$ is degraded by some optical noise (e.g. due to optical amplification), a certain SNR degradation is obtained after photodetection. According to the noise beating theory [12], the beating between signal and noise can be considered dominant for high OSNR, and it can be approximated as Gaussian noise. Thus, the power spectrum of $n(t)$ is approximately flat and with density

$$G_n(f) = \frac{2R^2 P_s^2}{\mathrm{SNR}_o B_o}, \tag{12}$$

where B_o is the optical reference bandwidth for measuring the OSNR, and $\mathrm{SNR}_o = P_s/P_{no}$ is the global optical OSNR, P_{no} being the power of optical noise within B_o.

According to (4) and (9), N_k can be expressed as two Fourier coefficients of $n(t)$ evaluated at $f = f_k/2$, whose variance is proportional to $G_n(f)$ evaluated at $f = f_k/2$ [11]. After making the necessary calculations, the variance of N_k can be expressed as

$$\sigma_N^2 = \frac{1}{4}\frac{1}{2T}\frac{2R^2 P_s^2}{\mathrm{SNR}_o B_o}. \tag{13}$$

The output of the k-th correlator is thus composed of a signal component S_k and an additive Gaussian noise component N_k,

leaving an SNR of

$$\mathrm{SNR}_e = \frac{P_x}{\sigma_N^2} = \frac{\pi^2 V_{\mathrm{DAC}}^2 B_o}{V_\pi^2 N B_e}\mathrm{SNR}_o, \tag{14}$$

$B_e = 1/T$ being the equivalent bandwidth occupied by each OFDM subcarrier.

So the probability of error can be found as that of BPSK modulated data with additive Gaussian noise [13]

$$P_e = \frac{1}{2}\,\mathrm{erfc}\sqrt{\frac{\mathrm{SNR}_e}{2}}. \tag{15}$$

Since a high resolution optical spectrum analysis is to be performed, an OSNR figure per subcarrier is defined. For convenience, this subcarrier OSNR (SC-OSNR) is defined as the quotient between the optical power measured per subcarrier P_{sc} and the power of the optical noise P_{no}. Using (2), (3), and (7), P_{sc} can be written as

$$P_{sc} = \frac{1}{2}\frac{\pi V_{\mathrm{DAC}}}{V_\pi\sqrt{N}}P_s, \tag{16}$$

consequently, the OSNR per subcarrier is

$$\mathrm{SNR}_{osc} = \frac{P_{sc}}{P_{no}} = \frac{\pi V_{\mathrm{DAC}}}{V_\pi\sqrt{N}}\mathrm{SNR}_o. \tag{17}$$

Thus, a linear relationship between SNR_{osc} and SNR_e can be found as

$$\frac{\mathrm{SNR}_{osc}}{\mathrm{SNR}_e} = \frac{1}{2}\frac{V_\pi\sqrt{N}}{\pi V_{\mathrm{DAC}}}\frac{B_e}{B_o}. \tag{18}$$

In other words, as SNR_e is proportional to the SNR_{osc}, one can estimate the performance of the OFDM modulation by a simple inspection of SNR_{osc}, and even extrapolate a limit for the symbol error probability.

Up to this point we have seen the relationship of the OFDM signal before and after optical modulation, and how the OSNR is related to the electrical SNR at the receiver side. However, an additional consideration should be made, when monitoring the proposed transmission system. According to Eq. (3), the Fourier transform of $s(t)$ is

$$M(f) = \frac{1}{\sqrt{N}}\sum_{k=1}^{N} F\{X_k\} * F\{T_k(t)\}, \tag{19}$$

where $*$ is the convolution operator and $F\{\cdot\}$ is the Fourier transform. The spectral behavior of the Hartley transform is related only to the term associated to the kernel

$$F\{T_k(t)\} = \frac{(1-j)\delta(f-f_k) + (1+j)\delta(f+f_k)}{2}. \tag{20}$$

Taken into account the Fourier transform of the kernel, each data symbol X_k is mapped onto two mirror symmetric subcarriers (f_k and $-f_k$). For example, X_1 contributes to subcarriers 1 and N of Fig. 1(a); X_2 contributes to subcarriers 2 and $N-2$ of the same figure; and so on. Additionally, when the whole signal is upconverted to an intermediate frequency f_c, as indicated by Fig. 1(b), the symmetry is with respect to f_c. Therefore, the FHT is an Hermitian linear operator, similar to the real-valued FFT.

In order to assess the impact of the optical signal degradation at a subcarrier level, the optical spectrum of Fig. 1(c) has to be mapped with the corresponding digital subcarriers, which are related to the electrical spectrum of Fig. 1(a) and (b). The procedure to employ is the following:

1. A SC-OSNR is measured in the spectral interval occupied by each subcarrier. In contrast with the total OSNR defined for 0.1 nm and accounting for an average performance of the whole system, this value allows specific characterization and performance degradation monitoring for each subcarrier.
2. The SC-OSNR contributions at the two sides of the optical carrier are averaged in order to take into account the symmetry due to the optical modulation. At this point, we obtain an SC-OSNR spectral distribution like Fig. 1(b) from Fig. 1(c).
3. In order to take into account the inherent Hermitian symmetry of the FHT (or a real-valued FFT), a further average of the SC-OSNR is performed between both sides of each OFDM band.

The resulting averaged SC-OSNR is a figure of merit which takes into account all the symmetries of the double sideband IM/DD spectra and, thus, can be directly related to the figures obtained in the digital domain, after OFDM demodulation. Additionally, this methodology can be easily adapted to other OFDM techniques. For example, when data is mapped into a complex-valued FFT combined with I/Q modulation and coherent detection, a more straightforward mapping between optical spectral components and data symbols is present, and step 3 can be avoided.

3. Experimental setup

In order to perform a first test of the OSNR monitoring at subcarrier level, the experimental setup described in Fig. 3 is used for a back-to-back configuration. It is conceived to characterize the correlation between the different levels of OSNR values in the

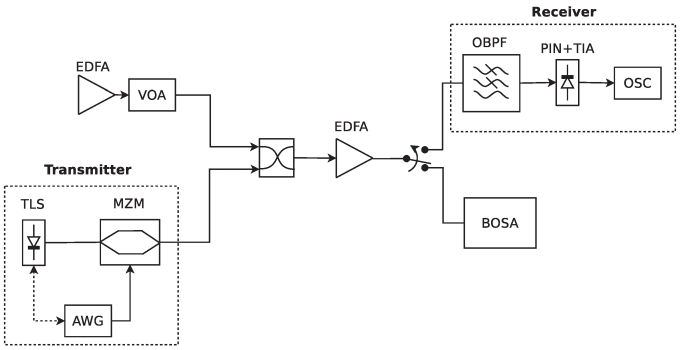

Fig. 3. Experimental setup.

optical domain and the performance analysis parameters in the electrical domain. The DSP and electrical up/down-conversion at the transmitter/receiver are performed off-line using Matlab, following the steps detailed in Fig. 2. At the transmitter, data are pseudo-randomly generated using the Mersenne-Twister generator [14]. Next, these data are mapped into the corresponding constellation (BPSK) and modulated by an FHT, with 64 subcarriers. The system is intended for occupying a 12.5 GHz channel, as it is the minimum slot width envisioned in an elastic and flexible networking environment [15]. Consequently, the total bandwidth of the generated optical spectrum is set to 11 GHz. A small guard band of 500 MHz around the optical carrier f_o = 193.865 THz (1550.92 nm) is set for avoiding undesired effects from the laser emission profile. Thus, the considered electrical bandwidth occupancy for the useful OFDM signal (51 subcarriers) is 5 GHz. The bit rate is 5 Gb/s, as a BPSK modulation format is used. The obtained real-valued OFDM symbols are then serialized. Every 2048 OFDM frames, 8 training symbols are inserted for synchronization and equalization. The digital OFDM signal is clipped and upconverted to an intermediate frequency (f_c = 3 GHz) by mixing it with a digital oscillator. The resulting signal is converted to the analog domain by an arbitrary waveform generator (AWG) running at 12 GSa/s. This analog signal is conditioned and injected to a Mach–Zehnder modulator (MZM) biased at the quadrature point and excited by a tunable laser source (TLS) operating at 1550.92 nm.

In order to experimentally analyze the optical noise performance, an additive white noise generated by an Erbium doped fiber amplifier (EDFA), followed by a variable optical attenuator (VOA), is introduced in the system by means of a 50:50 coupler. An additional EDFA is placed after the coupler for ensuring enough optical power for the spectral analysis and when employing the optical receiver. In order to relax the working conditions of this EDFA, an optical filter can be placed between the VOA and the 50:50 coupler.

The spectral analysis is performed with a high resolution optical spectrum analyzer (Aragon Photonics, BOSA 200). The equipment achieves 10 MHz resolution based on the use of stimulated Brillouin scattering (SBS) as an active optical filter [16]. Compared with other filtering techniques the main advantage of SBS is the high optical rejection ratio that it can achieve. Due to its non-linear nature, the device presents a -40 dB bandwidth of 60 MHz. The high rejection ratio of the system allows the measurement and characterization of spectrally close components. As it is an active filter, it also reaches a −70 dBm sensitivity with an 80 dB spurious free dynamic range. Other techniques capable to achieve similar characteristics could be also suitable, e.g. coherent spectrum analysis [17]. The high performance sought in the optical analysis is not arbitrary; it becomes necessary for the proper analysis of the different features present in these spectrally efficient modulation formats.

At the receiver, the incoming signal passes through an optical bandpass filter (OBPF) of 0.1 nm, for filtering out the optical noise of the concerning span. The reason to adopt this narrow optical filter is that it corresponds to the minimum spectral slot width envisioned in an elastic and flexible networking environment [15]. Next, the optical signal is detected by a module composed of a PIN diode and a transimpedance amplifier (PIN+TIA). The detected current is digitized by a real-time oscilloscope (OSC) running at 50 GSa/s. The OFDM baseband signal is then recovered after downconverting and low pass filtering in the digital domain. The recovered signal is off-line demodulated, equalized and demapped according to Fig. 2.

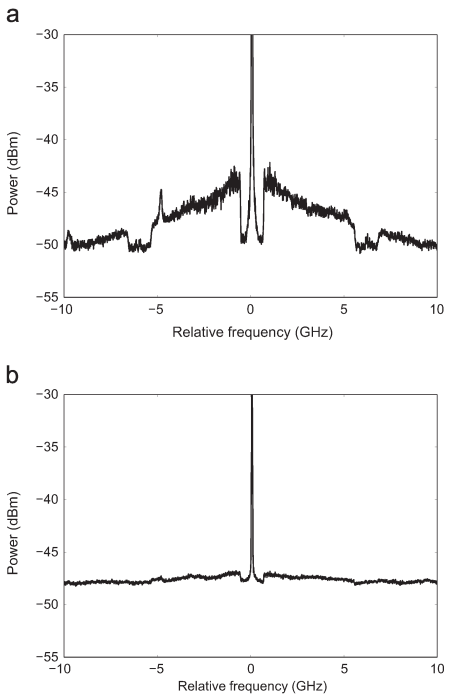

Fig. 4. Optical spectrum before the receiver with (a) 28 dB OSNR and (b) 18 dB OSNR.

4. Results and discussion

Several OSNR values are analyzed, ranging from 18 dB up to 32 dB, within a bandwidth of 0.1 nm. These values are further referred to as total OSNR, in order to distinguish them from SC-OSNR. Sample optical spectra are depicted in Fig. 4 using a resolution bandwidth of 10 MHz at −3 dB. Note that for the case of 28 dB all the useful signal within the OFDM bands is above the optical noise, as shown in Fig. 4(a). For the case of 18 dB OSNR, part of the OFDM bands is below the aforementioned noise level. This can be observed in Fig. 4(b).

As the resolution of the BOSA provides values of power in a 0.08 pm bandwidth, the optical signal level measurement can be performed for each frequency component corresponding to the OFDM subcarriers. For example, if the spectrum is sliced in frequency intervals equivalent to the occupancy of each subcarrier, individual performance monitoring of each subcarrier across the optical bandwidth is obtained without optical filtering. Fig. 5 shows a close-up view of one of the modulation sidebands. There, we can recognize the expected shape of the modulated subcarriers as shown in Fig. 1. Based on the recovered spectra we locate and extract the precise position of all the subcarriers, and measure their optical power. In the graph, we have marked the bandwidth of the different subcarriers by alternating white and gray colors. We obtain the total power of each subcarrier by integrating the power spectral density within their bandwidth. The noise is measured in the spectral regions where no subcarriers are present and then integrated according to the corresponding bandwidth of the subcarriers. For example, in a double sideband OFDM system, the noise level can be measured within the guardband around the

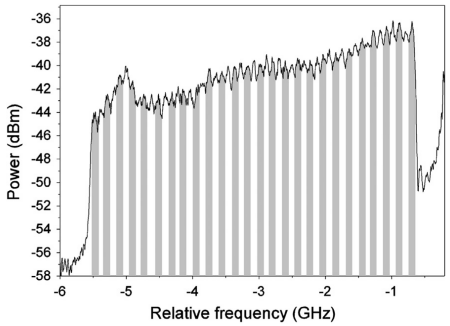

Fig. 5. Sample optical spectrum of one of the modulation sidebands. The bandwidth of the different subcarriers is evidenced alternating white and gray colors.

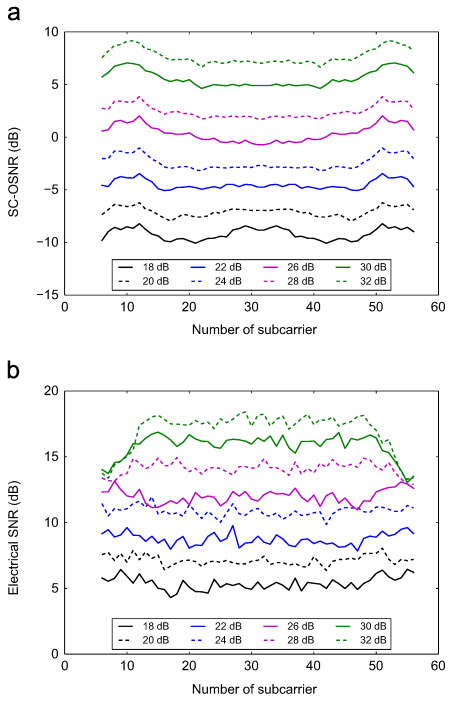

Fig. 6. (a) Distribution of the SC-OSNR from the measurement of the optical spectrum, per subcarrier. (b) Distribution of the electrical SNR measured before equalizing, per subcarrier.

optical carrier, as suggested in [8]. Polarization nulling techniques can also be applied to estimate the noise for each subcarrier. Then, the measured spectra are processed according to the method described in Section 2. The results obtained after this data processing are shown in Fig. 6(a), for the measured total OSNR values, showing the OSNR dependency over the FHT subcarriers. There it can be observed the OSNR dependency over the FHT subcarriers. Furthermore, the subcarriers that are more affected by the optical noise can be easily identified. For example, the first and last subsets of subcarriers (neighborhoods of the 10-th and 53-th subcarriers) have a value of OSNR greater than 3 dB compared to the

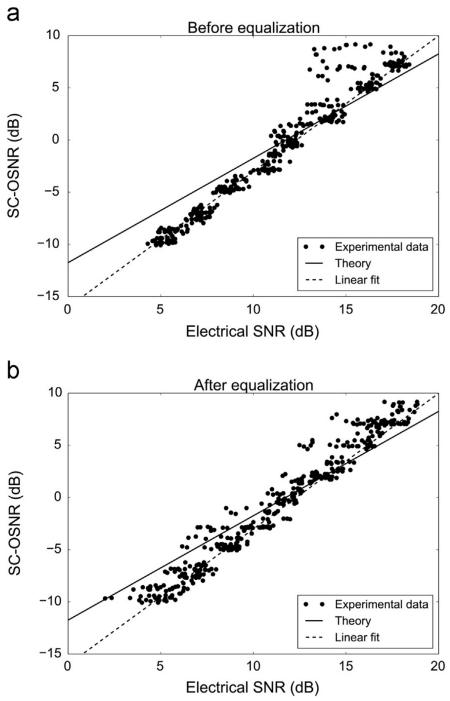

Fig. 7. SC-OSNR as a function of the electrical SNR taken (a) before equalization and (b) after equalization. Points are the values for different subcarriers and at different total OSNR values. Continuous line corresponds to theoretical model based on Eq. (18). Dashed line is the linear fit (in dB) of the points.

central subcarriers.

Similarly, the signal at the receiver is recovered just after the FHT block, where the electrical SNR is calculated as the quotient between the mean power and the variance per subcarrier, for the proposed range of total OSNR values. The distribution of this electrical SNR over the FHT subcarriers is depicted in Fig. 6(b). There it can be seen how the subcarriers are affected by the noise, after photodetection and DSP. For total OSNR values of 26 dB and below, the subcarriers in the neighborhood of 10-th and 53-rd subcarriers are less affected by the noise than the central ones (about 2 dB difference). Nevertheless, above 26 dB total OSNR, the central subcarriers outperform the ones at the edges. This is due to synchronization errors, mainly contributed by a small sampling frequency offset between transmitter and receiver, whose effects are only noticeable for high values of total OSNR. Note that the impact of the sampling frequency offset depends on the subcarrier number, degrading more the edges of the OFDM band than the central subcarriers [18].

A direct relationship is found between the SC-OSNR calculated from the high-resolution OSA spectrum and the electrical SNR calculated at the receiver. This is shown in Fig. 7, where the SC-OSNR is plotted as a function of the electrical SNR before equalization (a) and after equalization (b). As expected, the electrical SNR before equalization is highly correlated with the SC-OSNR. In fact, their dependency is almost linear in dB, meaning that increasing one dB of electrical SNR is directly translated to a 1 dB increase of SC-OSNR. Also, for electrical SNR in the neighborhood of 15 dB and higher, the theoretical model based on (18) is a lower

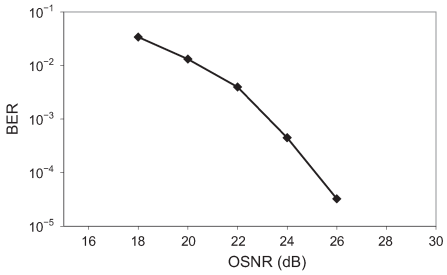

Fig. 8. Total BER as a function of the total OSNR.

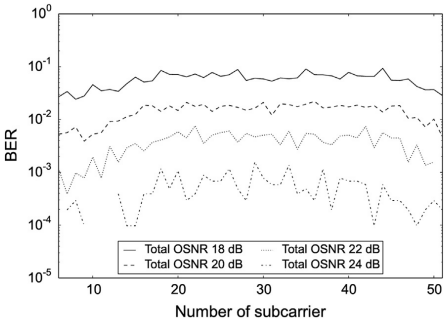

Fig. 9. Distribution of BER per OFDM subcarrier.

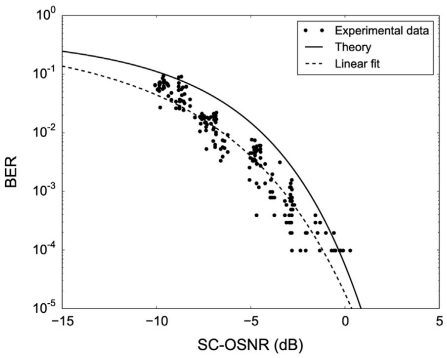

Fig. 10. BER as a function of the SC-OSNR. Points correspond to values for different subcarriers and at different total OSNR values.

limit, following the curve trend. For values of electrical SNR above 13 dB, there is a high dispersion of points, due to the fact observed in Fig. 6(b). For total OSNR values beyond 26 dB, the electrical SNR of the subcarriers at the edges is limited to ~13 dB. In order to overcome this effect, the electrical SNR is calculated after equalization, as shown in Fig. 7(b). For this case, the points corresponding to higher electrical SNR have lower dispersion. However, the other parts of the plot show less correlation between SC-OSNR and electrical SNR.

Finally, BER measurements are obtained by statistical bit error counting up to obtain 10^3 errors. Results are shown in Figs. 8–10. Fig. 8 shows the total BER as a function of the total OSNR. There it can be observed that 10^{-3} BER is attained at 23.7 dB of OSNR.

Fig. 9 shows the BER distribution over the active OFDM subcarriers at different values of total OSNR, for a single acquisition of 2^{15} bits. Comparing Fig. 6 with Fig. 9, a clear correlation between both can be seen, as expected. For example, in the neighborhood of the 10-th and 53-rd subcarriers, the BER is much lower than for the central ones (about one order of magnitude).

Also a direct relationship is found between SC-OSNR measured with BOSA and BER. This is shown in Fig. 10. As expected, the BER is correlated with the SC-OSNR, in a similar way to the total OSNR, see Fig. 6(a), decreasing one order of magnitude per 5 dB increase of SC-OSNR. Also, the BER calculated employing (18), represented with a continuous line, acts as an upper limit. This is because the theoretical model describes the limit performance, when SC-OSNR is above 15 dB and assuming a Gaussian distribution of the electrical noise, according to the discussion presented in Section 2.

5. Conclusion

In this work we have proposed a methodology to estimate the sub-carrier OSNR and we have demonstrated the direct correlation between the BER performance of individual sub-carriers and the measured sub-carrier OSNR. Live monitoring of these quality parameters can be performed at the nodes of the optical networks with no need for demodulating data. Thus, it becomes a key point towards better management of OFDM-based systems in future flexible and elastic optical networks. Additionally, the methodology developed can be easily adapted to be used when employing other OFDM techniques, as coherent optical OFDM.

Acknowledgments

This work was supported by EU/FP7 through project IDEALIST (G.A. 317999), MICYT through Project TSI-020100-2011-423 and by MINECO through Projects TEC2010-17869 and TEC2012-38119 (FARO).

References

[1] C.C.K. Chan, Optical Performance Monitoring Techniques, Elsevier, San Diego, CA, USA, 2010.
[2] R. Ramaswami, K. Sivarajan, G. Sasaki, Optical Networks: A Practical Perspective, Morgan Kaufmann, Burlington, MA, USA, 2009.
[3] R. Martínez, R. Casellas, R. Munoz, T. Tsuritani, Experimental translucent-oriented routing for dynamic lightpath provisioning in gmpls-enabled wavelength switched optical networks, J. Lightwave Technol. 28 (8) (2010) 1241–1255. http://dx.doi.org/10.1109/JLT.2010.2043335.
[4] W. Shieh, I. Djordjevic, Orthogonal Frequency Division Multiplexing for Optical Communications, Elsevier, San Diego, CA, USA, 2010.
[5] M. Jinno, H. Takara, B. Kozicki, Y. Tsukishima, Y. Sone, S. Matsuoka, Spectrum-efficient and scalable elastic optical path network: architecture, benefits, and enabling technologies, IEEE Commun. Mag. 47 (11) (2009) 66–73. http://dx.doi.org/10.1109/MCOM.2009.5307468.
[6] M. Svaluto Moreolo, J.M. Fabrega, L. Nadal, F. Vílchez, Software-defined optical ofdm transmission systems: enabling elasticity in the data plane, in: 14th International Conference on Transparent Optical Networks (ICTON), 2012, pp. 1–4. http://dx.doi.org/10.1109/ICTON.2012.6254504.
[7] M. Svaluto Moreolo, J.M. Fabrega, L. Nadal, F. Vílchez, V. Lopez, J. Fernandez-Palacios, Cost-effective data plane solutions based on OFDM technology for flexi-grid metro networks using sliceable bandwidth variable transponders, in: 2014 International Conference on Optical Network Design and Modeling, 2014, pp. 281–286.
[8] J.M. Fabrega, P. Sevillano, M. Svaluto Moreolo, J.J. Martinez, A. Villafranca, J. Subias, All-optical in-band OSNR measurement in intensity-modulated direct-detection optical OFDM systems, in: 15th International Conference on Transparent Optical Networks (ICTON), 2013, pp. 1–4. http://dx.doi.org/10.1109/ICTON.2013.6602731.
[9] B. Schmidt, A. Lowery, J. Armstrong, experimental demonstrations of electronic dispersion compensation for long-haul transmission using direct-detection optical OFDM, J. Lightwave Technol. 26 (1) (2008) 196–203. http://dx.doi.org/10.1109/JLT.2007.913017.

[10] R.N. Bracewell, The Fourier Transform and its Applications, McGraw-Hill, New York, 2000.
[11] J.M. Fabrega, M. Svaluto Moreolo, M. Chochol, G. Junyent, Impact of modulator driving on constant envelope optical OFDM based on Hartley transform, IEEE Photonics Technol. Lett. 25 (6) (2013) 598–601. http://dx.doi.org/10.1109/LPT.2013.2246785.
[12] G.P. Agrawal, Fiber-Optic Communication Systems, 3rd edition, John Wiley & Sons, Hoboken, NJ, USA, 2002.
[13] J.G. Proakis, Digital Communications, McGraw Hill, New York, NY, USA, 1989.
[14] M. Matsumoto, T. Nishimura, Mersenne twister: a 623-dimensionally equi-distributed uniform pseudo-random number generator, ACM Trans. Model. Comput. Simul. 8 (1) (1998) 3–30. http://dx.doi.org/10.1145/272991.272995.
[15] ITU-T Recommendation G.694.1: Spectral Grids for WDM Applications: DWDM Frequency Grid, Technical Report, International Telecommunication Union, February 2012.
[16] J.M. Subias, J. Pelayo, F. Villuendas, C. Heras, E. Pellejer, Very high resolution optical spectrometry by stimulated Brillouin scattering, IEEE Photonics Technol. Lett. 17 (4) (2005) 855–857. http://dx.doi.org/10.1109/LPT.2005.843946.
[17] D. Baney, B. Szafraniec, A. Motamedi, Coherent optical spectrum analyzer, IEEE Photonics Technol. Lett. 14 (3) (2002) 355–357. http://dx.doi.org/10.1109/68.986811.
[18] M. Sliskovic, Carrier and sampling frequency offset estimation and correction in multicarrier systems, in: Global Telecommunications Conference, 2001. GLOBECOM '01, vol. 1, IEEE, San Antonio, TX, USA, 2001, pp. 285–289, http://dx.doi.org/10.1109/GLOCOM.2001.965124.

ANNEX C

List of acronyms

APL	Aragon Photonics Lab
ASE	Amplifies Spontaneous Emission
AWG	Arbitrary Waveform Generator
BER	Bit Error Rate
BOSA	Brillouin Optical Spectrum Analyzer
BPSK	Binary Phase-Shift Keying
CD	Chromatic Dispersion
CSRZ	Carrier-Suppressed Return-to-Zero
DAQ	Data Acquisition Systems
DB	Duo Binary
DD	Direct Detection
DGD	Differential Group Delay
DOP	Degree of Polarization
DPSK	Differential Phase-shift keying
DQPSK	Differential Quadrature Phase Shift Keying
DSF	Dispersion Shifted Fiber
DSP	Digital Signal Processing
DWDM	Dense Wavelength Division Multiplexing
ECDL	External Cavity Diode Laser.

EDFA	Erbium Doped Amplifier
EPC	Electronic Polarization Controller
FFT	Fast Fourier Transform
FHT	Fast Hartley Transform
FTTH	Fiber to the Home
FWHM	Full Width at Half Maximum
FWM	Four Wave Mixing
GSa/s	GigaSamples per second
ICI	Intercarrier Interference
IDE	Integrated Development Enviroment
IEC	International Electrotechnical Commission
IFFT	Inverse Fast Fourier Transform
IM	Intensity Modulated
ITU	International Telecommunication Union
LP	Linearly Polarized
MCM	Multicarrier Modulation
Pol - MUX	Polarization Multiplexing
MZM	Mach-Zhender Modulator
NRZ	No Return to Zero
OBPF	Optical Bandpass Filter
OFDM	Orthogonal Frequency Division Multiplexing
O-OFDM	Optical Orthogonal Frequency Division Multiplexing
OOK	On-Off Keying
OPM	Optical Performance Monitoring / Optical Power Meter
OSA	Optical Spectrum Analyzer
OSC	Oscilloscope
OSNR	Optical Signal to Noise Ratio
OSNRSC	Sub-Carrier Optical Signal to Noise Ratio
PBC	Polarization Beam Coupler
PBS	Polarization Beam Splitter
PC	Polarization Controller
PDG	Polarization Dependent Gain
PDL	Polarization Dependent Loss
PMD	Polarization Mode Dispersion
PPG	Pulse Pattern Generator
PRBS	Pseudo Random Bit Sequence
PSD	Power Spectral Density
PSP	Principal States of Polarization
QAM	Quadrature Amplitude Modulation
RF	Radio Frequency
ROADM	Reconfigurable Optical Add-Drop Multiplexer
RSS	Residual Sum of Squares

RZ	Return to Zero
SBS	Stimulated Brillouin Scattering
SC	Sub Carrier
SDH	Synchronous Digital Hierarchy
SG-DBR	Sampled Grating Distributed Bragg Reflector
SMF	Single Mode Fiber
SNR	Signal to Noise Ratio
SONET	Synchronous Optical Networking
SOP	State of Polarization
STM	Synchronous Transport Module
SUT	Singal Under Test
TIA	Transimpedance Amplifier
TLS	Tunable Laser Source
TTL	Transistor–transistor logic
U-DWDM	Ultra Dense Wavelength Division Multiplexing
VDL	Variable Delay Line
VOA	Variable Optical Attenuator
WDM	Wavelenght Division Multiplexing
XPM	Cross-Phase Modulation